SURFACE WAVE DISPERSION ABOUT THE NEW MADRID REGION

Flor de Lis Mancilla Pérez, B.E.

**A Digest Submitted to the Faculty of the Graduate School
of Saint Louis University in Partial Fulfillment of
the Requirements for the Degree of
Master of Science (Research)**

2001

Digest

The dispersion properties of surface waves encode information about the structure of the Earth. In this thesis I obtain group velocity dispersion curves and local phase velocity dispersion curves for a set of earthquakes and explosions. Specifically, the data set consists of 50 events recorded in the Cooperative New Madrid Seismic Network (CNMSN), run by Saint Louis University, and the Alabama earthquake (October 24, 1997) recorded by 48 stations spread over North America.

In obtaining the group velocity curves I use the Multiple Filter and the Phase Matched Filter techniques. The combination of these two techniques permits isolation of the fundamental mode to obtain cleaner group velocity dispersion curves. The group velocity dispersion curves are used to test the viability of the Stevens' model, a global model developed under the Comprehensive Nuclear-Test-Ban Treaty (CTBT) monitoring. The results of the test show that the Stevens' model works well in the range of periods between 10 and 160 seconds (with differences between observations and prediction within $\pm 3.3\%$ at 20 seconds). For periods larger than 160 seconds the model overestimates the values of the group velocities dispersion curve (at 260 seconds the overestimations are around $12.5 \pm 2.5\%$).

Once the fundamental mode is isolated the local phase velocity dispersion curves are calculated with the $p - \omega$ technique. I have checked the performance of this technique, developed for linear arrays in reflection and refraction experiments, in the non-linear CNMSN array. For some particular earthquakes, those with the best station coverage and the clearest disper-

1

sion curves for a wide period range, the technique works surprisely well (the differences between observations and predictions are within 5%). For these events the local phase velocity dispersion curves fit the predictions of the HAMBURG model for central U.S. (Herrmann and Ammon, 1997). For the other earthquakes, the $p - \omega$ technique has not been successful. Further studies are needed to better improve this technique.

SURFACE WAVE DISPERSION ABOUT THE

NEW MADRID REGION

Flor de Lis Mancilla Pérez, B.E.

**A Thesis Submitted to the Faculty of the Graduate School
of Saint Louis University in Partial Fulfillment of
the Requirements for the Degree of
Master of Science (Research)**

2001

COMMITTEE IN CHARGE OF CANDIDACY:

Professor Robert B. Herrmann,
     Chairperson and Advisor

Associate Professor Charles J. Ammon

Associate Professor John Encarnación

Acknowledgments

I express my thanks

To Carlos because without his help I would have never finished this thesis. Thanks for being my special friend and colleage. To learn about physics and life with you has been a pleasure. Thanks for sharing with me these two years. Te quiero.

To my advisor Bob Herrmann for giving me the opportunity to spend these two years here and for his contributions to this thesis.

To Chuck Ammon for giving me the opportunity to work with him, opening the door to real research.

To John Encarnación for reading my thesis and for being the joy of the department.

To David Kirschner for being more than a teacher and for the field trips, the next in Hawaii!.

To Jordi, for those afternoons sitting around a coffee cup, planning future projects and discussing seismology. Gracias amigo.

To Jorge for being my "Compa" and my friend. Thanks for encouraging me.

To the rest of students: Minoo, Hong-yi, Fabrizio, Dan, Winchell, David Young-Soo, and Alemayehu.

To all the staff: Melanie, Bob, Eric, Jeanne, and Christine for helping me always when I needed.

To Matt and Elena for being my friends and making my life better.

Finally, to my family, for giving me their love and support from home.

Table of Contents

List of Tables

List of Figures

1. INTRODUCTION

Knowledge of the Earth's structure with depth is a very challenging problem. The almost unique source of information for structures located "at intermediate and deep depths" comes from the record of seismic signals. Among these, the surface waves play a principal role. As its name states, surface waves are signals associated with the presence of a free surface (or, more generally, a discontinuity surface). Their amplitudes decrease inversely with the distance from the source, in contrast to the quadratic decrease of P- and S-wave amplitudes. For this reason, the surface waves form the longest and the strongest portion of the seismic records excited by explosions and shallow earthquakes. Within the surface waves, information about the Earth's structure is encoded in the form of their dispersion curves. The longer the wave length of a surface wave the deeper it samples the Earth's structure, and the faster is its propagation velocity. Thus, to analyze how the velocity of propagation of a surface wave depends on its wavelength (dispersion) amounts to probing Earth's structure.

The appearance of a seismic record depends on the signal source and the propagation properties of the path between source and receptor. For the Rayleigh surface waves part of the seismic record, Stevens and Adams (1999) have developed a global model, here after referred to as the Stevens' model, that provides the group velocity dispersion curves from any source point to any receiver point. Their main aim was to have a reliable means of identifying the 20 s Rayleigh wave to automatically determine Ms of an earthquake or an explosion for the Comprehensive Nuclear-Test-Ban

Treaty (CTBT) monitoring. In fact, a good determination of $M_s : m_b$, that is, the relation of the magnitude of a source associated with surface waves versus to that associated with body waves, and its regional variants, is among the most reliable discriminants.

In 1990, Saint Louis University upgraded a preexisting seismic network to form the present Cooperative New Madrid Seismic Network (CNMSN) consisting of broadband sensors. This increases the quality of data supporting new types of research. This region is important because it is one of the most seismically active intraplate regions of the world. This study is a first step towards an improved determination of the shear-velocity structure of the crust and uppermost mantle in the region.

In the present work I obtain group and local phase velocity dispersion curves for 50 events recorded in this network (CNMSN) and for the Alabama earthquake (October 24, 1997) that was recorded in 48 stations spread over North America. The group velocity dispersion curves so obtained permit testing the performance of the Stevens' model (Stevens and Adams, 2000) comparing the observation with its predictions. One aspect in which I am particularly interested is the adequacy of the model for paths to the New Madrid region depending on the frequency range. Having a confident global model in an as-wide-as-possible frequency range will provide an outstanding tool for different kinds of analysis such as the study of seismic sources or receiver functions.

I start this thesis with an overview on surface waves and their dispersion properties in Chapter 2. In Chapter 3, the theoretical bases for the group velocity measurements (multiple filter technique and phase matched filter) are introduced. Then, Chapter 4 is concerned with the actual group

velocity observations and its comparison with the Stevens-Adams model. In Chapters 5 and 6, I present the theoretical ideas behind the measurement of the phase velocity (p-ω stacking), and the actual phase velocity observations, respectively. In all this work it is assume that the effects on the measurement of *i)* the deviation of ray paths from the great-circle linking the source to the receivers, *ii)* azimuthal anisotropy and, *iii)* mislocations of earthquake epicenters are negligible. Finally, in Chapter 7 I discuss the results.

2. SURFACE WAVES

2.1 INTRODUCTION

The sudden redistribution of stresses in the earth as a result of an earthquake (or other sources like the explosion of a nuclear weapon) produces a release of energy in the form of elastic waves. The series of movements registered by a seismic detector in some other point of the earth's surface depends on the characteristics of the source and on the specific earth structures crossed by the waves on their way towards the detector.

In this work I am interested in the characterization of the structure of the earth in term of its elastic properties. First, we will review how each region of the earth can be characterized the parameters: bulk and the shear moduli, or alternatively the longitudinal and the transverse wave velocities. I will introduce the concept of surface waves by considering the earth as a layered half-space. We will see how to extract information about the earth structure taking into account the part of the seismograms associated with these surface waves.

2.2 EARTH STRUCTURE AND BODY WAVES

Imagine that one analyzes the interior of a region of the earth with a resolution such that it appears homogeneous isotropic and very large. In the small-strains small-displacements approximation we will have a linear relation

$$\tau_{ij} = C_{ijkl}\epsilon_{kl}, \quad C_{ijkl} = \lambda\delta_{ij}\delta_{lk} + \mu(\delta_{ik}\delta_{jl} + \delta_{il}\delta_{jk}) \tag{2.1}$$

between the stress tensor τ_{ij} and the strain tensor ϵ_{ij} that depends on the two Lamé parameters λ (associated with the bulk modulus) and μ (shear modulus). Remembering the relation between the stress tensor and the displacement vector field u_i

$$\epsilon_{ij} = \frac{1}{2} \left(\partial_i u_j + \partial_i u_j \right),\tag{2.2}$$

we can arrive at the following equation of motion for the displacement field (Ben-Menahem and Singh, 1981, p. 20; Aki and Richards, 1980, p. 64)

$$(\lambda + 2\mu)\vec{\nabla}(\vec{\nabla} \cdot \vec{u}) - \mu\vec{\nabla} \times (\vec{\nabla} \times \vec{u}) + \rho\vec{F} = \rho\frac{\partial^2 \vec{u}}{\partial t^2}.\tag{2.3}$$

Here $\vec{F}$ denotes any external force per unit volume and ρ is density of the earth in the particular region being analyzed. Now, if we separate the displacement vector into two components

$$\vec{u} = \vec{u}_\alpha + \vec{u}_\beta, \quad \vec{\nabla} \times \vec{u}_\alpha = 0, \quad \vec{\nabla} \cdot \vec{u}_\beta = 0,\tag{2.4}$$

we can rewrite the equation of motion in absence of external forces as

$$\alpha^2 \left(\nabla^2 - \frac{1}{\alpha^2}\frac{\partial^2}{\partial t^2} \right) \vec{u}_\alpha + \beta^2 \left(\nabla^2 - \frac{1}{\beta^2}\frac{\partial^2}{\partial t^2} \right) \vec{u}_\beta = 0,\tag{2.5}$$

$$\alpha = \left(\frac{\lambda + 2\mu}{\rho} \right)^{1/2}, \quad \beta = \left(\frac{\mu}{\rho} \right)^{1/2}.\tag{2.6}$$

By looking at the form of this equation and the definitions of u_α, u_β we can deduce that a general displacement field configuration can be expressed as a superposition of plane waves of two types:

- Longitudinal waves (or P waves)

$$\vec{u}_P = A_P \hat{k} \exp\left[ik(\alpha t - \hat{k} \cdot \vec{x}) \right].\tag{2.7}$$

- Transverse waves (or S waves)

$$\vec{u}_{S\eta} = A_{S\eta}\hat{a}_\eta \exp\left[ik(\beta t - \hat{k}\cdot\vec{x})\right]. \tag{2.8}$$

Here the index η can take two values where the unit vectors $\hat{a}_\eta = \{\hat{a}_1, \hat{a}_2\}$ are orthogonal to the direction of propagation of the wave, e.g., $\hat{a}_\eta \cdot \hat{k} = 0$.

Of course, a plane wave solution is an abstract idealization as a physical region is neither infinite nor eternal. A finite piece of a plane wave in space and time can be a very good approximation to the configuration of the field in many interesting situations.

The characteristics of a particular earth region can be encoded in the values of the velocity of propagation of longitudinal and transverse plane waves, respectively α and β together with the density, ρ.

2.3 LAYERED HALF-SPACE EARTH MODEL

A first approximation to the description of the earth is that it consists of several layers in depth with different properties (different values of α, β, and ρ). To understand the propagation of waves for this model, one way to proceed is to look again at the decomposition of a generic solution into simple traveling wave configurations. (These traveling waves now are not going to be plane waves, although some of them could be seen as pieces of plane waves pasted along the surfaces discontinuities.)

In this thesis, we will concentrate on the specific configurations related with the existence of the free surface of the earth. For this reason let us consider first a half-space as a model for the earth.

The surface of the earth is free. This implies that the components of the stress tensor in the vertical direction, z, must be zero: $\tau_{ij}\hat{a}_z^j = 0$. (We will define the free surface as the $z = 0$ plane and assume that the medium occupies the region $z > 0$). Let's separate the transverse body waves into horizontal (or SH waves), if the particle motion is parallel to the surface, and vertical (or SV waves), if it is not parallel to the surface. The different traveling wave configurations proper of this model are:

- SH wave incident at the surface:

$$\vec{u} = \vec{u}_{SH}^I + \vec{u}_{SH}^R = A_{SH}^I \hat{a}_y \exp\left[i\omega t - i(\omega/\beta)(\sin\theta\ x - \cos\theta\ z)\right]$$

$$+ A_{SH}^I \hat{a}_y \exp\left[i\omega t - i(\omega/\beta)(\sin\theta\ x + \cos\theta\ z)\right]. (2.9)$$

Here θ denote the incidence angle. As a limiting case there is the possibility of a half plane SH wave traveling along the x direction.

- SV wave incident at the surface. In this configuration there are a reflected SV and a reflected P wave:

$$\vec{u} = \vec{u}_{SV}^I + \vec{u}_{SV}^R + \vec{u}_P^R$$

$$= A_{SV}^I (\cos\theta\hat{a}_x + \sin\theta\hat{a}_z) \exp\left[i\omega t - i(\omega/\beta)(\sin\theta\ x - \cos\theta\ z)\right]$$

$$+ A_{SV}^R \frac{\sin 2\varphi \sin 2\theta - (\alpha/\beta)^2 \cos^2 2\theta}{\sin 2\varphi \sin 2\theta + (\alpha/\beta)^2 \cos^2 2\theta}$$

$$\times (-\cos\theta\hat{a}_x + \sin\theta\hat{a}_z) \exp\left[i\omega t - i(\omega/\beta)(\sin\theta\ x + \cos\theta\ z)\right]$$

$$+A_P^R \frac{(\alpha/\beta)\sin 4\theta}{\sin 2\varphi \sin 2\theta + (\alpha/\beta)^2 \cos^2 2\theta}$$

$$\times (\sin\varphi\hat{a}_x + \cos\varphi\hat{a}_z)\exp\left[i\omega t - i(\omega/\alpha)(\sin\varphi\ x + \cos\varphi\ z)\right]. \quad (2.10)$$

In this expression the angle φ is related to θ by Snell's law: $\frac{\sin\theta}{\beta} = \frac{\sin\varphi}{\alpha}$. When $\sin\theta > (\beta/\alpha)$, $\sin\varphi$ becomes greater than 1 (φ become complex), and therefore $\cos\varphi$ becomes pure imaginary. By looking at the previous expression one can see that an imaginary $\cos\varphi$ amounts to a evanescent inhomogeneous P wave traveling in the x direction. It is also worth mentioning that it is not possible to have a "half-plane SV" wave traveling in the x direction without the P-wave disturbance.

- P wave incident at the surface. The configuration consists of a reflected SV and a reflected P wave:

$$\vec{u} = \vec{u}_P^I + \vec{u}_P^R + \vec{u}_{SV}^R$$

$$= A_P^I(\sin\varphi\hat{a}_x - \cos\varphi\hat{a}_z)\exp\left[i\omega t - i(\omega/\alpha)(\sin\varphi\ x - \cos\varphi\ z)\right]$$

$$+A_P^R \frac{\sin 2\varphi \sin 2\theta - (\alpha/\beta)^2 \cos^2 2\theta}{\sin 2\varphi \sin 2\theta + (\alpha/\beta)^2 \cos^2 2\theta}$$

$$\times (\sin\varphi\hat{a}_x + \cos\varphi\hat{a}_z)\exp\left[i\omega t - i(\omega/\alpha)(\sin\varphi\ x + \cos\varphi\ z)\right]$$

$$+A_{SV}^R \frac{-2(\alpha/\beta)^2 \sin 2\varphi \cos 2\theta}{\sin 2\varphi \sin 2\theta + (\alpha/\beta)^2 \cos^2 2\theta}$$

$$\times \left(- \cos\theta \widehat{a}_x + \sin\theta \widehat{a}_z \right) \exp\left[i\omega t - i(\omega/\beta)(\sin\theta\ x + \cos\theta\ z) \right]. \quad (2.11)$$

In this case φ is the angle of incidence of the P wave. Again Snell's law provides the relation between φ and θ. Notice that in these solutions there are no evanescent parts. We see that it is not possible to have a "half-plane P" wave moving in along the x direction without SV

- In a half space earth model there is only one other additional type of configuration: the Rayleigh wave. These are evanescent inhomogeneous plane waves with P and SV components. We will deal with them more extensively in the next section.

2.4   RAYLEIGH WAVES

Extrapolating the form of a plane wave to the case in which some of the direction cosines $\widehat{k}_x$, $\widehat{k}_y$ $\widehat{k}_z$ are greater that zero, though leaving the relation $\widehat{k}_x^2 + \widehat{k}_y^2 + \widehat{k}_z^2 = 1$ unchanged, we obtain a evanescent form for the displacement fields,

$$
\begin{aligned}
\vec{u}_P &= A(\widehat{a}_x \pm i\gamma_\alpha \widehat{a}_z)\ \exp[\mp(\omega/c)\gamma_\alpha z]\ \exp[i\omega t - i(\omega/c)x)], \\[2mm]
\vec{u}_{SV} &= B(\mp i\gamma_\beta \widehat{a}_x + \widehat{a}_z)\ \exp[\mp(\omega/c)\gamma_\beta z]\ \exp[i\omega t - i(\omega/c)x)], \quad (2.12) \\[2mm]
\vec{u}_{SH} &= C\widehat{a}_y\ \exp[\mp(\omega/c)\gamma_\beta z]\ \exp[i\omega t - i(\omega/c)x)],
\end{aligned}
$$

where

$$\gamma_\alpha = \left(1 - \tfrac{c^2}{\alpha^2}\right)^{1/2}, \quad \gamma_\beta = \left(1 - \tfrac{c^2}{\beta^2}\right)^{1/2}. \quad (2.13)$$

There is only a regular solution that satisfies the free surface boundary condition. This solution is a combination of evanescent P and SV wave

traveling along the x axis:

$$
\begin{aligned}
\vec{u} =\ & A(\vec{a}_x - i\gamma_\alpha \vec{a}_z) \exp[-(\omega/c)\gamma_\alpha z] \exp[i\omega t - i(\omega/c)x] \\
& + B(i\gamma_\beta \vec{a}_x + \vec{a}_z) \exp[-(\omega/c)\gamma_\beta z] \exp[i\omega t - i(\omega/c)x]
\end{aligned}
\tag{2.14}
$$

This will represents waves traveling in the positive x direction with phase velocity c. Its evanescent character can be seen in the decaying exponential with increasing z, (provided $\gamma_\alpha, \gamma_\beta$ are real, that is, $c < \beta$). Applying the boundary condition on the free surface (Ben-Menahem and Singh, 1981, p. 114), one obtains the relations

$$
\begin{aligned}
2\gamma_\alpha A + i\left(2 - \tfrac{c^2}{\beta^2}\right) B &= 0, \\
-i\left(2 - \tfrac{c^2}{\beta^2}\right) A + 2\gamma_\beta B &= 0,
\end{aligned}
\tag{2.15}
$$

and therefore, the condition

$$
\left(2 - \frac{c^2}{\beta^2}\right)^2 - 4\gamma_\alpha \gamma_\beta = 0
\tag{2.16}
$$

This condition is known as the *Rayleigh equation*. It can be shown that, provided that $\beta < \alpha$, a $c < \beta$ exists (and independent of ω) that satisfies Rayleigh equation.

A real representation of a Rayleigh wave configuration can be written as

$$
\vec{u} = A\left\{\hat{a}_x D_x(z) \sin[\omega t - (\omega/c)x] + \gamma_\alpha \hat{a}_z D_z(z) \sin[\omega t - (\omega/c)x]\right\}, \tag{2.17}
$$

with depth functions $D_x(z)$ and $D_z(z)$ of the form

$$
D_x(z) = \exp[-(\omega/c)\gamma_\alpha z] - \left(1 - \frac{c^2}{2\beta^2}\right) \exp[-(\omega/c)\gamma_\beta z], \tag{2.18}
$$

$$
D_z(z) = -\exp[-(\omega/c)\gamma_\alpha z] + \left(1 - \frac{c^2}{2\beta^2}\right)^{-1} \exp[-(\omega/c)\gamma_\beta z]. \tag{2.19}
$$

The Rayleigh waves are a surface phenomenon. They are inhomogeneous plane waves with vanishing amplitude at greater and greater depths. Their polarization can be described as retrograde elliptical at the surface. At a depth $h = 1 - (c^2/\beta^2)$, where $D_x(z)$ goes through a zero, they change this behaviour to prograde elliptical.

In the half-space earth model we have enumerated all possible characteristic configurations. However, in a more complicated earth model with different layers in depth, new types of configurations appear.

Let us consider the simple case of a single layer over a half-space model. The generalization of the Rayleigh wave configurations to this case gives rise to new phenomenology. The different solutions can be classified into branches ($M_1, M_2, ...$) and these branches into modes ($M_{11}, M_{12}, ..., M_{21}, ...$) (Ben-Menahem and Singh, 1981, p. 116-120). All these solutions have a decaying behaviour in the half-space. The part of the solutions inside the layer can have oscillatory behaviour or exponential (growing and decaying) behaviour. With the "M_1 branch" term one indicates oscillatory symmetric modes of the free surface. The energy of this configurations is concentrated mainly in the free surface. On the other hand, "M_2 branch" indicates antisymmetric modes of the free surface. In this case the energy is concentrated mainly in the interface. Within each branch there are different solutions indicated by the symbols $M_{11}, M_{12}, M_{13}, \cdots$ and $M_{21}, M_{22}, M_{23}, \cdots$. M_{11} and M_{21} are the fundamental modes of branch M_1 and M_2 respectively. In this study we will concentrate in the fundamental mode of the branch M_1 (M_{11}), that is the mode with mayor energy concentration in the free surface.

The most important feature of all these modes is that on them the phase

velocity c depends on the frequency ω. This gives a dispersive character to the Rayleigh waves. The specific form of $c(\omega)$ for each mode depends on depth and properties of the layer with respect to the half-space. In more general situations one can have an earth model with multiple layers or even a continuously changing structure in depth. In these cases too, $c(\omega)$ will depend on the specific structure in depth of the earth. This is the crucial factor in this thesis. We will extract information about the structure of the earth by looking at the dispersion curves $c(\omega)$ of Rayleigh waves and of a new surface wave configurations that exist in a multilayer earth: *Love waves*.

2.5 LOVE WAVES

In a half-space earth model there is no possibility of having an evanescent SH configuration. From equations (2.12), the displacement at any point of the medium would be given by

$$\vec{u}_{SH} \;=\; C\hat{a}_y \; \exp[\mp(\omega/c)\gamma_\beta z] \; \exp[i\omega t - i(\omega/c)x]. \qquad (2.20)$$

This confines the energy to propagate along the free surface with exponential decay away from the $z = 0$. The stress free boundary condition at the surface $z = 0$ yield

$$\mu C(\omega/c)\gamma_\beta = 0. \qquad (2.21)$$

Therefore, $C = 0$ implies that in the case of a homogeneous half-space medium Love waves do not exist.

Consider however a half-space covered with a homogeneous layer of thickness H. The free surface is taken as the plane $z = 0$. From equations

(2.12) and (2.8)

$$
\vec{u} = \begin{cases}
\hat{a}_y\{A \, \exp[-i(\omega/c)\eta_1 z] + B \, \exp[i(\omega/c)\eta_1 z]\} \times & \exp[i\omega t - i(\omega/c)x)], \\
& (0 < z < H), \\
\\
C\hat{a}_y \, \exp[-(\omega/c)\gamma_2 kz] \, \times \exp[i\omega t - i(\omega/c)x)], \\
& (z > H),
\end{cases}
\tag{2.22}
$$

where

$$
\eta_1 = \left(\tfrac{c^2}{\beta_1^2} - 1\right)^{1/2}, \quad \gamma_1 = \left(1 - \tfrac{c^2}{\beta_1^2}\right)^{1/2}.
\tag{2.23}
$$

The traction at the free surface must be zero and the displacements and the tractions must be continuous across the interface. These conditions yield (Ben-Menahem and Singh, 1981, p. 106)

$$
A - B = 0,
$$

$$
A \, \exp[-i(\omega/c)\eta_1 H] + B \, \exp[i(\omega/c)\eta_1 H] - C \, \exp[-(\omega/c)\gamma_2 H] = 0,
$$

$$
A \, \exp[-i(\omega/c)\eta_1 H] - B \, \exp[i(\omega/c)\eta_1 H] + iC\tfrac{\mu_2\gamma_2}{\mu_1\eta_1} \, \exp[-(\omega/c)\gamma_2 H] = 0.
\tag{2.24}
$$

The solution of these equations leads to a dispersion relation, that gives the phase velocity as a function of the frequency (or period),

$$
\tan((\omega/c)\eta_1 H) = \frac{\mu_2\gamma_2}{\mu_1\gamma_1}.
\tag{2.25}
$$

Using the explicit expressions of η and γ we arrive at

$$
\tan\left(H\omega\sqrt{\frac{1}{\beta_1^2} - \frac{1}{c^2}}\right) = \frac{\mu_2\sqrt{1/c^2 - 1/\beta_2^2}}{\mu_1\sqrt{1/\beta_1^2 - 1/c^2}}
\tag{2.26}
$$

and therefore a dispersion curve $c = c(\omega)$.

It is clear from Eq. (2.23) that $c < \beta_2$, because otherwise, $\vec{u}$ will not tend to zero as $z \to \infty$. Furthermore, if η_1 is purely imaginary, Eq.(2.25) becomes

$$
-\gamma_1 \tanh((\omega/c)\gamma_1 H) = \left(\frac{\mu_2}{\mu_1}\right)\gamma_2,
\tag{2.27}
$$

which has no relevant solutions for $\omega > 0$ because the two sides are of opposite signs. Therefore, η_1 is real, i.e. $\beta_1 < c$. Then $\beta_1 < c < \beta_2$, which implies that the shear-wave velocity in the layer has to be less than the shear-wave velocity in the half-space. Only in this case (typical in real situations) will one have surface Love waves.

Equation (2.25) (or (2.26)) is a transcendental equation. For any value of c in the interval $\beta_1 < c < \beta_2$, it determines a set of possible values of $(\omega/c)\eta_1 H$, the first in the interval $(0, \pi/2)$, the second in the interval $(\pi, 3\pi/2)$, and so on. As in the dispersive case of Rayleigh waves one has different modes of propagation. Let us reiterate that the dispersion equation shows that the phase velocity, c, of Love waves is not a fixed constant but depends on the particular value of ω. Waves with different frequencies will have, in general, different phase velocities.

2.6   SURFACE WAVES AND EARTH STRUCTURE

For frequencies in which the finiteness of the Earth can be neglected, the traveling wave description just given provides us with a qualitative description of the different oscillatory phenomena one sees in the earth surface and interior. An earthquake, or any other earth cataclysm, excites all these traveling-wave modes, and they are detected by worldwide seismic networks.

Surface waves, that is, Rayleigh and Love waves, propagate along the Earth's surface, whereas body waves, P and S waves, propagate through its interior. For laterally homogeneous medium models, Rayleigh waves are radially polarized and exist at any free surface, whereas Love waves

are transversely polarized and require some velocity increase with depth (or a spherical geometry) to exist. They differ from body waves in many respects. They travel slower, their amplitude-decay with range is generally much less, and their velocities are strongly frequency dependent. Their amplitude distribution over depth is stationary with horizontal position (apart from an overall multiplicative factor describing the horizontal spreading). Therefore, the geometrical spreading effects are much less on surface waves than on body waves, for which the energy spreads both horizontally and vertically down into the Earth's interior.

Surface waves are generally the strongest arrivals recorded at teleseismic distances and they provide some of the best constraints on Earth's shallow structure and low-frequency source properties. They also form the longest and strongest portion of a seismic record excited by explosions and shallow earthquakes. Traversing areas with diverse geologic structures, they incorporate information on the properties of these areas, which is best reflected in the dispersion, the dependence of velocity on frequency. Long-period surface waves, with periods of 10 to 200 s, have been a valuable source of information on both the Earth structure and the seismic source mechanism. Their phase velocities, group velocities, (see below) and attenuation characteristics have been useful in delineating the structure of the crust and upper mantle in various regions of the Earth. Their source spectra and radiation patterns have contributed to the determination of seismic moment, focal mechanisms, and focal depths of remote events (Tsai and Aki, 1969 and 1970). They also supply crucial data for discriminating earthquakes from underground explosions.

In this thesis I will be concerned with the measurement of the disper-

sion relations for surface waves based on seismic records. The last part of this chapter will review some elementary concepts on phase and group velocities.

2.7 PHASE AND GROUP VELOCITIES

We saw that in the infinite homogeneous and isotropic earth model, the structural parameters λ, μ and ρ can be encoded in the phase velocities α and β of plane P and S waves. In the same way, in a layered half-space earth model, (or with a continuously varying structure in depth), the structural $\lambda(z)$ and $\mu(z)$ can be encoded in the dispersive phase velocities $c_R(\omega)$ and $c_L(\omega)$ of inhomogeneous plane Rayleigh and Love waves, respectively.

Taking the traveling phase of surface inhomogeneous plane wave solutions

$$\exp[i\omega t - i(\omega/c)x], \tag{2.28}$$

one realizes that its wave number is $k = \omega/c(\omega)$ and from here one can find a relation $\omega = \omega(k)$. Obviously, from this relation the phase velocity can be defined as $c = \omega/k$. The definition of group velocity is $U = d\omega/dk$. Now, this definition can be written as

$$\frac{1}{U(\omega)} = \frac{1}{c(\omega)} - \frac{\omega}{c^2(\omega)}\frac{dc(\omega)}{d\omega}, \tag{2.29}$$

or

$$U(\omega) = c(\omega)\left[1 - \frac{\omega}{c(\omega)}\frac{dc(\omega)}{d\omega}\right]^{-1} = c(T)\left[1\frac{T}{c(T)}\frac{dc(T)}{dT}\right]^{-1}. \tag{2.30}$$

We can gain insight on the meaning of group velocity with the the following exercise. Imagine a plane wave composed of the addition of a narrow Gaussian distribution of monochromatic waves around some fixed

frequency ω_0:

$$A = \int dk \frac{1}{\sqrt{2\pi}\sigma} \exp\left[-\frac{(k-k_0)^2}{2\sigma^2}\right] \exp[i\omega(k)t - ikx]. \qquad (2.31)$$

If the Gaussian function is narrow enough one can approximate the frequency by a straight line $\omega \simeq \omega_0 + U(k_0)(k-k_0)$. Then we can write

$$A = \int dk \frac{1}{\sqrt{2\pi}\sigma} \exp\left[-\frac{(k-k_0)^2}{2\sigma^2}\right] \exp[i\omega_0 t - ik_0 x] \exp[iU(k_0)(k-k_0)t - i(k-k_0)x],$$
$$(2.32)$$

and integrating

$$A = \exp[i\omega_0 t - ik_0 x] \exp\left[-\frac{[U(k_0)t - x]^2\sigma^2}{2}\right]. \qquad (2.33)$$

What we obtain is a monochromatic plane wave, with frequency ω_0 (the central frequency of the Gaussian distribution) and a phase moving at $c_0 = \omega_0/k_0$ velocity, modulated by a Gaussian envelope moving at a velocity $U(k_0)$, that is, at the group velocity for frequency ω_0. The group velocity can be associated with the velocity of propagation of information by modulating a carrier frequency.

3. THEORY OF THE GROUP VELOCITY MEASUREMENT

The development of numerical techniques in the last quarter of the last century has resulted in considerable progress in measurements of dispersion curves (Dziewonski and Hales, 1972; Keilis-Borok, 1986). The measurement of these dispersion curves, in general, is complex because the seismogram consists of a complex sum of normal modes. Others factors that can affect the measurements are multipathing and background noise. Knowledge of the group velocity dispersion curve is useful by itself, as they may be used in inversion processes to obtain shear-wave velocity structures (Keilis-Borok, 1986, Chapter 6). Also, comparison of calculated and observed group velocities represents a stringent test of the validity of a model. In addition, the ability to extract and determine group velocity curve is a prerequisite of a realizable phase velocity measurement.

One of the goals in this study is to isolate the fundamental mode in order to calculate the cleanest group velocity curve. The multiple filter (MFT) and the phase matched filter (PMF) technique are used to do this. In this chapter, I discuss the theoretical bases for calculating the group velocity dispersion curve, the multiple filter technique (MFT), and isolating the fundamental mode, phase matched filter (PMF) technique. Dziewonski et al. (1969) proposed the multiple filter technique (MFT) as an analytical method to obtain group velocity dispersion curves for a specific mode from complex multi-mode dispersion signal. Their development will be discussed in the first part of the chapter together with limitations and improvement of this technique. After applying the MFT, the disper-

sion curves are used as an input for the PMF technique proposed by Herrin and Gogorth (1977), which permits the isolation of the fundamental model and the cleaning of the signal. This allows us to reapply the MFT and calculate a more accurate group velocity dispersion curve of the fundamental mode (Fig. 3.1). The theoretical bases of the PMF will be discussed in the second part of the chapter.

To visualize the measurement process, we will dedicate the last part of the chapter to applying these techniques to some synthetic seismograms.

3.1 MULTIPLE FILTER TECHNIQUE

Dziewonski et al. (1969) developed the multiple filter technique (MFT) to determine the group velocities of dispersive waves. The basis of this method is the property of a dispersive signal that different frequency components arrive at different times. This method consists in the application of an array of narrow filters to the complex seismic signal. These narrow filters may resolve transient signals composed of several dominant periods that arrive at the recording station almost simultaneously. Using the filtered amplitude, I calculate the group velocity. It is assumed that the signal is a plane wave and that the instrumental response of the signal has been removed.

The Fourier transform of a signal $f(t)$ is defined as:

$$F(\omega) = \int_{-\infty}^{\infty} f(t)e^{-i\omega t} dt. \tag{3.1}$$

The complex spectrum of the signal $F(\omega)$ can be represented by its amplitude and phase functions

$$F(\omega) = |F(\omega)|e^{i\Phi(r,\omega,\theta)}. \tag{3.2}$$

Signal

MFT

Group velocity curve

PMF

Fundamental mode

MFT

Group velocity curve
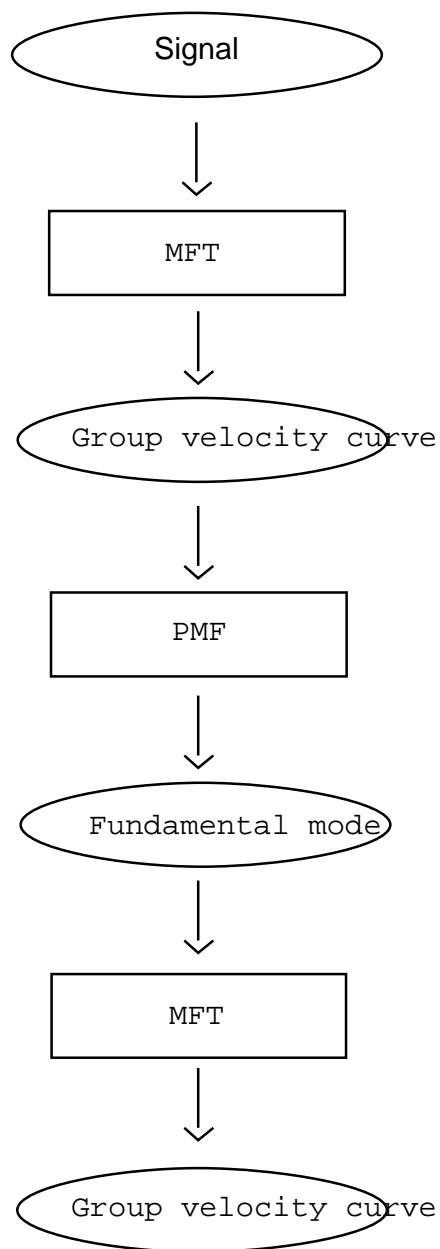
Figure 3.1: Flow chart of group velocity dispersion curve measurement. First the MFT is applied in order to obtain a provisional group velocity dispersion curve that is used as input in the PMF to isolate the fundamental mode. Once the fundamental mode is obtained, the MFT is applied again to this clean signal, containing only the fundamental mode, and an improved group velocity is calculated.

where r is the distance and θ is the azimuth. The phase term for the propagating surface wave is composed of the initial phase (source phase), $\phi(\omega, \theta)$, and the propagation term $k(\omega)r$:

$$\Phi(r, \omega, \theta) = -k(\omega)r + \phi(\omega, \theta). \tag{3.3}$$

A narrow filter is now applied to the signal. Dziewonski et al. (1969) used the following filter function:

$$H(\omega, \omega_n) = \exp\left[-\alpha \left(\frac{\omega - \omega_n}{\omega_n}\right)^2\right], \tag{3.4}$$

which has cutoff frequencies at $\omega = \omega_n \pm \omega_c$. This filter is a Gaussian filter, centered at the frequency w_n, with the parameter α controlling the width. The expression of the filtered signal is :

$$g_n(t) = \frac{1}{2\pi} \int_{\omega_n - \omega_c}^{\omega_n + \omega_c} F(\omega)H(\omega, \omega_n)e^{i\omega t}d\omega \tag{3.5}$$

where $g_n(t)$ is the resulting filtered signal. Substituting the definitions of $F(\omega)$ and $H(\omega)$, equations (3.4) and (3.5), the expression for the filtered signal becomes

$$g_n(t) = \frac{1}{2\pi} \int_{\omega_n - \omega_c}^{\omega_n + \omega_c} A(\omega) \exp[i(\omega t - k(\omega)r + \phi(\omega))] \exp\left[-\alpha \left(\frac{\omega - \omega_n}{\omega_n}\right)^2\right] \tag{3.6}$$

Following an scheme parallel to Bhattacharya (1983), it is assumed now that $A(\omega)$, $\phi(\omega)$ and $k(\omega)$ can be approximated in the vicinity of ω_n by the

first order Taylor series expansion:

$$A(\omega) = A(\omega_n) + \left(\frac{dA}{d\omega}\right)_{\omega=\omega_n} (\omega - \omega_n) = A_n + A'_n(\omega - \omega_n)$$

$$k(\omega) = k(\omega_n) + \left(\frac{dk}{d\omega}\right)_{\omega=\omega_n} (\omega - \omega_n) = k_n + k'_n(\omega - \omega_n) \qquad (3.7)$$

$$\phi(\omega) = \phi(\omega_n) + \left(\frac{d\phi}{d\omega}\right)_{\omega=\omega_n} (\omega - \omega_n) = \phi_n + \phi'_n(\omega - \omega_n),$$

where $k'_n = 1/U_n$ and U_n is the group velocity.

Now, $g_n(\omega)$ can be evaluated by substituting Eqs. (3.7) into (3.6), with the variable change $\omega - \omega_n = \bar{\omega}$

$$g_n(t) = \frac{1}{2\pi} A_n \exp[i(\omega_n t - k_n r + \phi_n)]$$

$$\times \int_{-\omega_c}^{\omega_c} (1 + p\bar{\omega}) \exp\left[i\beta\bar{\omega} - q\bar{\omega}^2\right], \qquad (3.8)$$

where

$$p = \frac{A'_n}{A_n},$$

$$\beta = (t - k'_n r + \phi'_n), \qquad (3.9)$$

$$q = \frac{\alpha}{\omega_n^2}.$$

From Abramowitz and Stegun (1965) (Equation 7.4.2), we use

$$\int \exp[-(ax^2 + 2bx + c)]dx =$$

$$= \frac{1}{2}\sqrt{\frac{\pi}{a}} \exp\left[\frac{b^2 - ac}{a}\right] erf\left[\sqrt{a}\, x + \frac{b}{\sqrt{a}}\right] + constant, \qquad (3.10)$$

where erf is the error function. Using (3.10), we have

$$\int_{-R}^{R}(1+px)\,\exp[-(ax^2+2bx+c)]dx$$

$$(3.11)$$

$$= -\tfrac{p}{2a}\exp[-(ax^2+2bx+c)]\,\Big|_{-R}^{R} + \Big(1-\tfrac{pb}{a}\Big)\,I\,\Big|_{-R}^{R}\,.$$

Thus,

$$\bar{I} = \int_{-\omega_c}^{\omega_c}(1+p\,\bar{\omega})\,\exp[i\beta\bar{\omega}-q\bar{\omega}^2]d\bar{\omega}$$

$$= -\tfrac{ip}{q}\,\exp[-q\omega_c^2]\sin(\beta\omega_c) + \tfrac{1}{2}\sqrt{\tfrac{\pi}{q}}\Big(1+\tfrac{ip\beta}{2q}\Big)\,\exp\Big[-\tfrac{\beta^2}{4q}\Big]$$

$$(3.12)$$

$$\times \Big[erf\Big(\sqrt{q}\,\omega_c - i\tfrac{\beta}{2\sqrt{q}}\Big) + erf\Big(\sqrt{q}\,\omega_c + i\tfrac{\beta}{2\sqrt{q}}\Big)\Big]\,,$$

using the relation $erf(-z)=-erf(z)$. Therefore the expression for $g_n(t)$ is

$$g_n(t) = \frac{A_n}{2\pi}\,\exp[i(\omega_n t - k_n r + \phi_n)]\,\bar{I}. \qquad (3.13)$$

The series approximation of complex error function (Abramowitz and Stegun, 1965, equation 7.1.29) is

$$erf(x+iy) = erf(x) + \frac{\exp[-x^2]}{2\pi x}[1-\cos(2xy)+i\sin(2xy)]+..., \quad (3.14)$$

If q is large enough in equation (3.12), the term with $1/\sqrt{q}$ can be neglected, using the first term in the above series approximation. Under this condition, we can express $g_n(t)$ as

$$g_n(t) = \tfrac{A_n}{2\pi}\,\exp[i(\omega_n t - k_n r + \phi_n)]erf(\sqrt{q}\,\omega_c)$$

$$(3.15)$$

$$\times \Big[-\tfrac{ip}{q}\,\exp[-q\omega_c^2]\sin(\beta\omega_c) + \tfrac{1}{2}\sqrt{\tfrac{\pi}{q}}\Big(1+\tfrac{ip\beta}{2q}\Big)\,\exp\Big[-\tfrac{\beta^2}{4q}\Big]\Big].$$

Expressing $g_n(t)$ by its modulus and its phase, $g_n(t) = |g_n(t)| \exp[i\Theta_n]$, where

$$|g_n(t)| = \frac{A_n}{2\pi}\sqrt{\frac{\pi}{q}}\sqrt{1 + \left(\frac{p\beta}{2q}\right)^2} \exp\left[-\frac{\beta^2}{4q}\right] erf(\sqrt{q}\,\omega_c),$$

(3.16)

$$\Theta_n = \omega_n t - k_n r + \phi_n + \arctan\left[\frac{p\beta}{2q}\right].$$

the extreme positions of $|g_n(t)|$ are given by

$$\left(\frac{p}{2q}\right)^2 \beta^3 + \left(1 - \frac{p^2}{2p}\right)\beta, = 0 \tag{3.17}$$

which has the solutions

$$\beta = 0,$$

$$\beta = \pm\sqrt{2\left(1 - \frac{2q^2}{p^2}\right)}$$

(3.18)

If $(2q^2/p^2) > 1$ (i. e., $2\alpha/\omega_n^2 > A'_n/A_n$) then the only real solution is $\beta = 0$ and it is a maximum. With the following example we can see that the above condition is in general satisfied. For a value of $\alpha = 50$ (the most typical values used), the value of the spectral amplitude slope must be more than eight times higher than the amplitude value ($A'_n/A_n > 8$), at a frequency $\omega_n = 2\pi$, for β not to be a complex extreme. When I measure group velocities I assume that the only maximum corresponds to $\beta = 0$. Therefore, the group velocity can be obtain by following relation

$$\beta = 0 = t - k'_n r + \phi'_n. \tag{3.19}$$

Another assumption is that ϕ'_n is small enough that be can neglect in the analysis. This assumption can be relaxed if a two-station technique is used for great-circle paths of if the travel times are much greater that the source group delay ϕ'_n.

Therefore, the group velocity is the distance from the source to the receiver divided by the arrival time of the maximum of the envelope, $U_n = k'_n = r/t_n$, where t_n denotes the arrival time of the maximum of the envelope for the nth filter to the signal. Thus, the maximum of the envelope corresponds to the group travel time of the energy associated with the frequency ω_n. But it is worthy to remember that equation (3.13) was obtained using the first-order expansion of $k(\omega)$, $A(\omega)$ and $\phi(\omega)$. Substitution of the second-order terms leads to rather involved form of $|g_n(t)|$ and it will be shown later that in these cases, the maximum of the envelope does not, in general, correspond exactly to the group travel time.

The precision of measurement of group velocity by a bandpass filtration technique is subject to the assumptions the either (i) filters are very narrow, which means that α is high and $1/\sqrt{q}$ may be neglected with respect to $\sqrt{q}$ and $\alpha/\omega_n^2 > A'_n/A_n$, or (ii) the approximations expressed in (3.7) are valid.

Problems arise when the variation of amplitude with frequency and the variation with frequency of the group velocity can not be neglected. Applying MFT to synthetic seismograms, Dziewonski and Hales (1972) showed that group velocity determination by MFT has systematic errors when the group velocity changes rapidly with frequency and these errors can be reduced with increase of α. Herrmann (1973) noted that the variation of group velocity with frequency causes an error in amplitude determination by MFT.

Note also that the use of the filtered output to estimate phase travel time will be affected by the shape of the signal amplitude spectrum (3.16b). The magnitude of these errors, examining $\Theta_n(t)$, will depend on the group

velocity and the rate of the slope and value of the spectral amplitude.

To clarify the processes in the MFT, I present the flow chart of this technique in the Figure 3.2.

3.1.1 WHY A GAUSSIAN FILTER?

One important thing to considerate is the resolution of the filtering function in the immediate vicinity of each center frequency and velocity value. We require the resolution to be good. If we define the following integral as a measure of the duration of a time signal,

$$D_t^2 = \int_{-\infty}^{\infty} t^2 |f(t)|^2 dt, \tag{3.20}$$

and measure the frequency domain duration as

$$D_\omega^2 = \int_{-\infty}^{\infty} \omega^2 |F(\omega)|^2 d\omega, \tag{3.21}$$

then the uncertainty principle states for a time function, $f(t)$, vanishing at infinity faster than $t^{-1/2}$, that

$$D_t^2 D_\omega^2 \geq \left(\frac{\pi}{2}\right)^{\frac{1}{2}}. \tag{3.22}$$

The equality holds only for Gaussian signals [Percival and Walden (1993), p. 74].

D_t^2 and D_ω^2 represent measures of the time and frequency resolution. It is known that the improvement of the time domain resolution can be achieved only at the expense of frequency domain resolution. It is obvious, from (3.22) that there is an advantage in using a filter for which this expense is the least.

MFT
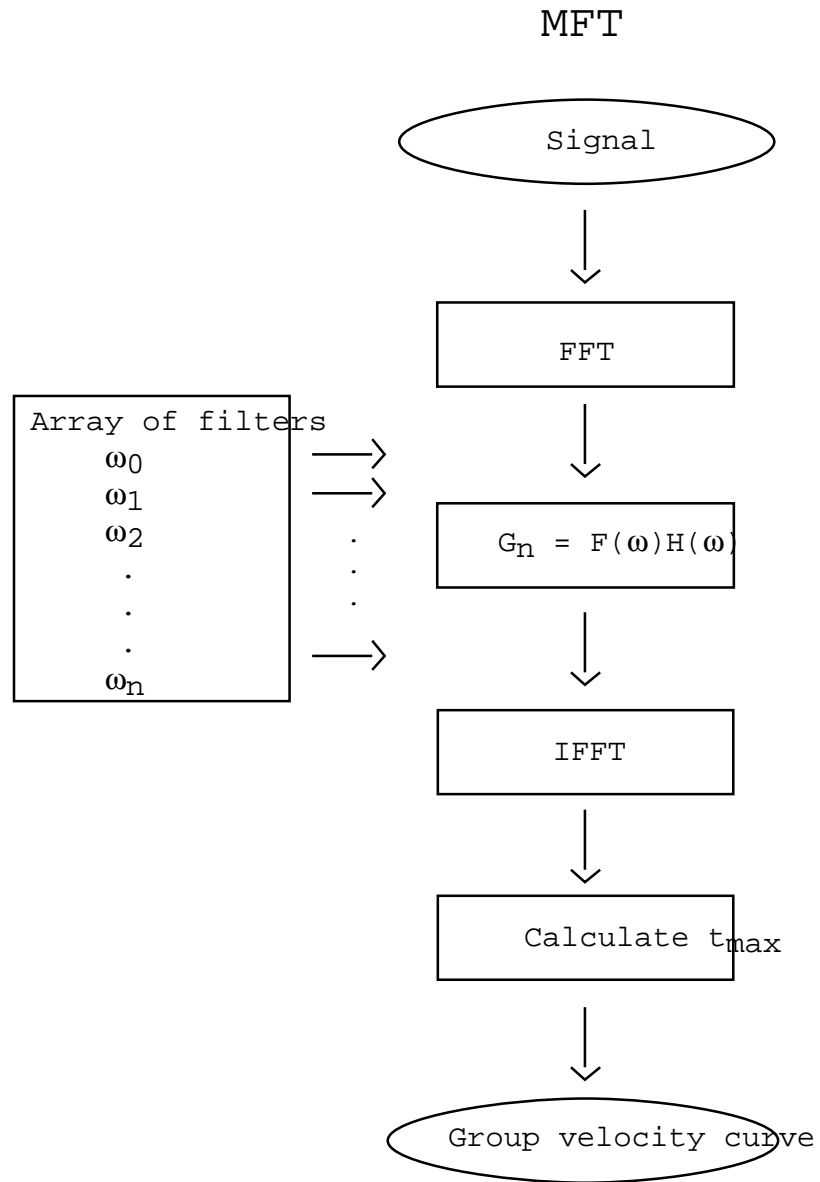
Figure 3.2: Flow chart of MFT. Following Fourier transform of the signal, an array of filters are convolved with our signal. After that the inverse Fourier transform is applied to the filtered signal. The travel time of the maximum of the envelope is the group travel time. The group velocity is the distance dividing by this time.

If ω_n denotes the center frequency for the Gaussian filter, in the frequency domain the Gaussian filter can be expressed as :

$$H_n(\omega) = \exp\left[-\alpha\left(\frac{\omega - \omega_n}{\omega_n}\right)\right] \tag{3.23}$$

The inverse Fourier transform of $H_n(\omega)$ is

$$h_n(t) = \frac{\sqrt{\pi}\,\omega_n}{2\alpha}\,\exp\left[-\frac{\omega_n^2\,t^2}{4\alpha}\right]\cos(\omega_n t) \tag{3.24}$$

Looking the expressions (3.23) and (3.24), the resolution is controlled in both domains by the parameter α. Improved resolution in one domain causes the opposite effect in the other, but the value of the product of the RMS durations of the Gaussian function, $D_\omega.D_t$, remains constant.

Selection of a particular filter width represents a compromise between the time and frequency domain resolution and depends on the level of noise, the character of the dispersion curve and the degree of contamination from energy belonging to other modes of propagation.

3.1.2   EFFECT OF MODAL INTERFERENCE

Until now, the theoretical discussion has been limited to the case in which only one mode is present in the signal. But the seismic signal is a complex signal, composed for different modes and noise. This complexity sets limitations to our approach of the problem.

At short periods, problems arise because of the presence of more than a single surface wave mode (Fig 3.3). Because the signal spectrum of these periods is a superposition of modal contributions, the resultant spectrum is highly oscillatory (see section 3.3) making analysis difficult. Herrmann (1973) showed the limitation of the multiple filter technique for the effect of modal interference.
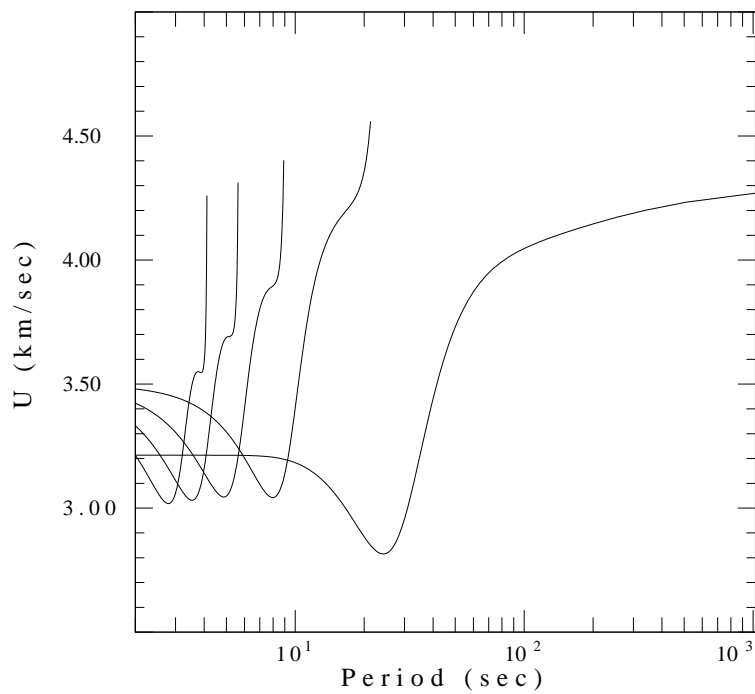
Figure 3.3: Group velocity curves for the first five modes for the Earth model used in section 3.3.

Following Herrmann (1973), ignoring the source amplitude spectral shape, the filtered multi-mode signal can be expressed as

$$g(t,r) = \frac{\omega_n}{2\pi}\sqrt{\frac{\pi}{\alpha}}\sum_{j=0}^{M} A_j(\omega_n, r)\, exp\left[-\frac{\omega_n^2}{4\alpha}\left(t - \frac{r}{U_{nj}}\right)^2\right] \qquad (3.25)$$

where the subscript j designates the value of a quantity for the jth mode.

Dziewonski et al. (1969) stated that the individual maxima of the envelope correspond to the arrivals of the group velocities of each mode. Because the modulus of (3.25) is a very complicated function then the accurate determination of group velocities, occurs when the envelope maxima are well separated.

Define the duration t_d of the resulting Gaussian envelope as the time from the peak value until the amplitude decreases to $\exp(-\pi)$ of the original value. In terms of α and T_n (the characteristic filter period), the duration has the expression:

$$t_d = T_n\sqrt{\frac{\alpha}{\pi}}. \qquad (3.26)$$

Therefore, for practical purposes, when the two equal amplitude maxima are separated by a time greater than $2t_d$ it is assumed that the two modes do not interfere. If the different mode maxima are separated enough, determinations of spectral amplitude, group velocity, and instantaneous phase can be made using the equation for only one mode (3.8), rather than (3.26). When the time separation of the arrivals of the two modes is less than $2t_d$, the maxima of the envelope will not correspond to the actual maxima of the individual modes. Examining (3.26), the resolution can be increased by decreasing the duration of the envelope of each mode by decreasing α. However, this would cause the amplitudes to reflect the variations of the group velocity with the frequency, requiring more terms in the

Taylor's expansion, equations (3.6) and (3.7)).

Narrow band-pass filtering of a dispersed surface wave can be used to determine the group velocities and spectral amplitudes of the various modes composing the signal under certain conditions. Namely, that the group-velocity arrivals of the individual modes are well enough separated in time that the contribution to the filtered signal do not interfere.

3.1.3 INCLUDING HIGHER ORDER IN THE TAYLOR'S EXPANSION

Bhattacharya (1983) approximated $A(\omega)$, $k(\omega)$ and $\phi(\omega)$, including a higher order terms in the Taylor's series expansion than Dziewonski et al. (1969) did, by considering

$$A(\omega) = A_n + A'_n(\omega - \omega_n),$$

$$k(\omega) = k_n + \frac{1}{U_n}(\omega - \omega_n) + k''_n \frac{1}{2}(\omega - \omega_n)^2, \qquad (3.27)$$

$$\phi(\omega) = \phi_n + \phi'_n(\omega - \omega_n) + \frac{1}{2}\phi''_n(\omega - \omega_n)^2.$$

Substituting the above approximation into (3.6), the new expression is similar to (3.8), with the same p and β, but changing q by q'

$$
\begin{aligned}
g_n(t) &= \frac{1}{2\pi} A_n \, \exp[i(\omega_n t - k_n r + \phi_n)] \\
&\times \int_{-\omega_c}^{\omega_c} (1 + p\bar{\omega}) \, \exp\left[i\beta\bar{\omega} - q'\bar{\omega}^2\right],
\end{aligned} \qquad (3.28)
$$

where

$$p = \tfrac{A_{n}}{A_n},$$

$$\beta = t - \tfrac{r}{U_n} + \phi'_n,$$

(3.29)

$$q' = \tfrac{1}{2}i(rk''_n - \phi'') + \tfrac{\alpha}{\omega_n^2}$$

Writing $q' = \rho \exp(i\Psi)$, with

$$\rho = \sqrt{\left[\left(\tfrac{\alpha}{\omega_n^2}\right)^2 + \left(\tfrac{rk''_n - \phi''_n}{2}\right)^2\right]},$$

(3.30)

$$\Psi = \arctan \frac{\tfrac{1}{2}(rk''_n - \phi''_n)}{\tfrac{\alpha}{\omega_n^2}},$$

and using (3.10) and (3.11), as I did before, the solution for (3.28) is

$$g_n(t) = \tfrac{A_n}{2\pi} \exp[i(\omega_n t - k_n r + \phi_n)]$$

$$\times \quad \{-\tfrac{ip}{\rho} \exp[i(-\Psi + \rho\omega_c^2 \sin\Psi) + \rho\omega_c^2 \cos\Psi] \sin(\beta\omega_c)$$

$$+ \quad \tfrac{1}{2}\sqrt{\tfrac{\pi}{\rho}} \left(1 + \tfrac{p\beta}{2\rho}\sin\Psi + \tfrac{ip\beta}{2\rho}\cos\Psi\right)$$

(3.31)

$$\times \quad \exp\left[i\left(-\left(\tfrac{\Psi}{2}\right) + \left(\tfrac{\beta^2}{4\rho}\right)\sin\Psi\right) - \left(\tfrac{\beta^2}{4\rho}\right)\cos\Psi\right]$$

$$\times \quad [erf(\xi_- + i\eta_-) + erf(\xi_+ + i\eta_+)]\},$$

where

$$\xi_{\mp} = \sqrt{\rho}\,\omega_c \cos\left(\tfrac{1}{2}\Psi\right) \mp \tfrac{\beta}{2\sqrt{\rho}}\sin\left(\tfrac{1}{2}\Psi\right),$$

(3.32)

$$\eta_{\mp} = \sqrt{\rho}\,\omega_c \sin\left(\tfrac{1}{2}\Psi\right) \mp \tfrac{\beta}{2\sqrt{\rho}}\cos\left(\tfrac{1}{2}\Psi\right).$$

If ρ is large enough than be can neglect $1/\sqrt{\rho}$ with respect to $\sqrt{\rho}$ then we can apply the approximation describes in (3.14), keeping the first term.

Therefore,

$$
\begin{aligned}
g_n(t) \;=\;& -\tfrac{p A_n}{2\rho\pi}\,\exp[-\rho\omega_c^2\,\cos\Psi]\,\sin(\beta\omega_c) \\[2ex]
& \times\;\; \exp[i(\omega_n t - k_n r - \phi_n - \Psi - \rho\omega_c^2\,\sin\Psi + \tfrac{2}{\pi})] \\[2ex]
& +\;\; \tfrac{A_n}{2\pi}\sqrt{\tfrac{\pi}{\rho}}\,\sqrt{\left[1 + \tfrac{p\beta}{\rho}\,\sin\Psi + \left(\tfrac{p\beta}{2\rho}\right)^2\right]}\,\exp[-(\tfrac{\beta^2}{4\rho)\cos\Psi})] \\[2ex]
& \times\;\; erf[\sqrt{\rho}\,\omega_c\,\cos(\tfrac{1}{2}\Psi)]\,\exp[i(\omega_n t - k_n r + x)],
\end{aligned}
\tag{3.33}
$$

where

$$
x = \phi_n - \frac{\Psi}{2} + \frac{\beta^2}{4\rho}\,\sin\Psi + \lambda,
\tag{3.34}
$$

and

$$
\lambda = \arctan\left[\frac{\tfrac{p\beta}{2\rho}\,\cos\Psi}{\left(1 + \tfrac{p\beta}{2\rho}\,\sin\Psi\right)}\right].
\tag{3.35}
$$

As before we look for the maximum of the envelope of $g_n(t)$. For that we shall find the value of β at the point of the maximum. It difficult to calculate the maximum of the envelope of (3.33) using both terms on the right side of the expression. We can simplify by neglecting the first term with respect to the second term when the envelope of the second term reaches maximum. We can do it if $\rho\omega_c^2$ is large enough (Bhattacharya, 1983). Thus, near the maximum of second term, we may approximate the filtered signal by

$$g_n(t) \;=\; \tfrac{A_n}{2\pi}\sqrt{\tfrac{\pi}{\rho}}\;\sqrt{\left[1 + \tfrac{p\beta}{\rho}\sin\Psi + \left(\tfrac{p\beta}{2\rho}\right)^2\right]}\;\exp\left[-\left(\tfrac{\beta^2}{4\rho}\right)\cos\Psi\right]$$

<div align="right">(3.36)</div>

$$\times\quad erf\left(\sqrt{\rho}\,\omega_c\cos\left(\tfrac{1}{2}\Psi\right)\right)\;\exp[i(w_n t - k_n r + x)].$$

where the amplitude and phase of (3.36) are, respectively,

$$|g_n(t)| \;=\; \tfrac{A_n}{2\pi}\sqrt{\tfrac{\pi}{\rho}}\;\sqrt{\left[1 + \tfrac{p\beta}{\rho}\sin\Psi + \left(\tfrac{p\beta}{2\rho}\right)^2\right]}\;\exp\left[-\left(\tfrac{\beta^2}{4\rho}\right)\cos\Psi\right]$$

<div align="right">(3.37)</div>

$$\times\quad erf\left(\sqrt{\rho}\,\omega_c\cos\left(\tfrac{1}{2}\Psi\right)\right),$$

and

$$\Theta = w_n t - k_n r + x. \tag{3.38}$$

The extreme positions of $|g_n(t)|$ are the solutions of the following equation

$$\cos\Psi\left(\frac{p}{2\rho}\right)^2\beta^3 + \frac{p\sin\Psi\cos\Psi}{\rho}\beta^2 + \left(\cos\Psi - \frac{p^2}{2\rho}\right)\beta - p\sin\Psi = 0 \tag{3.39}$$

or

$$\beta = \left[p\tan\Psi - \left(\beta^2\frac{p}{\rho}\sin\Psi + \beta^3\left(\frac{p}{2\rho}\right)^2\right)\right]\bigg/\left(1 - \frac{p^2}{2\rho\cos\Psi}\right). \tag{3.40}$$

Since, as it was assumed before that ρ is large then it may be taken as an initial approximation (see Bhattacharya, 1983)

$$\beta = p\tan\Psi. \tag{3.41}$$

The maximum of the envelope of the filtered signal occur at :

$$t_m = \frac{r}{U_n} - \phi'_n + p\tan\Psi \tag{3.42}$$

or,

$$U_n = \frac{r}{t_m + \phi'_n - p \tan \Psi} \tag{3.43}$$

Thus, if $p \tan \Psi$ is ignored, (3.43) reveals that the measured group velocity by MFT will be higher than the true value if $p \tan \Psi$ is negative or lower than the true value if $p \tan \Psi$ is positive. For all combinations of signs of Ψ and p, MFT distorts the computed group velocity to the group velocity of neighboring frequency at which the amplitude spectrum is rapidly changing.

3.1.4 INSTANTANEOUS FREQUENCY

One way to improve the group velocity measurements when the amplitude changes with frequency, is to consider that the measured group velocity corresponds to the instantaneous frequency ($< \omega >$) instead of the central filter frequency ω_n.

If the complex signal in the time domain is

$$g_n(t) = |g_n(t)| \exp[i\Theta(t)], \tag{3.44}$$

the instantaneous frequency is defined (see Keilis-Borok (1986), p. 137) as

$$\Omega(t) = \frac{d\Theta(t)}{dt}. \tag{3.45}$$

The property

$$< \Omega >=< \omega >, \tag{3.46}$$

(Keilis-Borok (1986), p. 140) tells that when Ω is measured an approximate value of the mean frequency around which the signal spectrum is concentrated can be obtained. Only in the case when the slope in spectrum

amplitude is equal to zero does the mean frequency coincide with the central frequency of the narrow-filter. We can improve the measurement by assuming that the mean instantaneous frequency is the frequency that corresponds to the value of the measured group velocity instead of the filter frequency.

From (3.15),

$$\Omega(t) = \frac{d\Theta(t)}{dt} = \omega_n + \frac{1}{1 + \left(\frac{p\beta}{2q}\right)^2}\left[\frac{p}{2q} + \frac{\beta}{2q}\frac{dp}{dt}\right] \tag{3.47}$$

If q is large it is assumed

$$\frac{1}{1 + \left(\frac{p\beta}{2q}\right)^2} \approx 1 \tag{3.48}$$

and neglecting the $p' = A_n''/A_n'$ term the expression for the instantaneous frequency is

$$\Omega(t) = \omega_n + \frac{p}{2q} \tag{3.49}$$

Examining the expressions (3.43) and (3.49)

$$
\begin{aligned}
p > 0 \implies & \left\{ \begin{array}{l} U_n > U_n(measured), \\[1em] \Omega > \omega_n \end{array} \right. \\[2em]
p < 0 \implies & \left\{ \begin{array}{l} U_n < U_n(measured), \\[1em] \Omega < \omega_n \end{array} \right.
\end{aligned}
\tag{3.50}
$$

this mean that the instantaneous frequency is shifted toward a direction that compensates the error in the group velocity measurement.

3.2 PHASE MATCHED FILTER

Herrin and Goforth (1977) proposed the phase matched filter technique (PMF) to remove the effect of noise and other modes from the seismic signal to isolate the fundamental mode. The PMF compresses the waveform into a narrow time window centered near zero time, allowing noise to be windowed out by taking the spectrum of this narrow window rather than the full signal time window. However, the amount of compression depends on how well the phase matched filter matches the actual phase of the signal. The PMF can be used to remove multipathing effects, isolate the fundamental mode and improve the signal-to-noise ratio.

Consider the cross-correlation of a signal, f(t), with a time function, h(t):

$$f(t) \otimes h(t) \Rightarrow |F(\omega)| \, |H(\omega)| \, exp[i(\Phi(\omega) - \sigma(\omega)]. \qquad (3.51)$$

Now we choose an $h(t)$ such that the Fourier phase is the same as $f(t)$ ($\sigma(\omega) = \Phi(\omega)$), as a phase matched filter with respect to the signal, then

$$f(t) \otimes h(t) \Rightarrow |F(\omega)| \, |H(\omega)|. \qquad (3.52)$$

There are different possible choices for $|H(\omega)|$

a) $|H(\omega)| = |F(\omega)|$

This maximizes the signal-to-noise power ratio assuming "white noise". For a low-level-noise signal, this give the best result.

b) $|H = (\omega)| = \frac{1}{|F(\omega)|}$

The output after this filter becomes the impulse function in the time domain, which maximizes the time resolution of the function but greatly reduces the signal-to-noise ratio. This is a good choice for interfering signal.

c) $|H = (\omega)| = 1$

This is a compromise between the time resolution and the signal-to-noise ratio criteria. In my measurements this will be the one that I use.

Herrin and Goforth (1977) refer to the zero-phase time-domain signal as the "pseudo-autocorrelation function". Assuming that the seismogram is composed of propagating normal modes, the signal can be expressed as

$$f(t) = \frac{1}{2\pi} \int_{-\infty}^{\infty} \sum_m |F_m(\omega)| \exp[\omega t - k_m(\omega)r + \phi_m(\omega)] d\omega \quad (3.53)$$

where $\phi_m(\omega)$ is source phase shift for the mth mode.

When the PMF technique is applied to the signal, $f(t)$, the pseudo-autocorrelation function has the expression

$$\psi_j(t) = \frac{1}{2\pi} \int_{-\infty}^{\infty} \exp[i\tilde{k}_j r] \sum_m |F_m(\omega)| \exp[\omega t - k_m(\omega)r + \phi_m(\omega)] d\omega, \quad (3.54)$$

where $\tilde{k}_j$ is an estimate of dispersive wavenumber of the jth mode of interest. Rewriting the above equation it is obtained

$$\psi_j(t) = \frac{1}{2\pi} \int_{-\infty}^{\infty} |F_j(\omega)| \exp\left[\left(\tilde{k}_j - k_j(\omega)\right) r + \phi_j(\omega)\right] \exp[\omega t] d\omega$$

$$(3.55)$$

$$+ \frac{1}{2\pi} \int_{-\infty}^{\infty} \sum_{m \neq j} |F_m(\omega)| \exp[\omega t - k_m(\omega)r + \phi_m(\omega)] d\omega.$$

If the source effect is removed and $\tilde{k}_j - k_j \approx 0$, the first integral in the right-hand side will be approximately zero-phase and will be concentrated around zero-lag. Time-windowing $\psi_j(t)$ with a symmetric and zero-phase window , $w(t)$, will remove the contribution of the other modes and noise to the signal, provided that they are separated enough from the zero-lag. Therefore, we can write that

$$\tilde{\psi}_j(t) = w(t)\psi_j(t) \quad (3.56)$$

Taking the Fourier transform of the windowed pseudo-autocorrelation function results in

$$|F_j(\omega)| \ \exp[i\delta k_j r] = \int_{-\infty}^{\infty} w(t)\psi_j(t) \ \exp[i\omega t]dt \qquad (3.57)$$

where

$$\delta k = \tilde{k}_j - k_j, \qquad (3.58)$$

or if we have not removed the source phase shift

$$\delta k = \tilde{k}_j - k_j + \frac{\phi_j}{r}. \qquad (3.59)$$

When r, the distance between the source and the receiver, is large enough we can neglect the source phase term in the above expression. Notice that there may be a residual phase ($\delta k \ r$), depending of the accuracy of the initial estimate of the wavenumber dispersion curve. To improve that we can use an iterative process with a new estimate of the wavenumber dispersion curve:

$$\tilde{k}_j^{new} = \tilde{k}_j - \delta k \qquad (3.60)$$

Then we can substitute this new value, $\tilde{k}_j^{new}$ in (3.55) and repeat the process again until the process converge.

A fundamental ambiguity is present in (3.57)

$$\exp[i\delta kr] = \exp[i\delta k \ r \pm i2n\pi]. \qquad (3.61)$$

To remove this ambiguity requires *a priori* knowledge of the location of the wavenumber at least at one frequency. This is possible if the data permits connecting the dispersion curve to global long period phase-velocity dispersion curves.

Herrin and Goforth (1977) described the computer algorithm used in the PMF technique. Here I present this algorithm with some details. To find a PMF for a given seismic signal, I use the following iterative process:

1. Input a trial group-velocity dispersion curve and an amplitude spectrum for the filter. We obtain this trial group velocity dispersion curve from the multiple filter technique describe in the section (3.2)

2. The group delay and the Fourier phase of the signal are related (Keilis-Borok, 1989, p. 137) by

$$t_{gr}(\omega) = -\frac{d\Phi(\omega)}{d\omega} \tag{3.62}$$

where t_{gr} is the group delay and $\Phi(\omega)$ is the spectral phase, then

$$\Phi(\omega_1) = \int_{\omega_0}^{\omega_1} t_{gr}(\omega)d\omega + \Phi(\omega_0). \tag{3.63}$$

This integral can have an additive constant without affecting the derivative group delay. Russell et al. (1987) show that the windowed pseudo-autocorrelation function is not biased by constant phase errors.

Using the epicentral distance and the dispersion curve, I calculate t_{gr}. With these group delay and (3.63) I obtain the Fourier phase of the phase matched filter.

3. I perform the cross-correlation of the signal with the phase matched filter calculated before (3.52) in the frequency domain. The amplitude of the phase matched filter is equal to unity ($|H(\omega)| = 1$)

4. After that I calculate the inverse Fourier transform to window the pseudo-correlation function in the time domain. The window function that I use is a Parzen window defined as

$$
w(t) = \begin{cases} 1 - 6\left(\frac{t}{M}\right)^2 + 6\left(\frac{|t|}{M}\right)^3 & |t| \le M/2 \\ 2\left(1 - \frac{|t|}{M}\right)^3 & M/2 < |t| \le M \\ 0 & |t| > M \end{cases} \tag{3.64}
$$

where M is the one-sided width of the Parzen window. The window size is proportional to the longest period in the signal. Russell (1987, section 4.1.3) discusses the bias of the Parzen window function, showing that the PMF in an iterative process can remove residual bias in phase, but not the bias in the spectral amplitude, that can be quite biased when there is significant curvature ($|F''(\omega)|$) in the amplitude spectrum.

5. Then I take this windowed pseudo-correlation function and obtain its spectral amplitude and phase.

6. I apply a first derivative smoothing condition, to the dispersion curve. This condition, with the approximations made (see section 3.2), is the same as imposing a condition for continuity of the second derivative of the Fourier phase spectrum. This is used to correct the group delay of the trial filter (3.53)

7. I return to the step 3, repeating the process until the phase spectra of the filter and the desired signal in the band of interest are identical.

3.3 EXAMPLE OF MULTIPLE FILTER AND PHASE MATCHED FILTER TECHNIQUES

As an example of the techniques described in previous sections, I apply them to some synthetic seismograms. These synthetic seismograms have been calculated using the mode summation code by R. B. Herrmann (Computer Programs in Seismology 3.1, Saint Louis University, 1996). To calculate them I utilize a simple earth model, a layer over a half-space and a strike-slip source with a strike = $0°$, a rake = $0°$, and dip = $45°$ at 40 km depth. The recording azimuth is $45°$. I only compute the first five modes (Fig. 3.4).

In the Figure 3.5, the synthetic seismograms for four different distances (1000 km, 2000 km, 3000 km and 4000 km) are presented. The increased dispersion with distance is easily seen.

The output of the MFT program is shown in Figure 3.6, where at the left of the figure is displayed the plot of the maximum values of the envelope amplitude per period, which are indicated with different symbols. At the right side is the plot of group velocity with period where the different colors represent different envelope amplitude values, with the highest amplitude in red. In the group velocity plot the fundamental mode is clearly seen by the gradation of color for periods larger than 10. For short periods the contributions of the higher modes are notable.

After picking the points that I think belong to the fundamental mode dispersion curve, I use these values as one of the input of the PMF technique. With that I isolate the fundamental mode. The comparison between the synthetic fundamental mode and the isolated fundamental mode us-
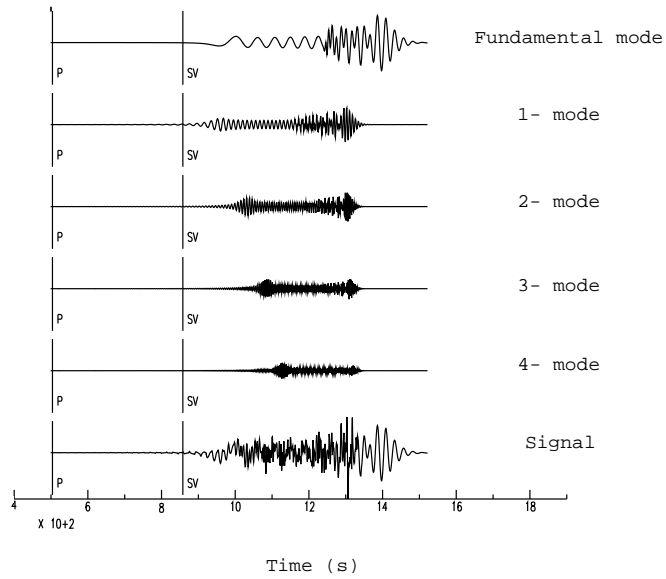
Figure 3.4: The first five modes and the complete modal summation at 4000 km

ing the PMF is presented in the Figures 3.7 and 3.8. Most of the differences between both signal are at short periods where the contributions of higher modes is important. The two signals in Figure 3.8 would be identical if low pass filtered.
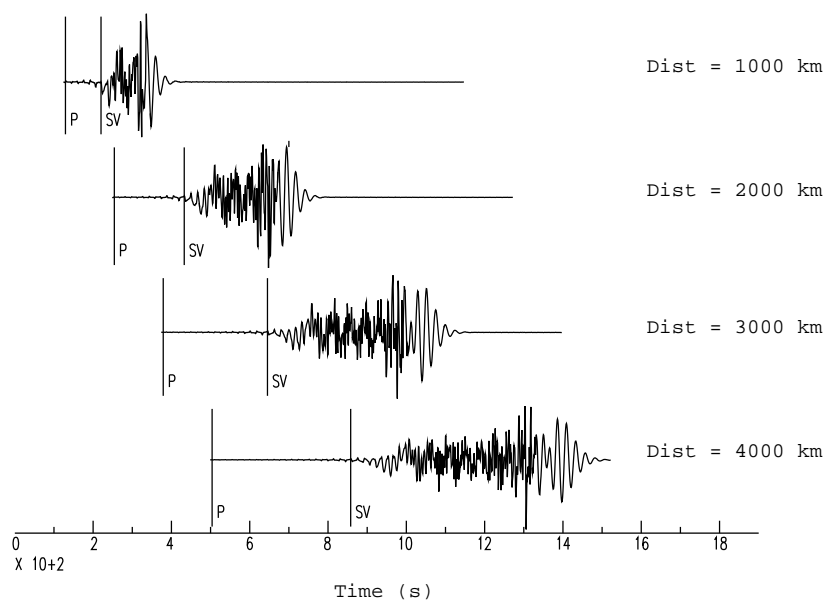
Figure 3.5: Synthetic Rayleigh waves at four different distances
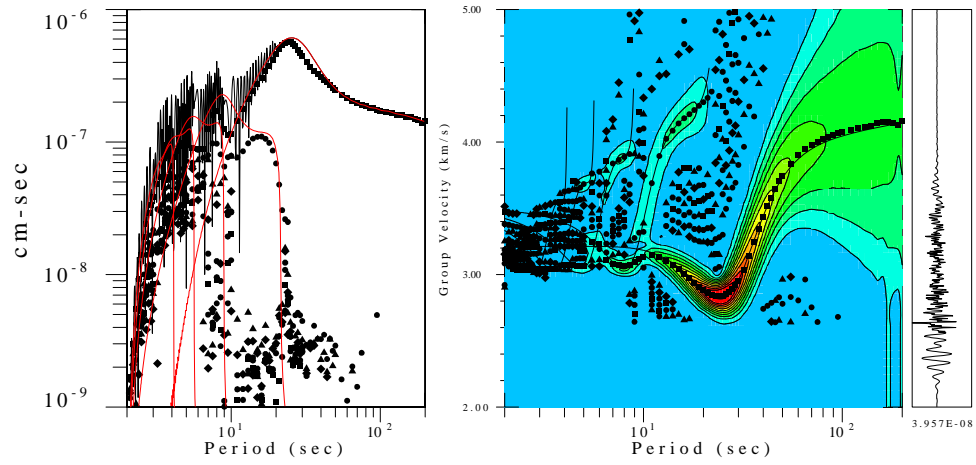
Figure 3.6: MFT at 4000 km. At the right side the plot of the group velocity dispersion curve with period is displayed; the color represents the filtered envelope values as a function of velocity and period. The red color represent the highest amplitude. The thin black lines, in this plot, are the theoretical group velocity dispersion curves for the earth model used in the synthetic computations. At the left side the plot shows the maximum amplitude values of the envelope (discrete symbol) per period. The red color lines show the amplitude of the different modes used in making the synthetic seismogram and with thin black line, the amplitude of the signal is plotted. The oscillation of the signal is due to the interferences of the higher modes
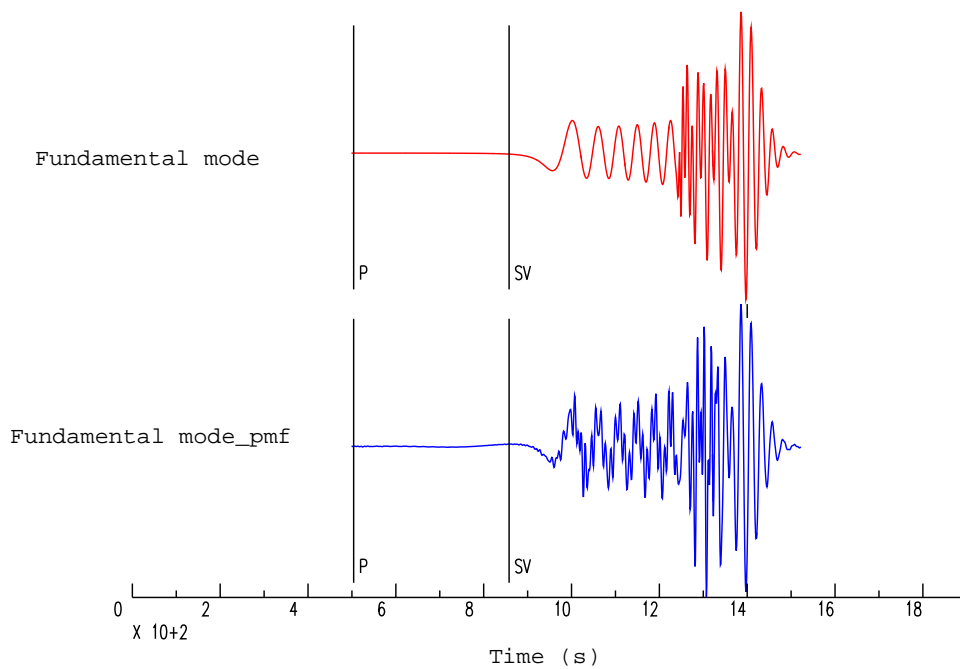
Figure 3.7: The original fundamental mode and the fundamental mode isolated by the PMF, for the signal at 4000 km
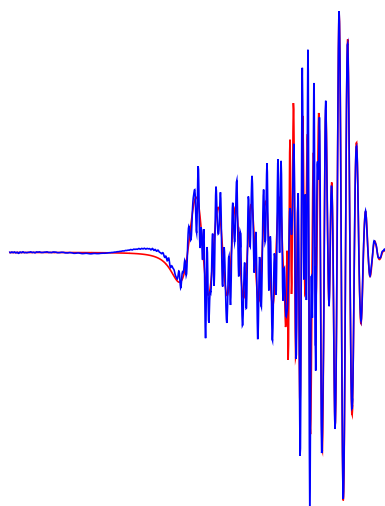
Figure 3.8: Superposition of the original fundamental mode and the output of PMF

4. GROUP VELOCITY MEASUREMENT

Using the methodology discussed in the Chapter 3, I calculate the group velocity dispersion curves for Rayleigh and Love waves. The data set consists of 50 events recorded by the Cooperative New Madrid Seismic Network (CNMSN) and the Southern Alabama earthquake (24 of October, 1997), which was recorded by 48 stations. The comparison of observed Rayleigh wave group velocity dispersion curves with the Stevens' model predictions is the main point of this chapter.

I start this Chapter with the a description of Stevens' model (Stevens and Adams, 1999). After that, I present the data set and the results of the test between the observations and the model predictions for the events recorded by CNMSN and for the Alabama earthquake.

4.1 STEVENS' MODEL

One of the motivations of this work is to test the Stevens' model. My intention is to check its performance for different ranges of periods by comparing its predictions with the group velocity dispersion curves that I have calculated. Before the presentation of the results I want to introduce the methodology under the Stevens' model.

This global model was created to identify and detect surface waves under a Comprehensive Nuclear-Test-Ban treaty at the International Data Center. The authors continue incorporating more data into this model to predict surface wave behavior more accurately.

Observed surface waves provide strong constraints on earth structure, so development of regional earth models can be a self-correcting process.

That is, surface wave dispersion and amplitude can be used to infer earth structure, and earth structure can be used to calculate surface-wave dispersion parameters. This is the basic idea of the project led by J. Stevens.

Stevens and Adams (1999) collected group and phase velocity data and performed global tomographic inversions, determining the shear velocity as a function of depth in discrete cells. This global model is divided in $1° \times 1°$ cells, each one associated with a particular Earth model type. Each model type consists of plane layers with uniform P and S velocities, density and Q (the thickness of the layer is obtained by previous studies). The layers extend to a depth of about 200 km. They treat the S-velocities as free parameters which are estimated by tomographic inversion of observations of phase and group velocity dispersion of surface waves. The surface wave dispersion observations come from :

1. A large data set of 84,966 phase velocity measurements taken from Curtis et al. (1998)

2. Global surface wave group velocities from earthquakes derived using PIDC GSETT3 data (Stevens and McLaughlin, 1988), augmented with more recent measurements derived from PIDC data, for a total of 1500 path at 6 frequencies from 0.02-0.06 Hz.

3. Surface wave phase and group velocity dispersion curves from underground nuclear test sites (Stevens, 1986; Stevens and McLaughlin, 1988), calculated from earth models for 270 paths (test site-station combinations) at 10 frequencies between 0.015 and 0.06 Hz.

4. Phase and group velocity measurements for western Asia and Saudi

Arabia from Mitchell et al. (1996) for 12 path at 17 frequencies between 0.012 and 0.14 Hz. A large data set of dispersion measurements from Saudi Arabia provided by St. Louis University (Mokhtar et al. personal communication)

5. Global phase velocity model of Ekstrom et al. (1996) for 9 periods between 35 and 150 seconds calculated for each $5°$ grid block from a spherical harmonic expansion of order l=40.

6. Group velocity measurements for Eurasia from Ritzwoller et al. (1996) and Levshin et al. (1996) for frequencies between 0.004 and 0.1 Hz with 500 to 5000 paths per frequency.

7. Group velocity measurements for South America and Antarctica provided by the University of Colorado (Vdovin et al.,1999; Ritzwoller et al., 1999).

Inversions are performed with P-wave velocities fixed (Crust2 or other studies) and with the P-wave velocities constrained by Poisson's ratio, and densities by Birch's Law. The inversions are limited to depths between 3 and 200 km, with fixed water layers and extended to greater depth using PREM (Dziewonski and Anderson, 1981). A smoothness condition that minimizes the change in adjacent layer velocities is also applied. The calculations are performed using the LSQR algorithm as described by Nolet (1987). Although surface-wave attenuation is not modeled in this inversions, the earth models include a Q structure based on PREM model in the mantle and on "Swanger's law" $Q = \beta/10$ where β is the shear velocity in m/s in each crustal layer (Stevens and Adams, 1999). The shallow layers

are too thin to be resolved by surface wave inversion, but are important to account for the effects of sediments and, for oceanic model types, the water column, because these layers have a strong effect on the higher frequencies, so these are fixed in the tomographic inversion. The parameters for these shallow layer are taken from other studies (e.g Mooney et al., 1988; Laske and Masters, 1997).

4.2 THE CNMSN EVENTS

The events used in this study were recorded by 8 Broadband stations belonging to CNMSN and BILLIKEN run by Saint Louis University (Fig 4.1 and Table 4.1).

Stations		
Name	Lat	Lon
BLO	39.1719	-86.5222
CCM	38.0555	-91.2445
FVM	37.984	-90.4260
MPH	35.123	-89.932
PLAL	34.9824	-88.0755
SIUC	37.7148	-89.2174
SLM	38.6362	-90.2362
UALR	34.7760	-92.3435
UTMT	36.3423	-88.8642

Table 4.1: Station locations

I calculate group velocity dispersion curves for 50 events recorded from 01/99 to 05/01 (Figure 4.2 and Table 4.2). The event distances range from teleseismic to local. Depending of the distance I use a different width parameter of the Gaussian filter, α which is represented by differences in color in Figure 4.2. In the event table I have assigned different letter for each α value used: $\alpha = 25$ with A, $\alpha = 50$ with B, $\alpha = 100$ with C, and $\alpha = 200$ with D. For a better exposition of the result, I have grouped the events by their locations; events in the same group have essentially the same path. These groups are noted in the last column of the table by a number.
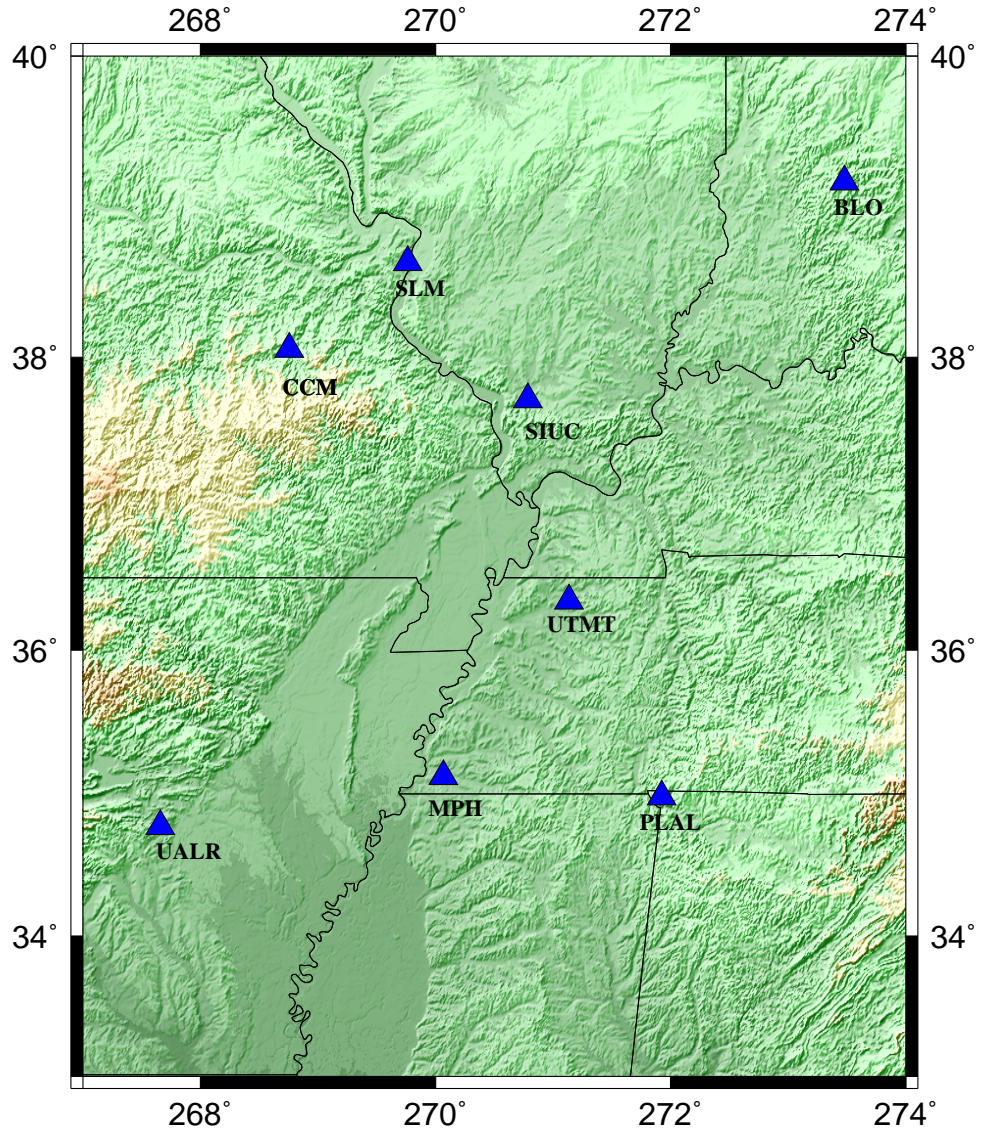
Figure 4.1: Cooperative New Madrid Seismic Network, broadband stations used in this study. CCM is a IRIS-Billiken station
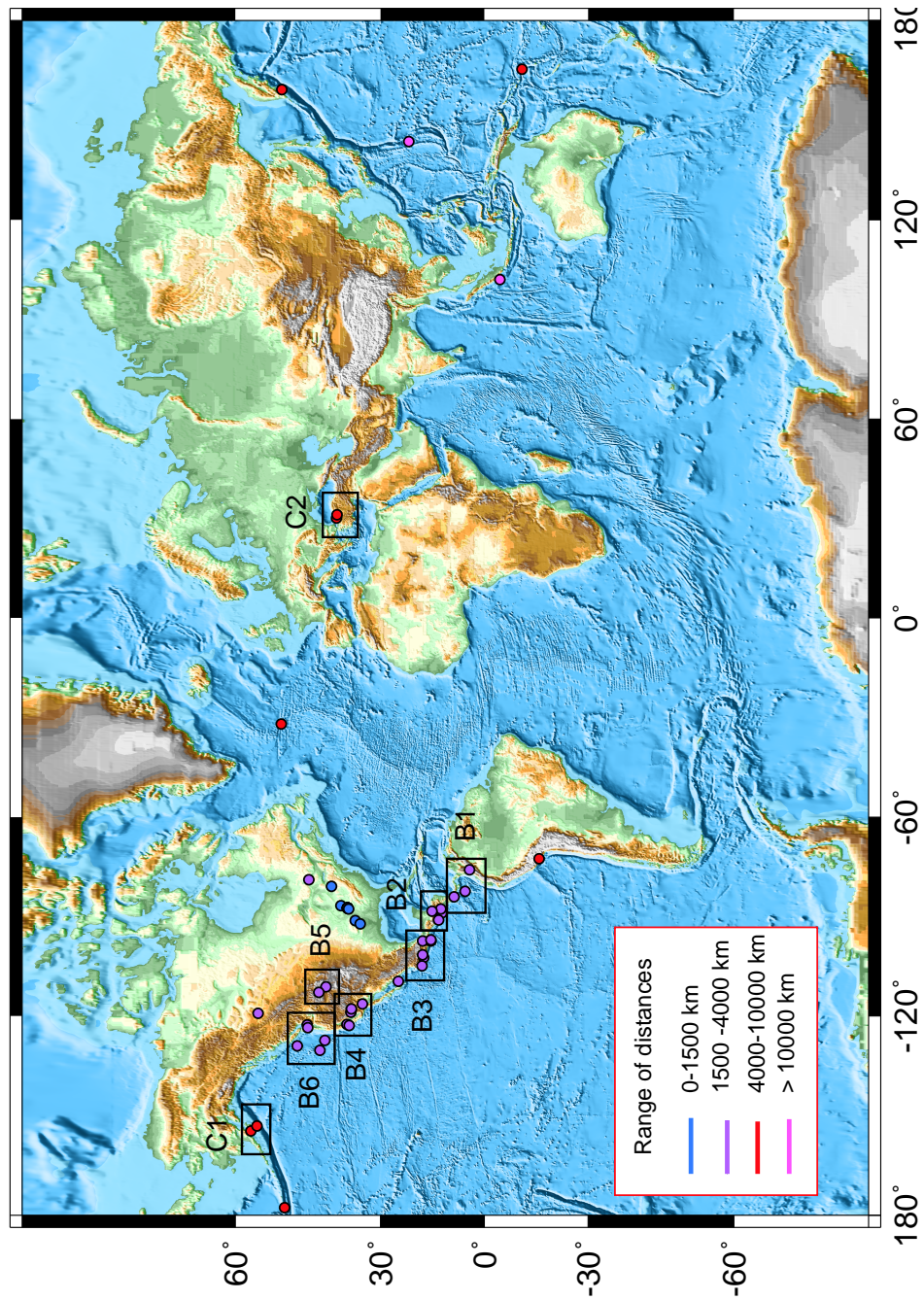
Figure 4.2: Event locations. The different colors correspond to different value of the width parameter, α, of the Gaussian filter: blue α=25, violet α=50, red α=100 and deep pink α=200. Source groups are indicated by the boxes.

4.2.1 GENERAL RESULTS

In this section I compare the observations to the Stevens' model. The results are presented for different range of distances (Figure 4.3). I select path ranges of 0-500 km, 0-1500 km, 1500-4000 km, and 4000-10000 km to focus on predictions for paths within the central U.S., for continental U.S. paths, and global paths. Most of the data used by Stevens and Adams (2000) have periods between 20 and 150 s. For the other periods, model based predictions based on CRUST2 (Mooney et al. 1998) for shorter periods, and PREM (Dziewonski and Anderson, 1981) for longer periods are used.

The whole result set of the differences between observations and Stevens' model predictions are displayed in Figure 4.3. To view the performance of the Stevens' model and the extrapolations made, I present expansions for different range of periods. These expansion are for periods shorter than 20 seconds in Figure 4.4, for periods in the range between 20 and 150 seconds in Figure 4.7 and for periods longer than 150 in Figure 4.13. After each expansion I present the histograms for some selected periods (Figures 4.5 for 5s, 4.6 for 10s, 4.8 for 20s, 4.9 for 50s, 4.10 for 70s, 4.11 for 100 s, 4.12 for 150s, 4.14 for 180s, 4.15 for 220s, 4.16 for 240s and 4.17 for 260s). These histograms permit a better visualization of the differences between observations and model predictions.

Events							
Name	Lat	Lon	M_w	Depth	n. Rayleigh	n. Love	clas
000101	46.87	-78.90	5.2	18	3	2	B
000414	39.86	-86.72	3.6	10.0	1	2	A
000506	-11.25	165.41	6.3	33.6	6	1	D
000602	44.50	-130.18	5.9	10	5	5	B 5
000604	-4.73	102.05	7.9	10	0	7	D
000711	57.58	-154.49	6.7	53.5	6	6	C 1
000720	38.34	-87.42	3.0	0.1	2	1	A
000727	38.26	-87.34	2.7	1.0	3	3	A
000805	38.25	-87.29	3.0	0.1	2	2	A
000809	18.19	-102.30	6.4	33.0	7	7	B 2
000811	38.25	-87.32	2.0	0.1	3	3	A
000817	38.26	-87.34	2.9	0.1	2	4	A
000822	36.486	-91.12	3.9	5.0	3	7	A
000831	38.28	-87.39	3.0	5.0	3	3	A
000903	38.38	-122.41	5.2	9.4	4	5	B 3
000918	25.28	-109.43	4.6	10	5	6	B
001005	38.23	-87.35	2.9	0.1	1	2	A
001207	38.00	-87.68	4.0	10.0	2	4	A
010111	49.24	-128.92	5.8	10	3	2	B 5
010113	12.77	-88.83	7.6	60.0	4	4	B 2
010126	41.99	-80.83	4.2	5.0	2	2	A
010228	47.2	-122.54	6.9	52.9	4	3	B 5
010414	56.35	-119.16	5.3	21.3	4	3	B
010421	43.16	-111.19	5.3	15.0	6	4	B 4
010428	18.60	-104.81	6.1	15.0	7	6	B 2
010504	35.24	-92.22	4.4	13.4	6	6	A
990125	4.45	-75.77	6.1	27.9	4	3	B 1
990308	52.13	159.32	6.7	33	5	4	C
990309	43.47	-127.26	5.1	10	6	6	B 5

Table 4.2: Events analyzed in this study. The different columns present latitude, longitude, moment magnitude, depth, number of Rayleigh dispersion curves, number of Love dispersion curves and the source group of the event. The letter refers to the distance and the α used in the MFT: A for $\alpha = 25$, B for $\alpha = 50$, C for $\alpha = 100$ and D for $\alpha = 200$. The group number indicates events with similar source-station path.

Events							
Name	Lat	Lon	M_w	Depth	n. Rayleigh	n. Love	clas
990310	52.31	-31.85	5.3	10	4	0	C
990320	51.61	-177.73	6.8	33	3	2	C
990331	5.8	-82.39	6.0	10	4	3	B 1
990403a	-16.39	-72.51	6.2	94	4	2	C
990403b	13.14	-87.66	5.7	33	4	5	B 2
990404	15.98	-97.25	5.1	33	4	0	B 2
990507	56.55	-153.04	6.1	33	3	0	C 1
990515	37.53	-118.82	5.6	5.7	3	3	B 3
990606	13.78	-90.90	6.1	33	5	5	B 2
990615	18.41	-97.34	6.7	79.6	6	5	B 2
990621	18.37	-101.39	5.7	72.7	6	1	B 2
990703	47.08	-123.46	5.9	40.6	7	3	B 5
990711	15.79	-88.26	6.6	10	4	4	B 2
990801	37.386	-117.73	5.7	8	6	6	B 3
990817	40.81	30.08	7.5	16.6	5	5	C 2
990818	37.91	-122.69	5.0	6.9	3	6	B 3
990820a	9.22	-84.05	6.7	33	5	5	B 1
990820b	44.78	-112.77	5.3	12	4	3	B 4
990930	16.04	-96.93	7.5	47.4	7	0	B 2
991016	34.60	-116.27	7.0	6.0	7	7	B 3
991112	40.77	31.15	7.2	10	7	6	C 2

Table 4.3: Continuation of table 4.2
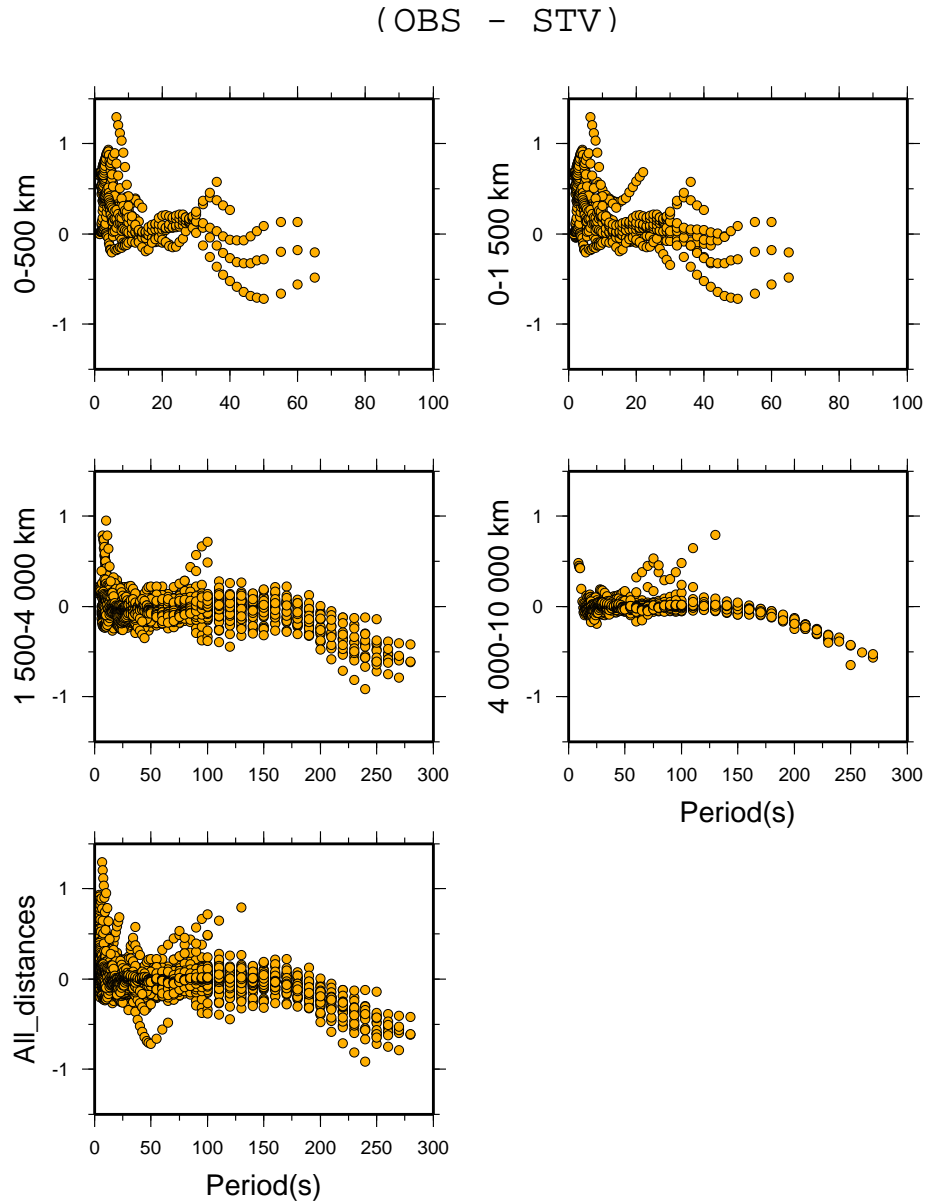
(OBS - STV)

Figure 4.3: Difference between observed and Stevens' model predictions for Rayleigh wave group velocity dispersion curves for the entire data set as a function of period. The results are displayed in different distance windows. The ordinate axes are group velocity values with the unit km/s.

(OBS - STV)

Figure 4.4: Expansion of Figure 4.3 for periods less than 20 s

Figure 4.5: Histogram at 5 seconds, showing the number of measurement corresponding to each value of the differences between observation and Stevens' model at 5 seconds period

Figure 4.6: Histogram at 10 seconds, showing the number of measurement corresponding to each value of the differences between observation and Stevens' model at 10 seconds period

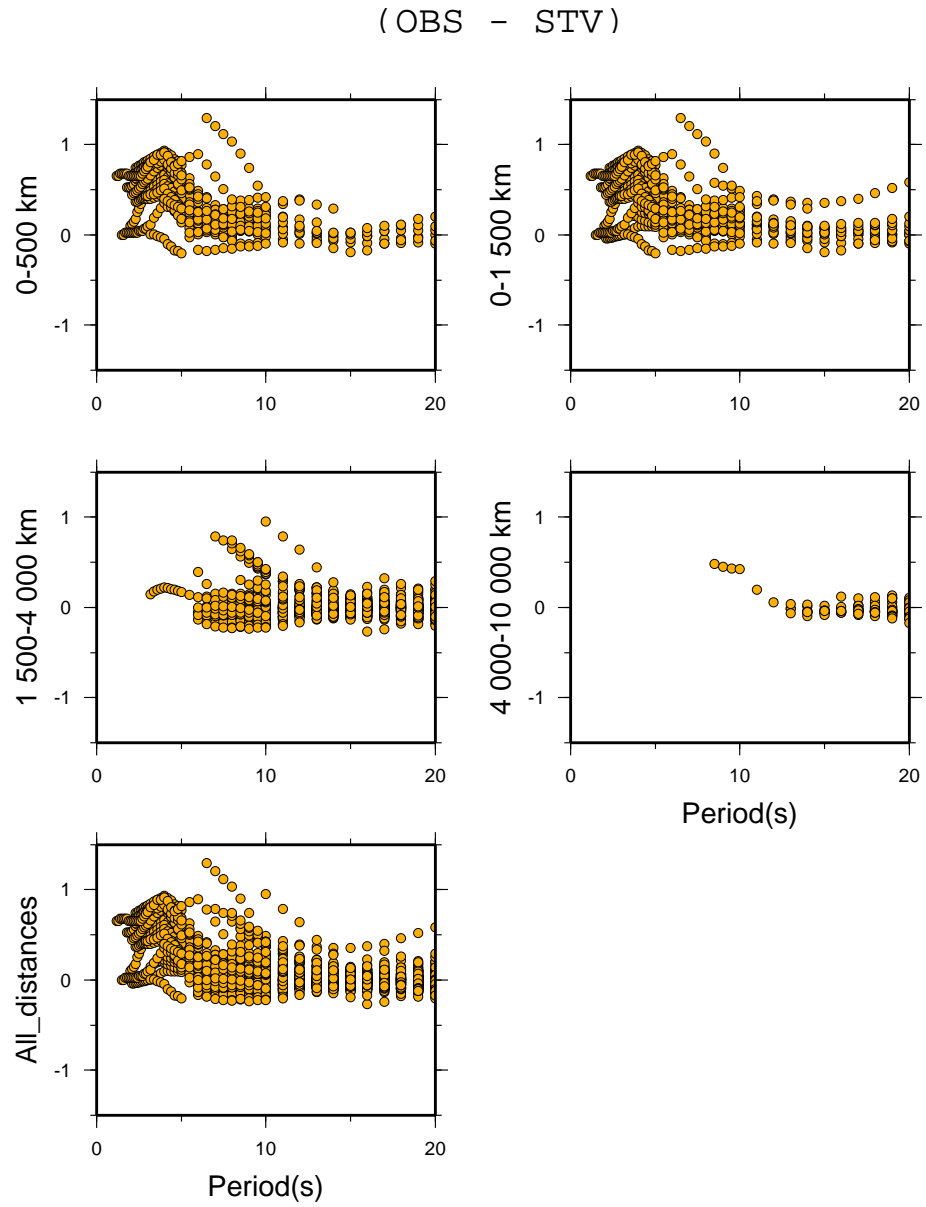Figure 4.7: Expansion of Figure 4.3 for periods between 20 and 150 s

Figure 4.8: Histogram at 20 seconds, showing the number of measurement corresponding to each value of the differences between observation and Stevens' model at 20 seconds period

Figure 4.9: Histogram at 50 seconds, showing the number of measurement corresponding to each value of the differences between observation and Stevens' model at 50 seconds period
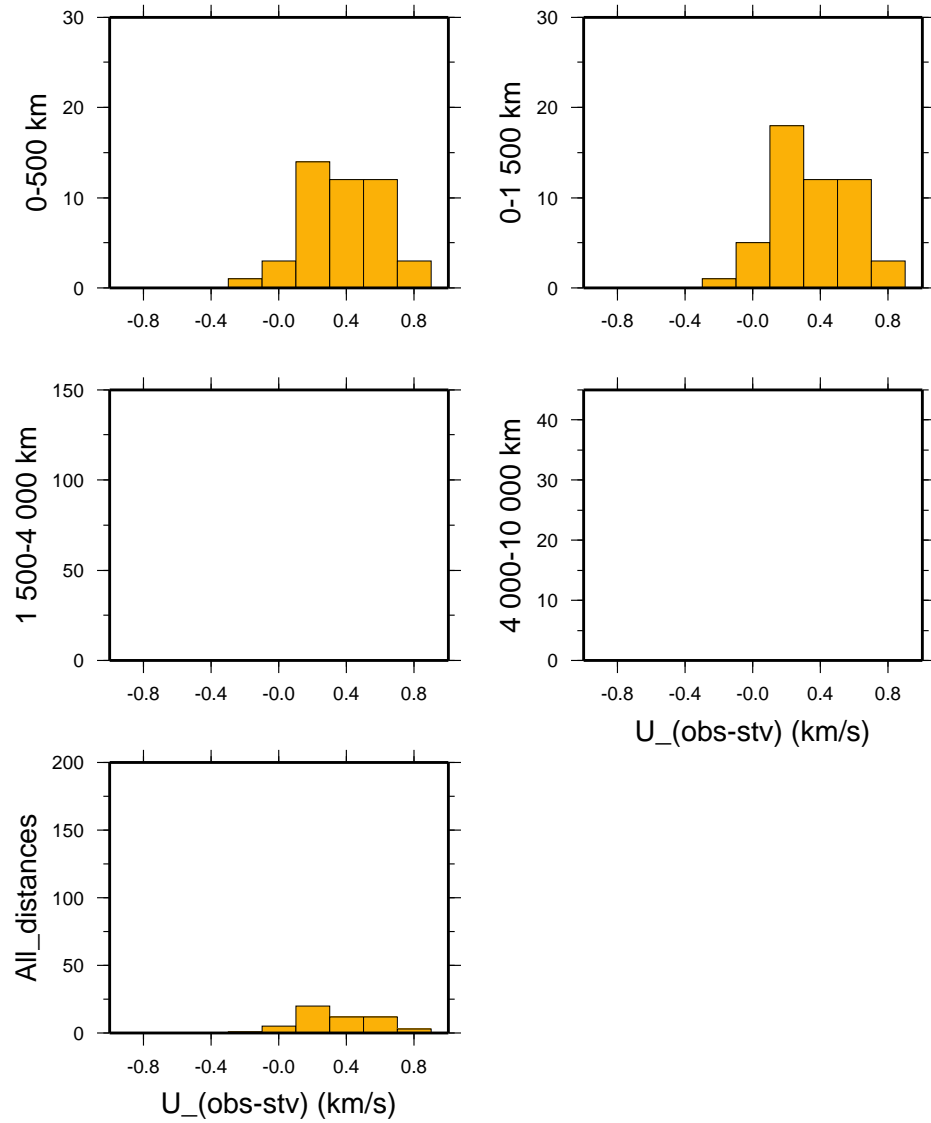
Figure 4.10: Histogram at 70 seconds, showing the number of measurement corresponding to each value of the differences between observation and Stevens' model at 70 seconds period

Figure 4.11: Histogram at 100 seconds, showing the number of measurement corresponding to each value of the differences between observation and Stevens' model at 100 seconds period
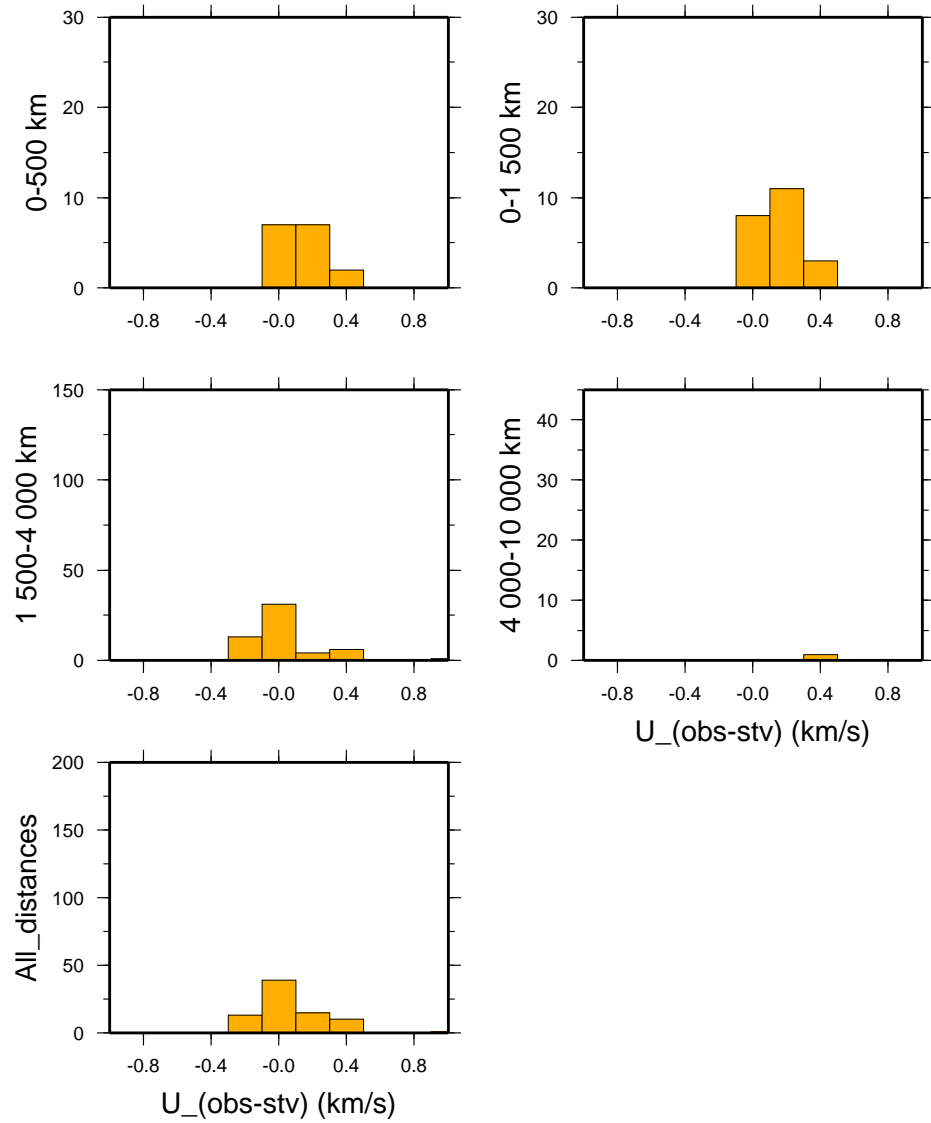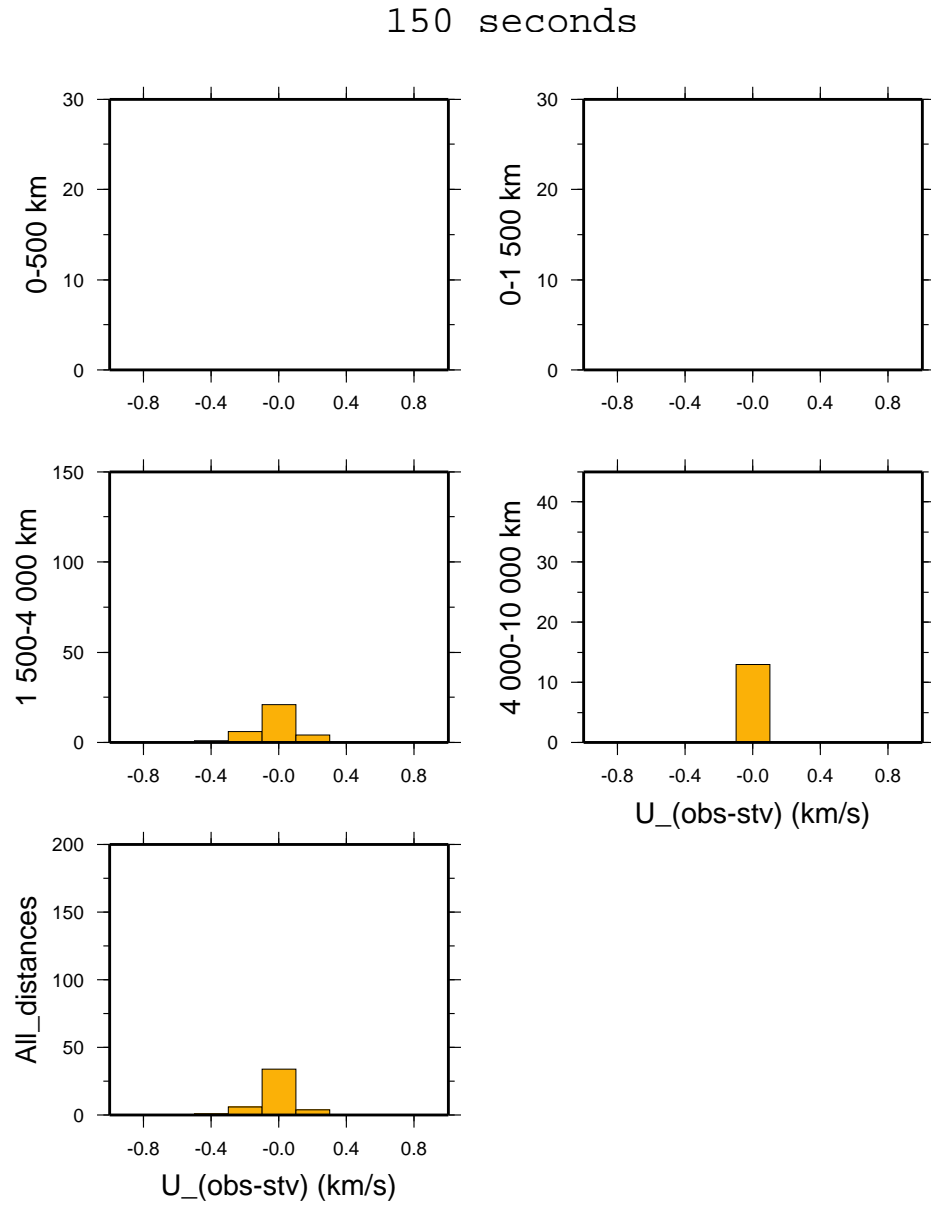
150 seconds

Figure 4.12: Histogram at 150 seconds, showing the number of measurement corresponding to each value of the differences between observation and Stevens' model at 150 seconds period
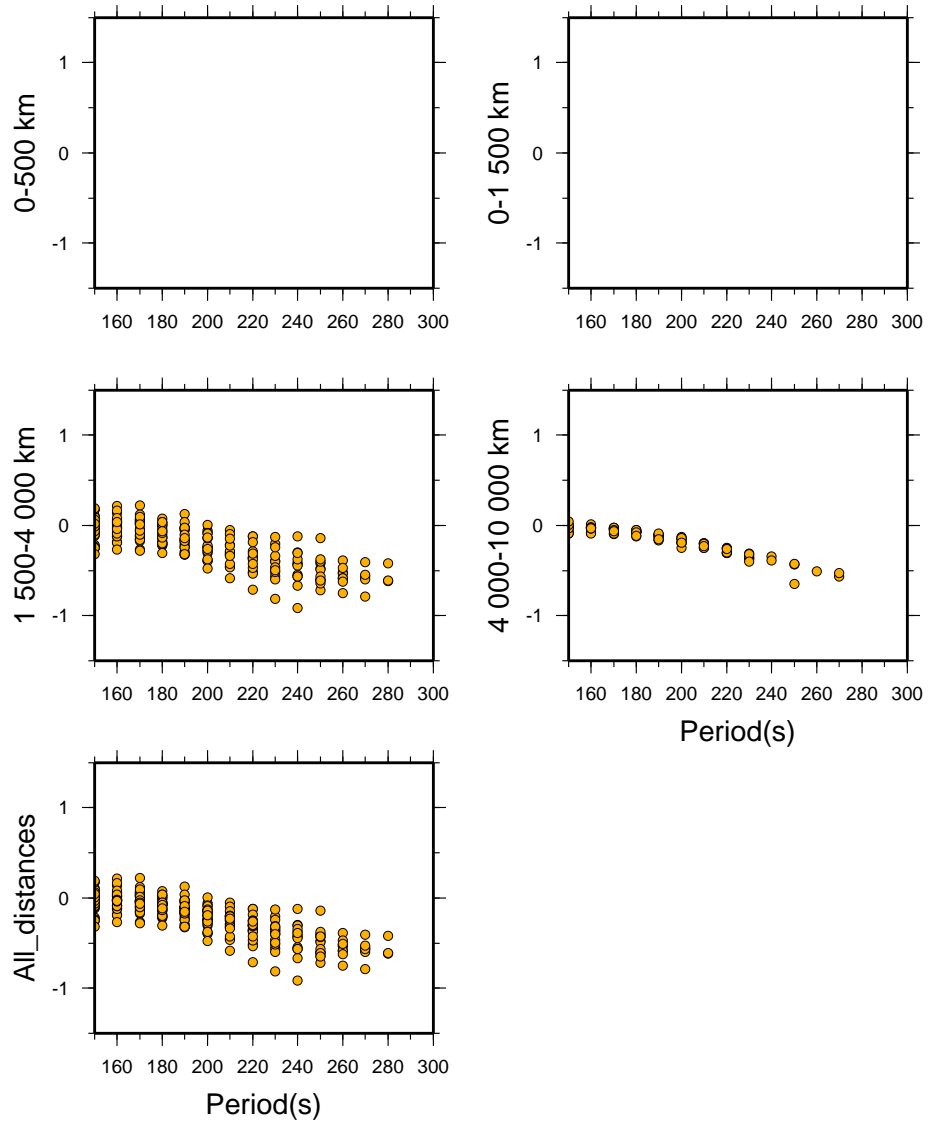
Figure 4.13: Expansion of Figure 4.3 for periods higher than 150 s
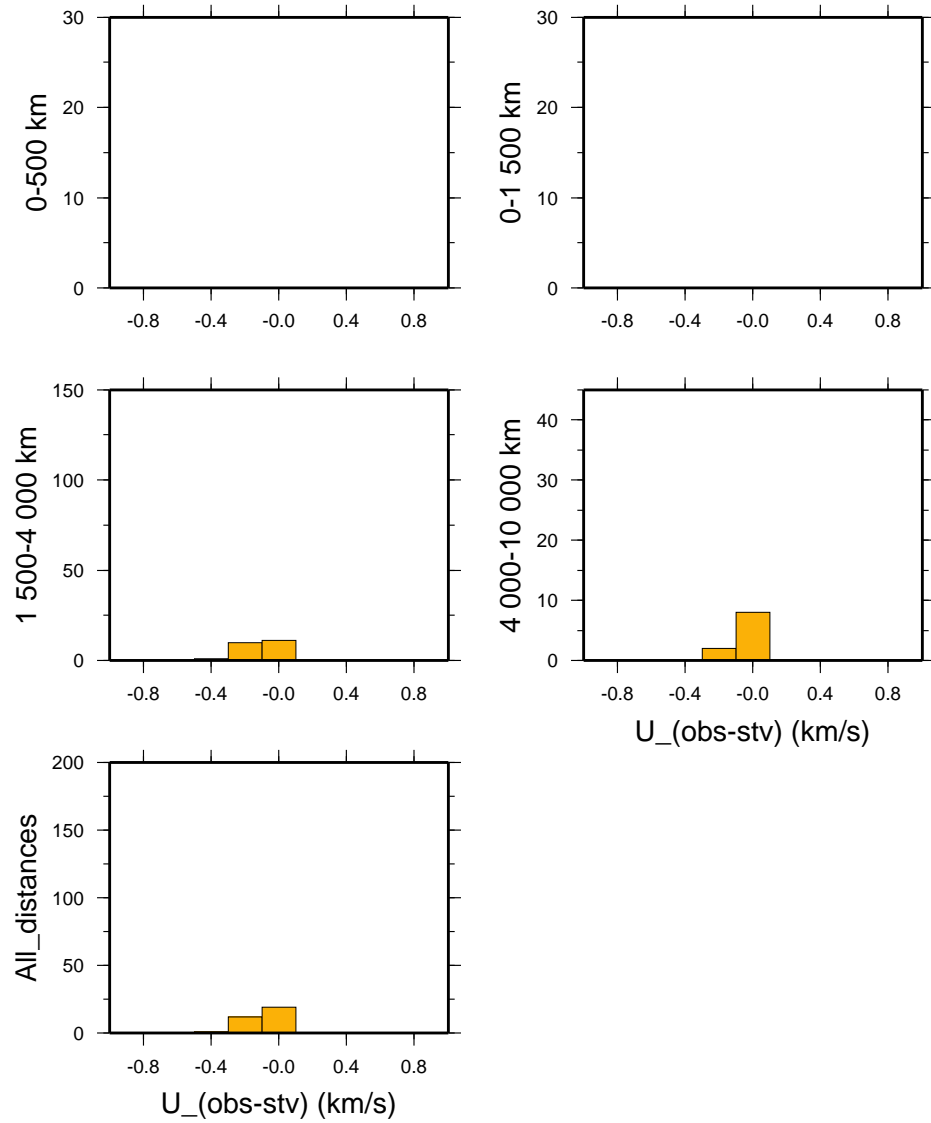
Figure 4.14: Histogram at 180 seconds, showing the number of measurement corresponding to each value of the differences between observation and Stevens' model at 180 seconds period

220 seconds

Figure 4.15: Histogram at 220 seconds, showing the number of measurement corresponding to each value of the differences between observation and Stevens' model at 220 seconds period
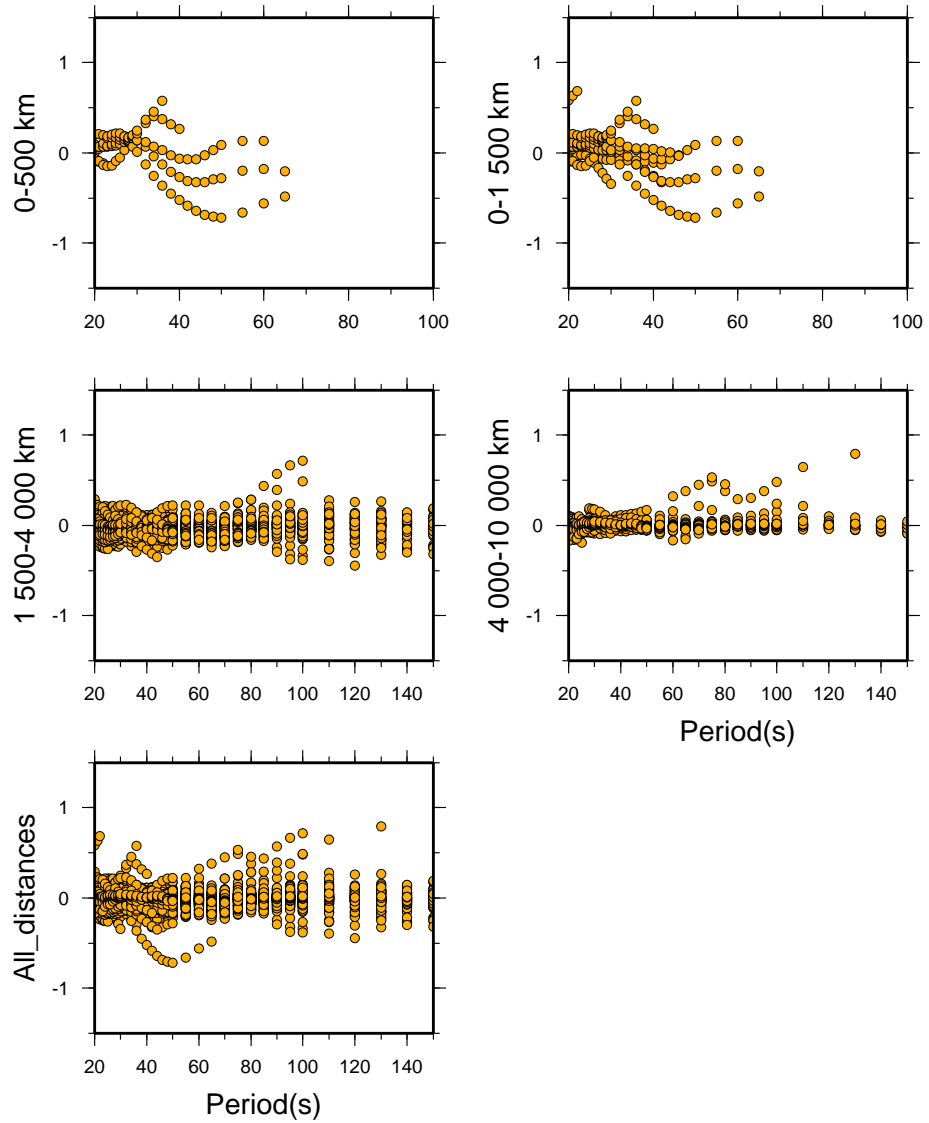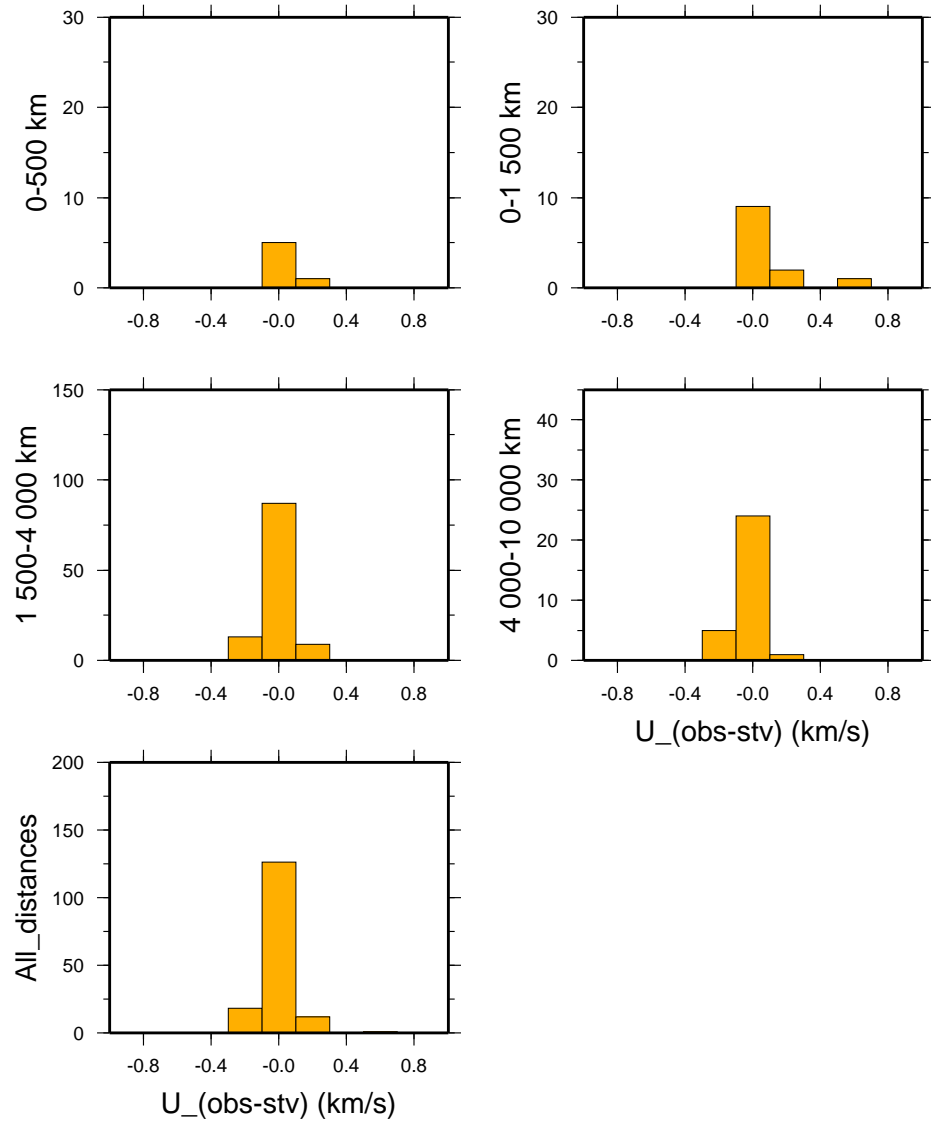
240 seconds
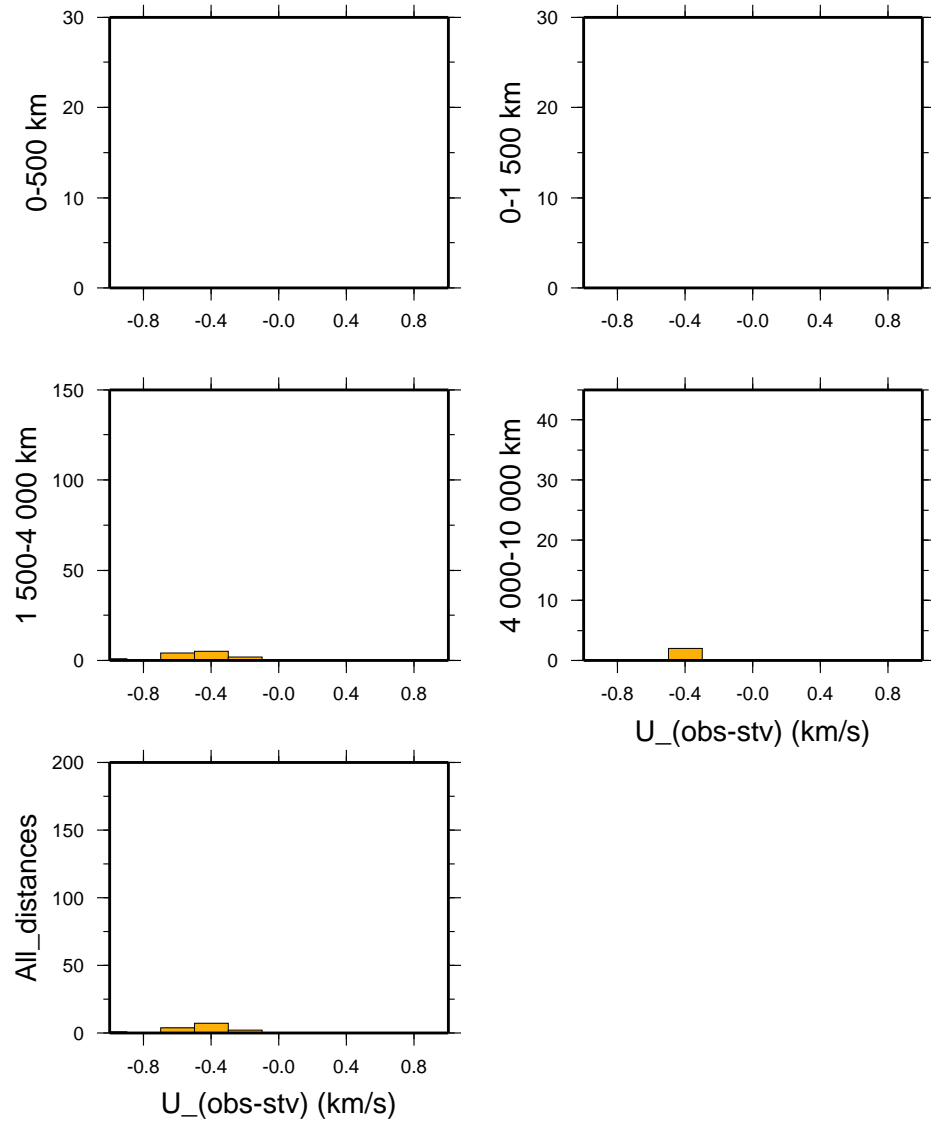
Figure 4.16: Histogram at 240 seconds, showing the number of measurement corresponding to each value of the differences between observation and Stevens' model at 240 seconds period
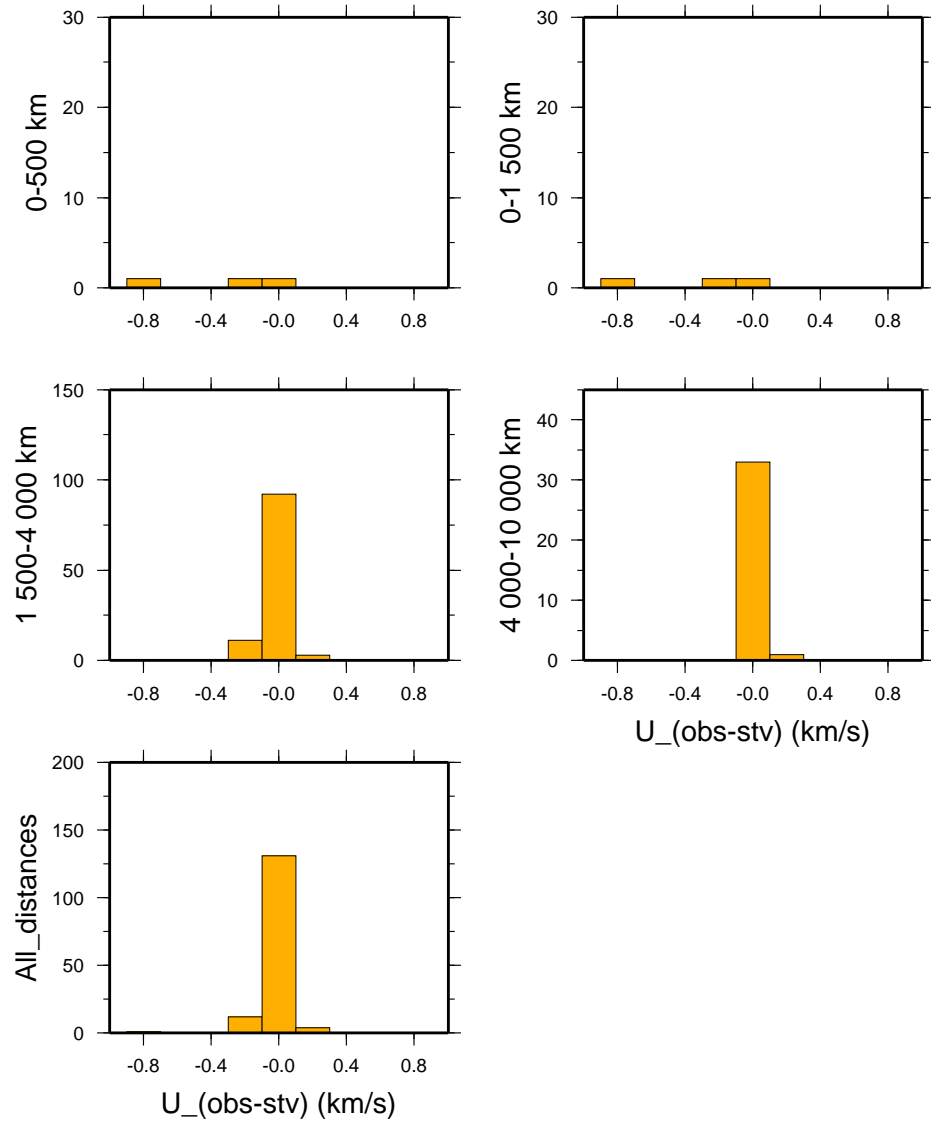
260 seconds
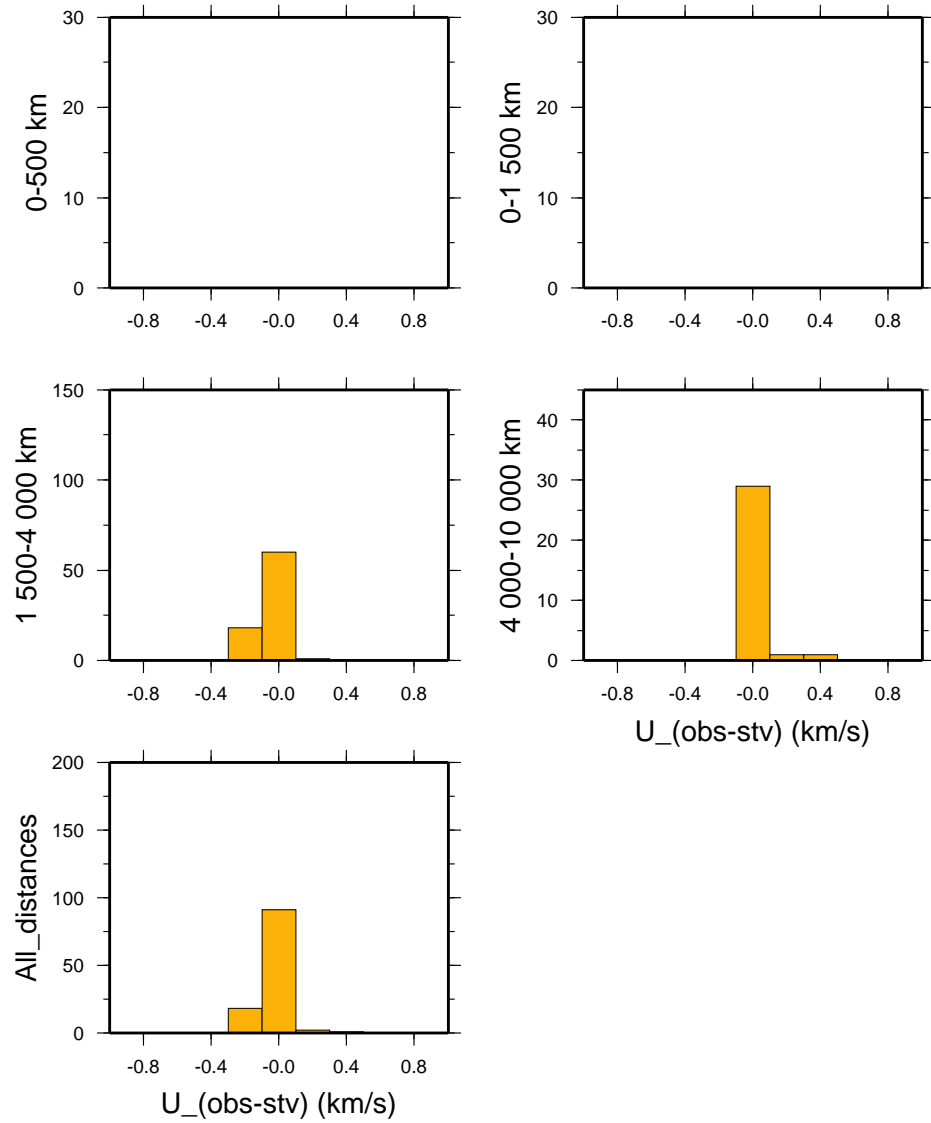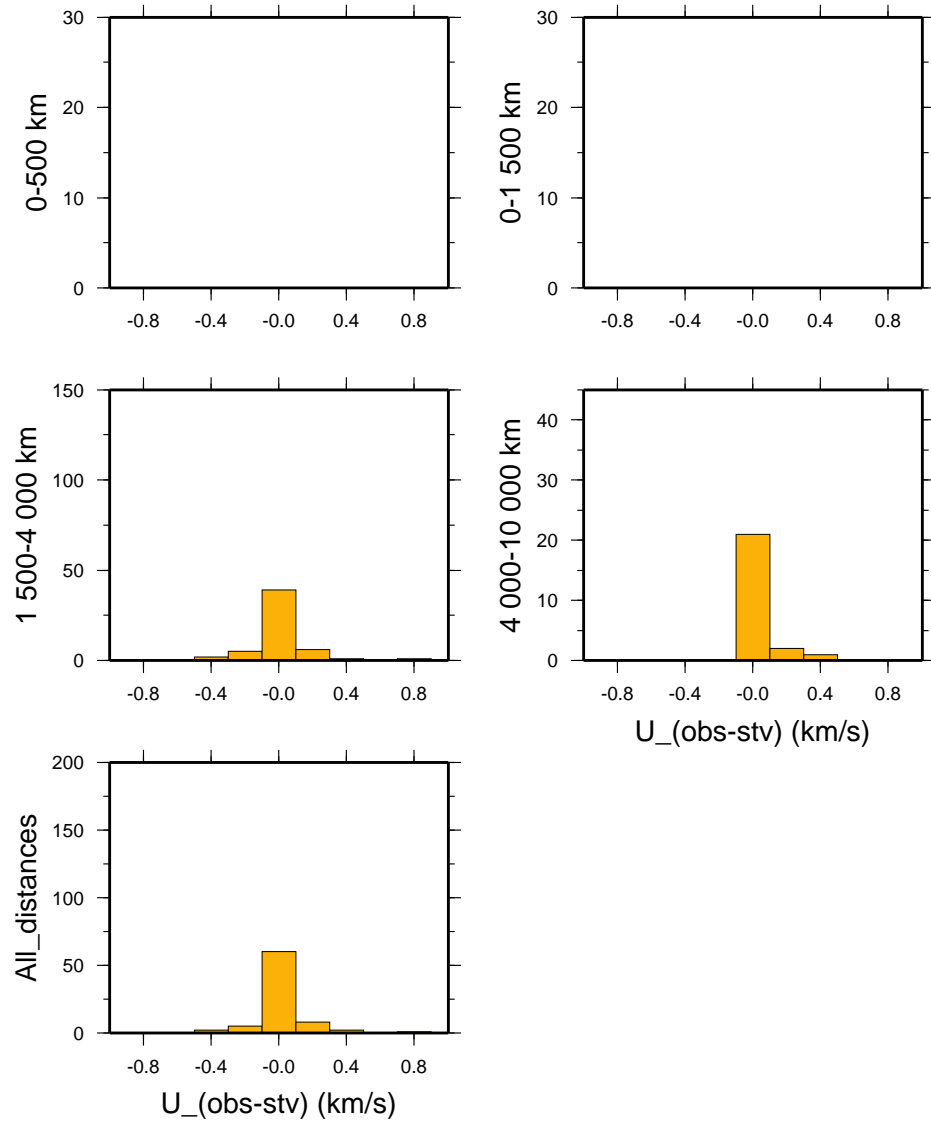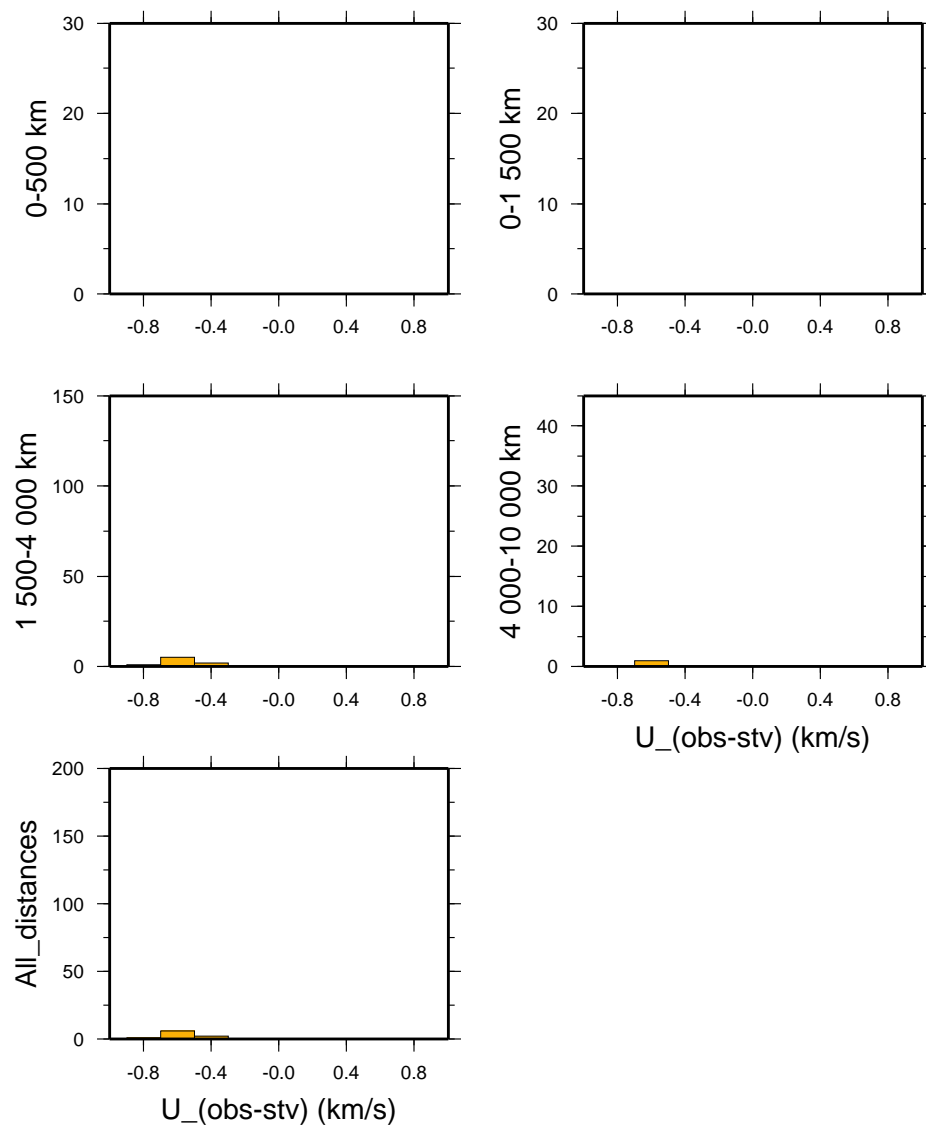

Figure 4.17: Histogram at 260 seconds, showing the number of measurement corresponding to each value of the differences between observation and Stevens' model at 260 seconds period
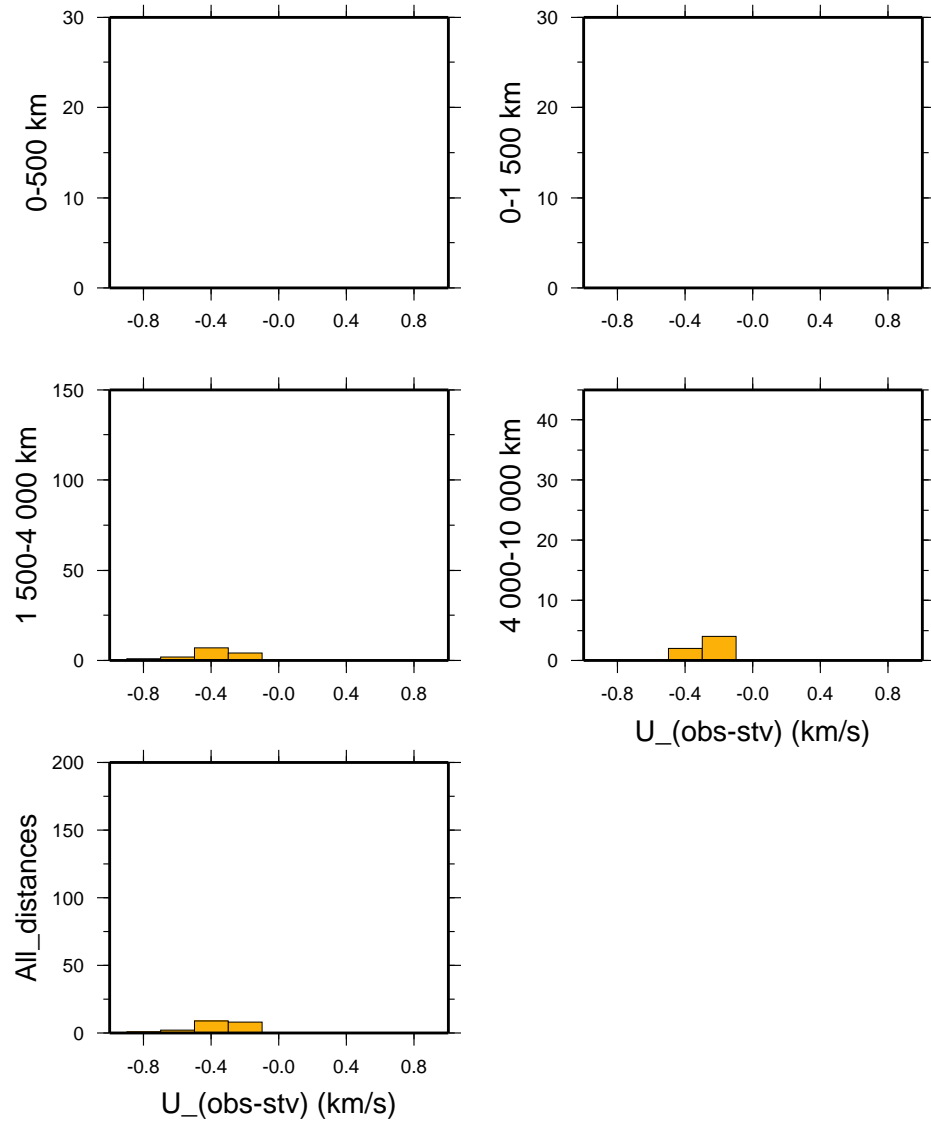
One way to present the common features of the comparison, is to show mean values of the difference between the observations and the Stevens' predictions with periods for different distance ranges (Figure 4.18). The number of observations per periods that contribute to these mean values are given in Figure 4.19. These two Figures are better to point out the main tendencies of the test results. Expansions of the Figure 4.7 are Figures 4.20 (periods shorter than 20 seconds), 4.21 (periods within 20 and 150 seconds), and 4.22 (periods longer than 150 seconds).

The performance of the Stevens model with period between 10 and 160 for distances longer than 1500 km is quite good, reproducing the observations very accurately ($\pm 3.3\%$ at 20 seconds, Figure 4.8). This result was expected, because that was the range of periods in which most of the data used by Stevens and Adams (2000). For periods less than 10 seconds the observed Rayleigh wave dispersion curves are faster than the model predictions. These underestimations are within $20 \pm 15\%$ at 5 seconds (Figure 4.5). Most of the observations for these shorter periods correspond to signal generated by presumed mining events in the deepest part of the Illinois Basin. The result confidence in these periods may be limited because of the difficulty in removing contributions coming from higher modes. The results for periods longer than 160 present a tendency of the model to have faster velocities than the observed group velocities. For example at 160 seconds the Stevens model overestimate the group velocities values by $12.5 \pm 2.5\%$ (Figure 4.12) This tendency increases with longer periods.
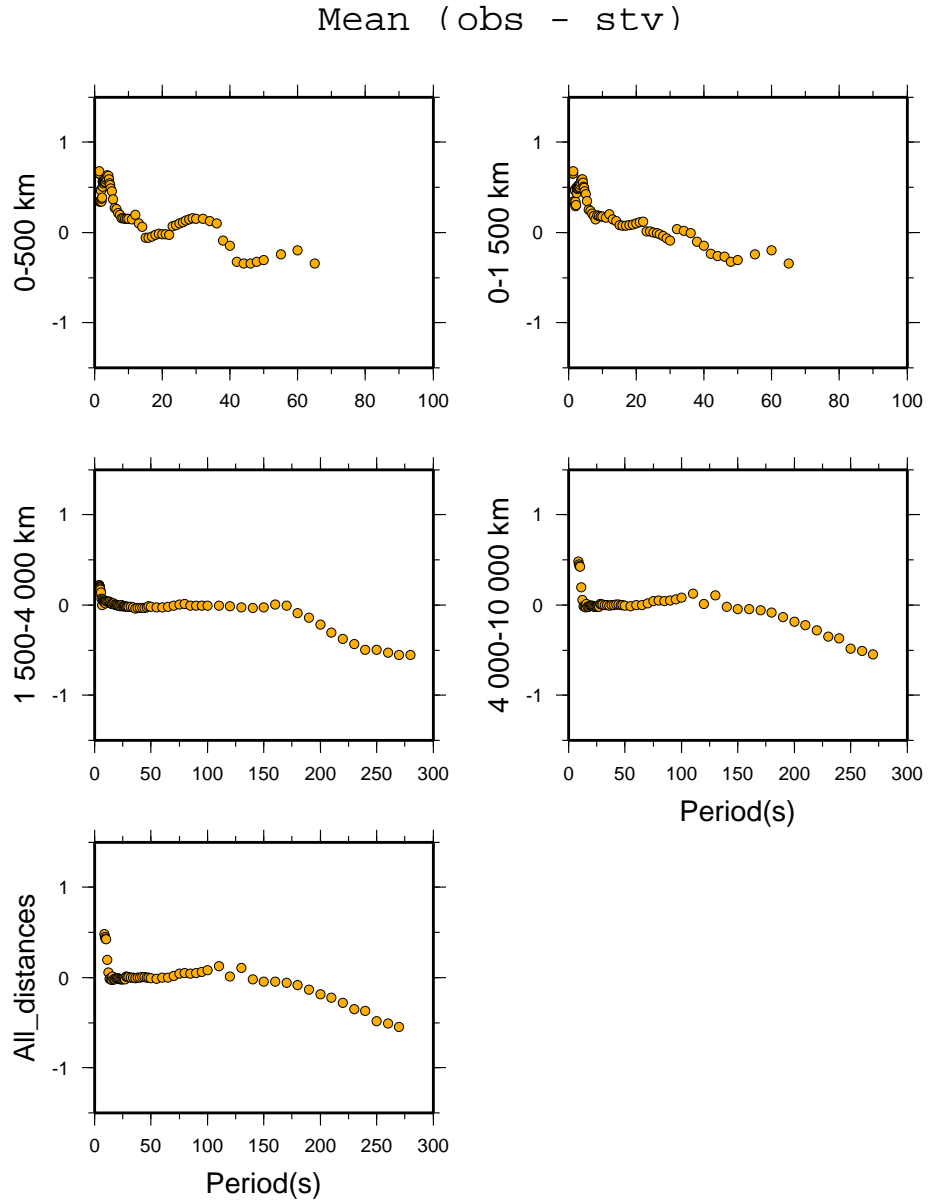
Figure 4.18: Mean values for the difference between observations and Stevens' model predictions for different range of distances as a function of period

Num Obs
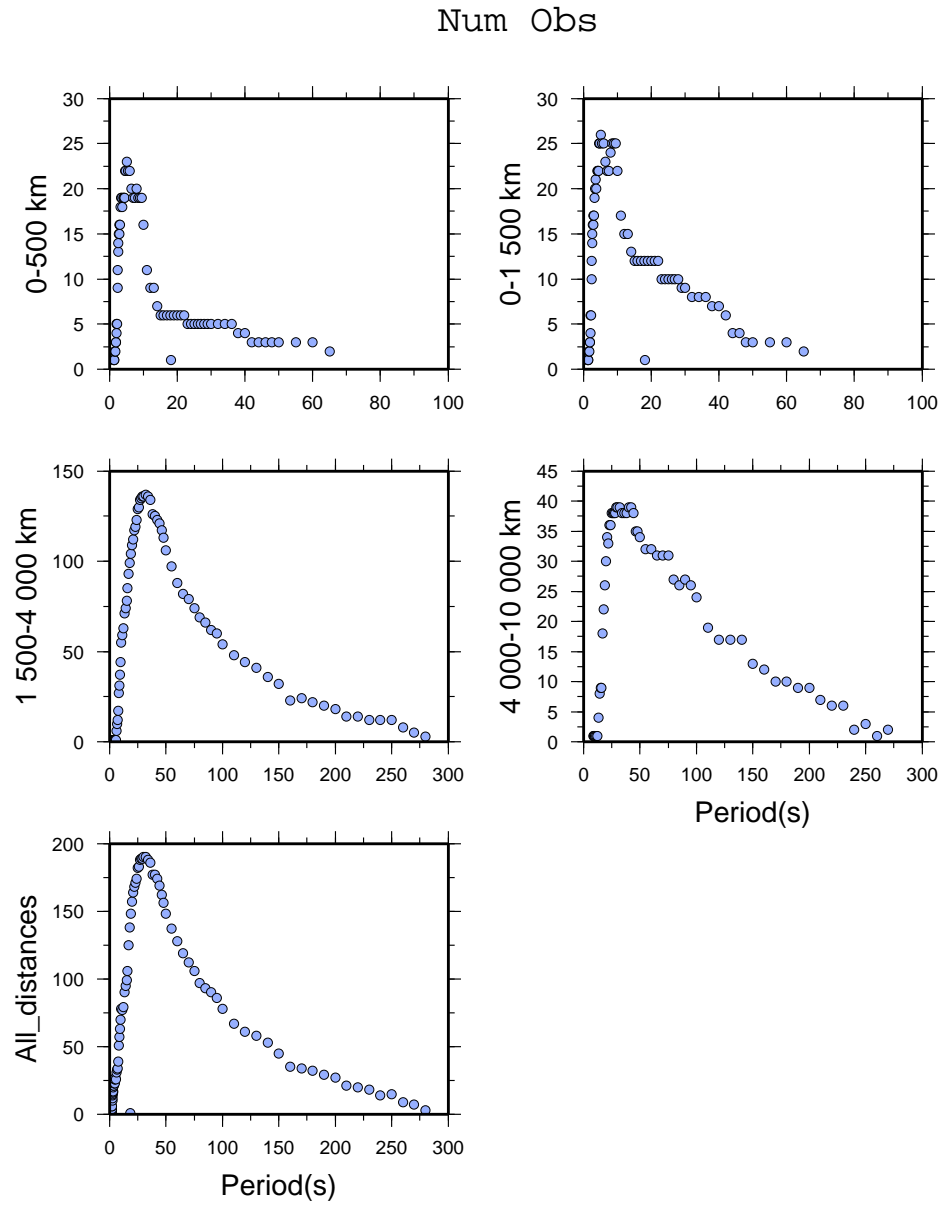
Figure 4.19: Number of observations per period that contribute to the mean values
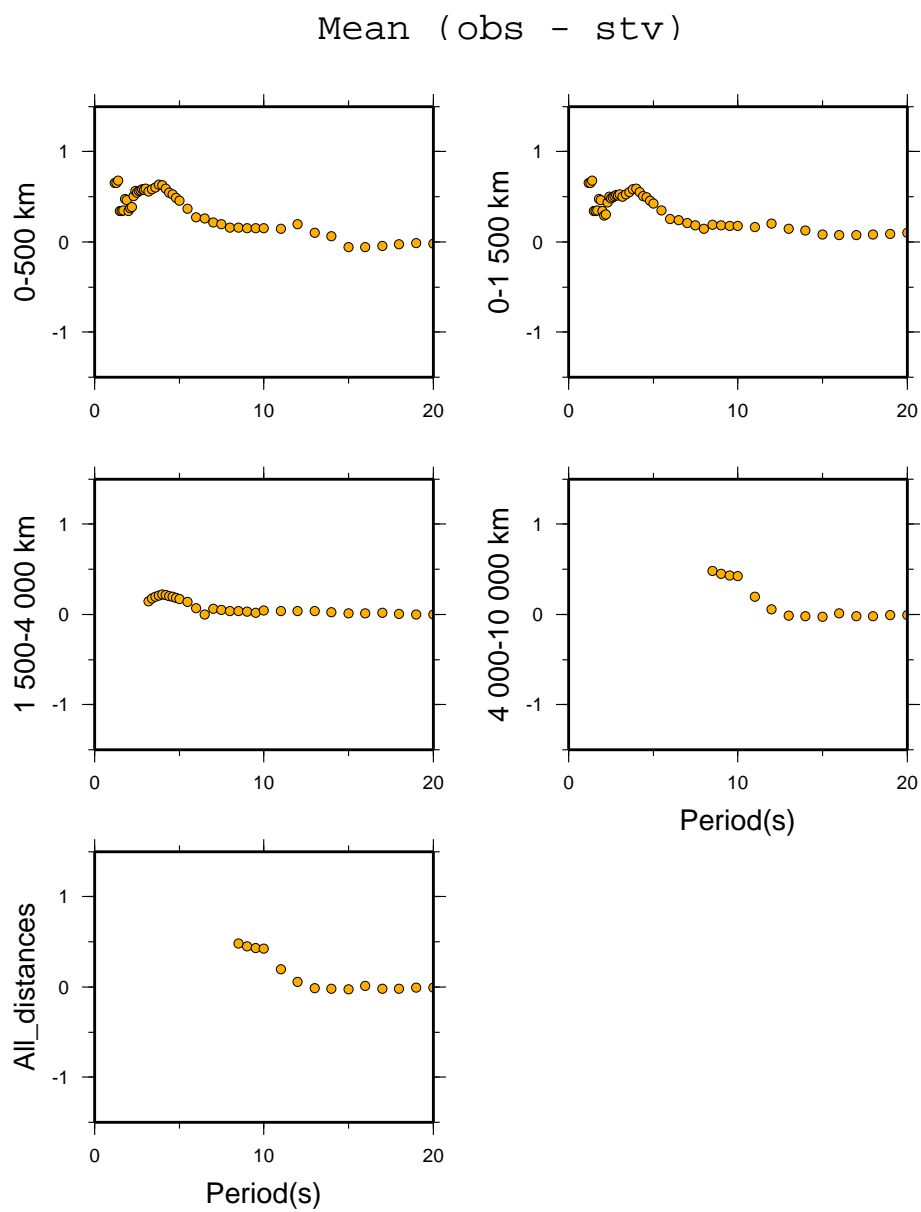
Figure 4.20: Expansion of Figure 4.7 for periods less than 20 s
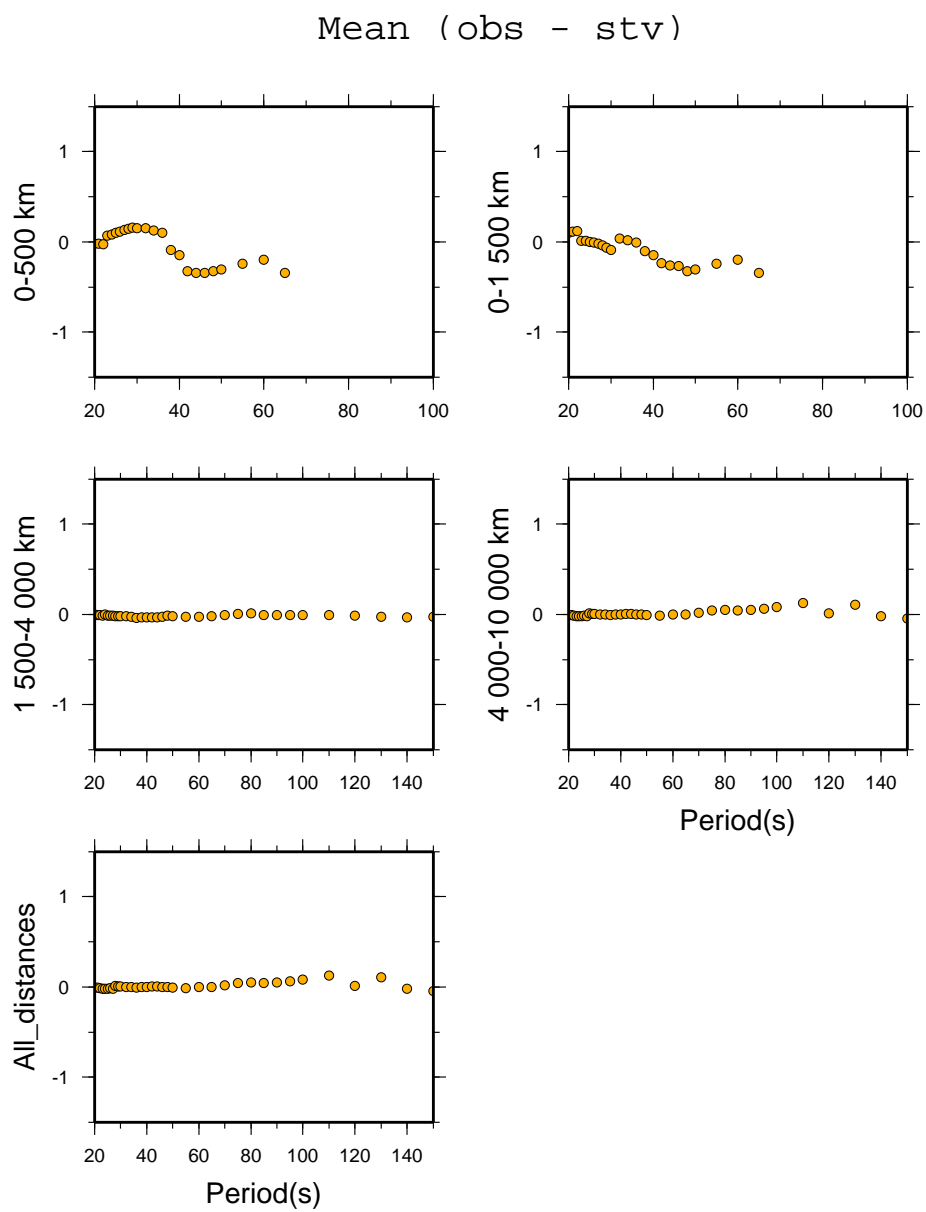
Figure 4.21: Expansion of Figure 4.7 for periods between 20 and 150 s
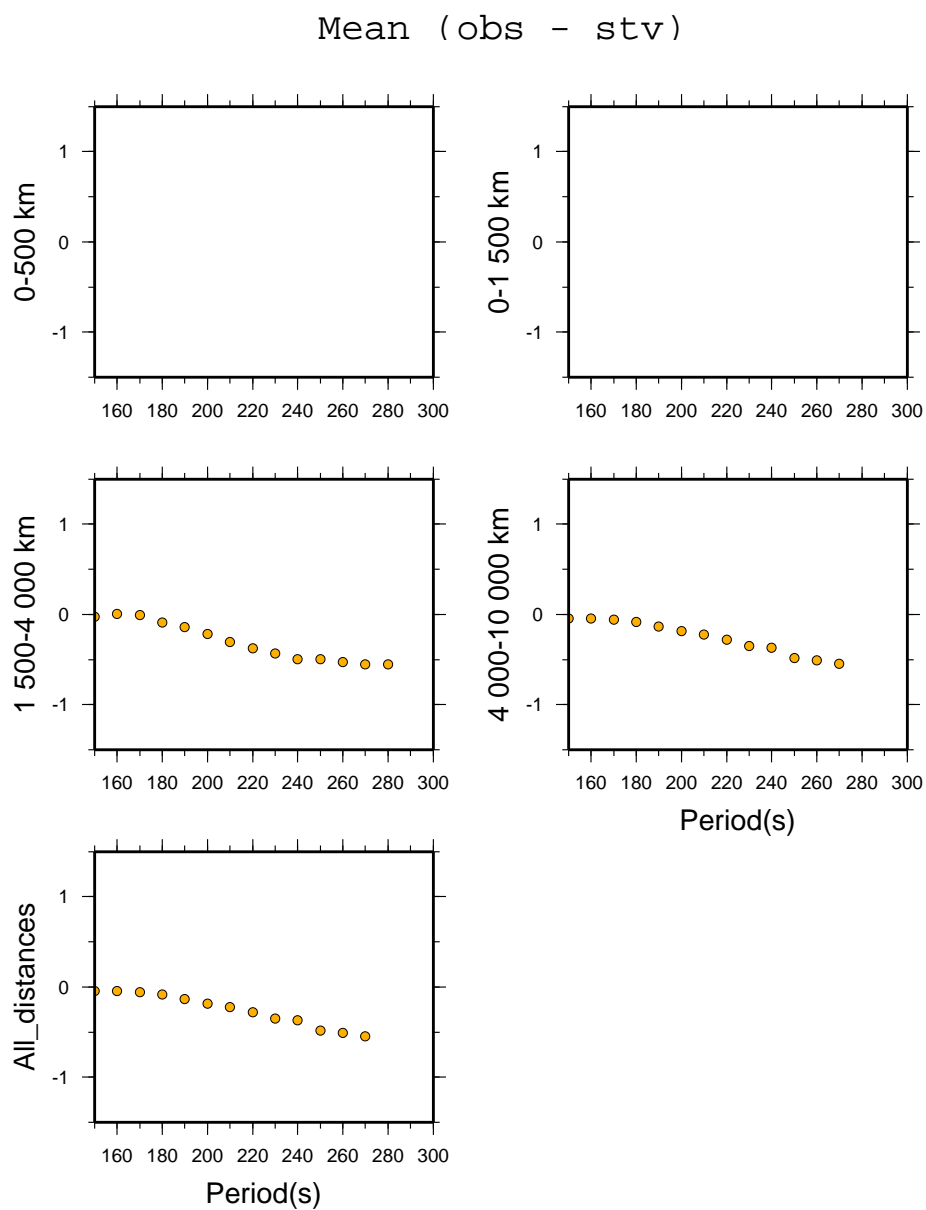
Figure 4.22: Expansion of Figure 4.7 for periods higher than 150 s

4.2.2 LOCAL EXPLOSIONS

Some of the events at local distances are presumed to be mining events, located near Evansville, IN (Figure 4.23 and Table 4.2, the events in group A). The observed Rayleigh wave group velocity dispersion curves for these explosion events are plotted in Figure 4.24. I organized the observations by station because the explosions are located very close one another, mapping almost the same path in their way to the stations. In the next Figure (4.25) the difference between the observations and the Stevens' model predictions are shown. These differences show a clear tendency for the predicted group velocities to be lower than observed. The periods of the explosion data ranges from 2 to 15 seconds. The comparison with the Stevens' model shows, as I already have commented, a tendency to underestimate the dispersion. However, I can see a repeated pattern in all of them: a linear increase of the observed group velocity with respect to the predicted from 2 seconds up to a maximum value at 4 seconds, followed by a linear decrease from 4 to 6 seconds and an almost constant difference thereafter.
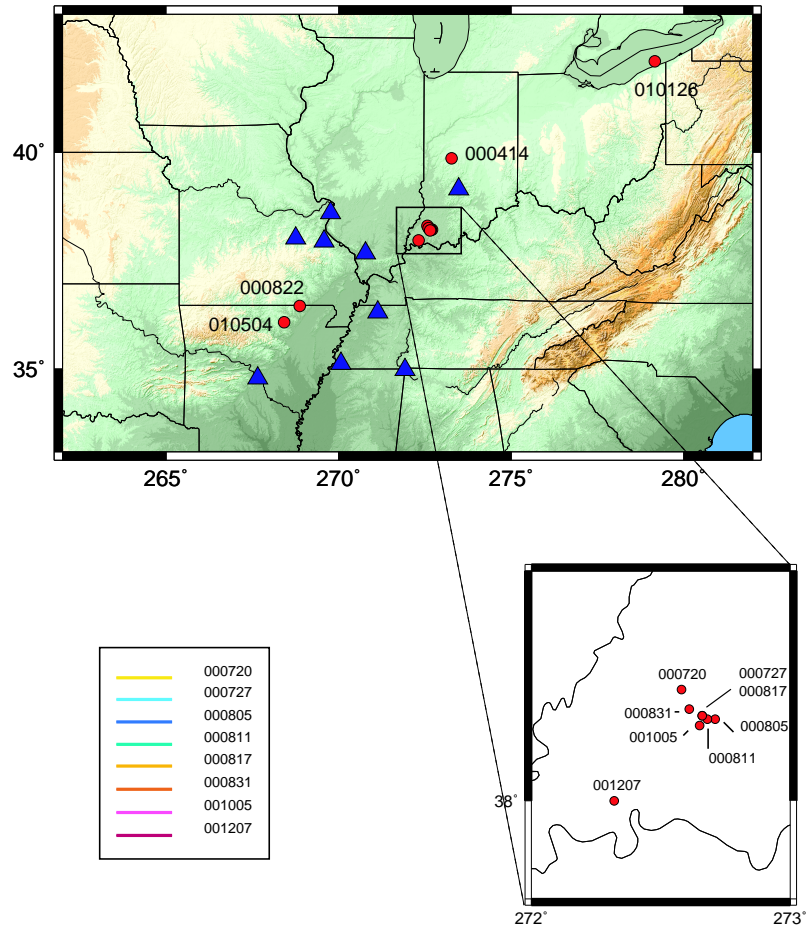
Figure 4.23: Map of local events. The small map shows the explosion events. In the bottom left corner the colors for each events in the following Figures are displayed
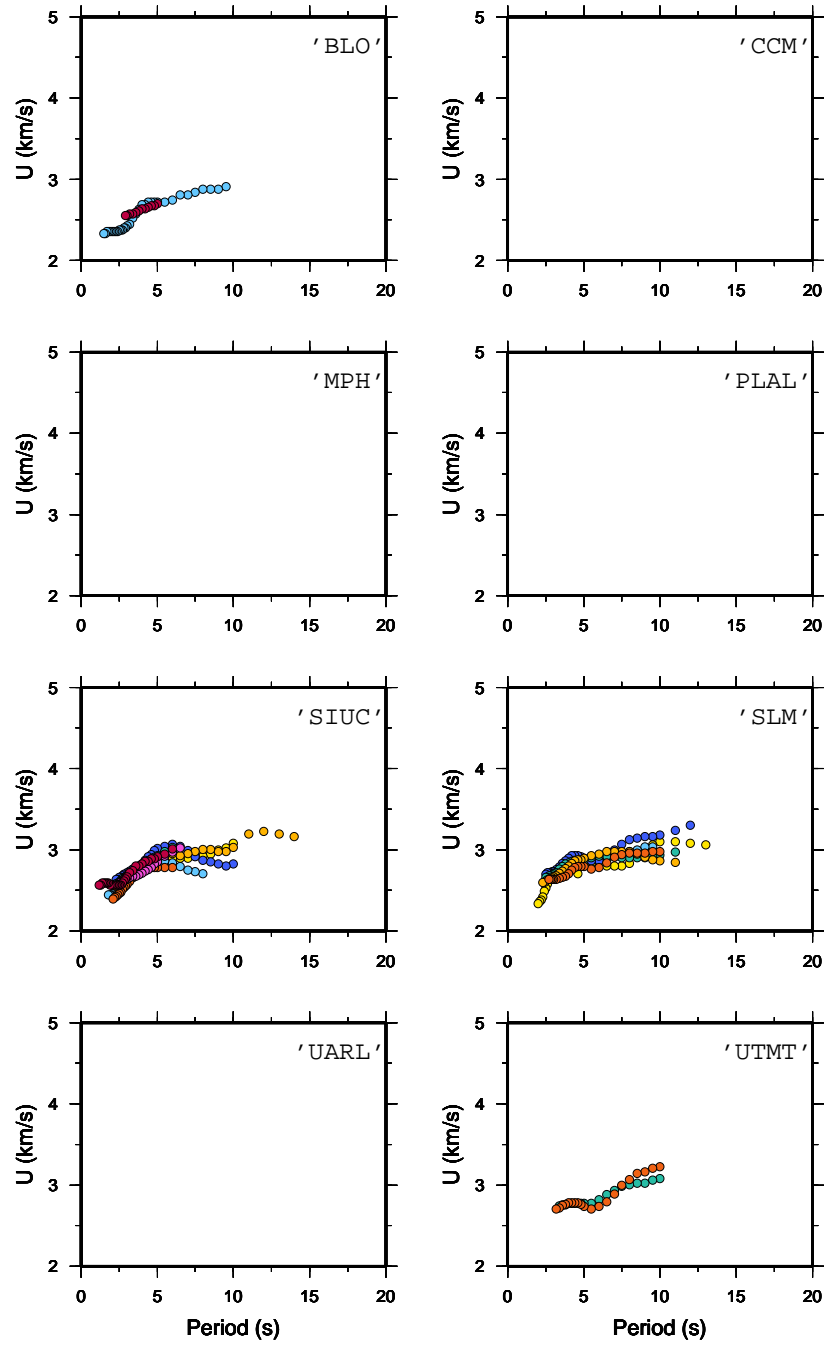
Figure 4.24: Group velocity dispersion curves for Rayleigh waves. Each color represents a different mining event. The color key is shown in Figure 4.12
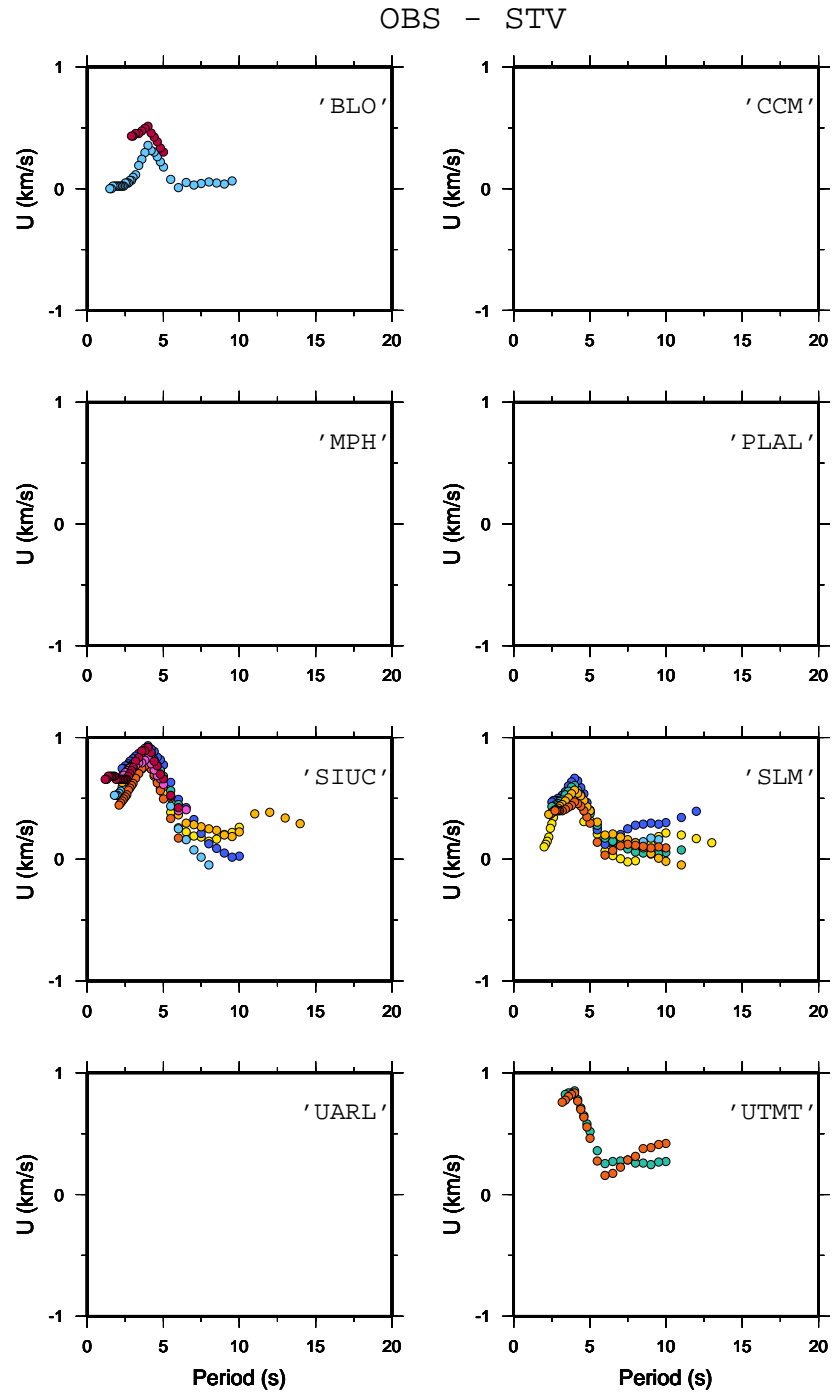
Figure 4.25: Difference between the observations and the Stevens' model predictions for Rayleigh group velocity dispersion curves for each station. Each color represents a different mining event. The color key is shown in Figure 4.12
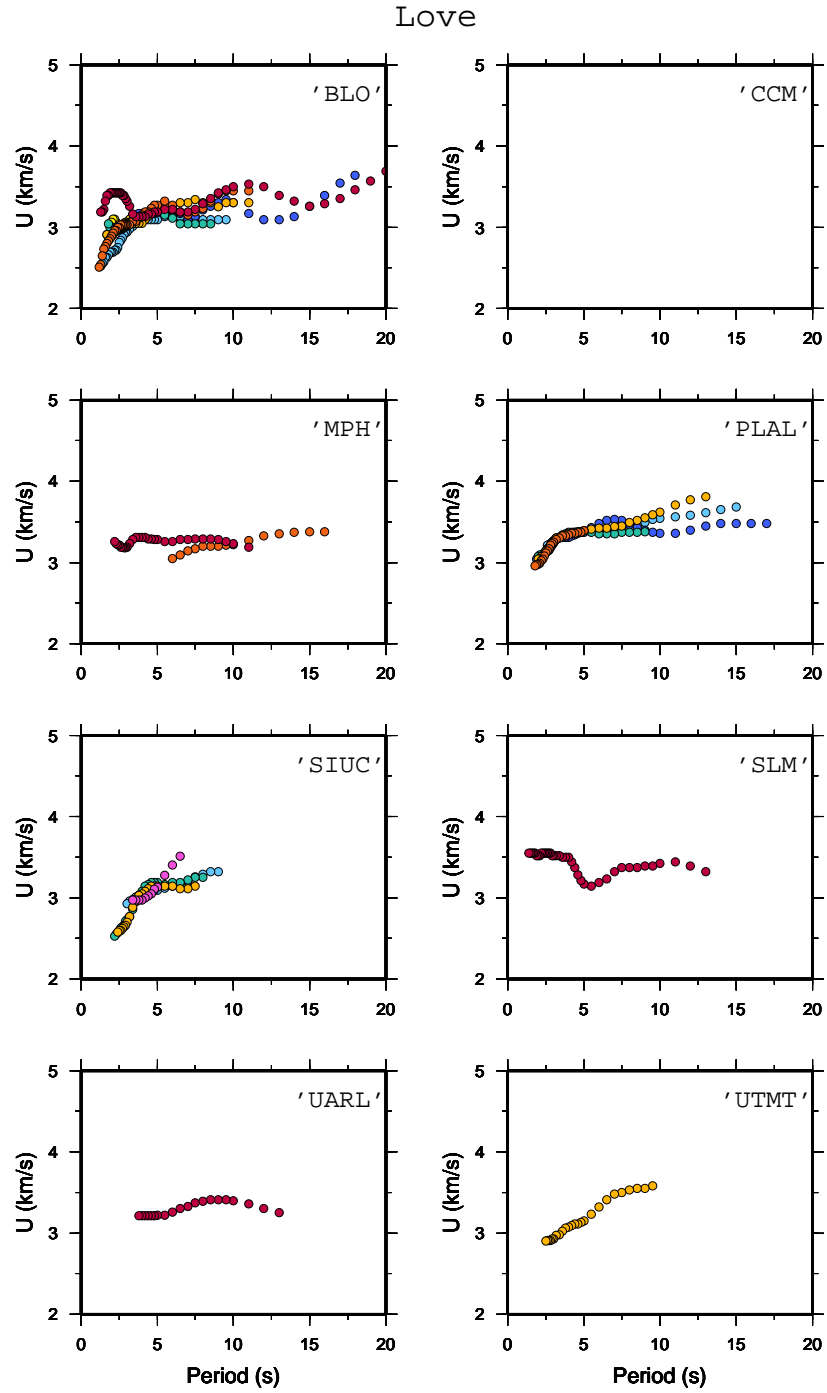
Figure 4.26: Group velocity dispersion curves for Love waves. Each color represents a different mining event. The color key is shown in Figure 4.12

4.3   ALABAMA EARTHQUAKE

The Alabama earthquake occurred in southern Alabama, on October 24 of 1997, with epicentral coordinates 31.2°N and -87.3°E. Chang et al. (1998) estimated the fault parameters (strike, dip, slip, depth, and seismic moment) using surface wave radiation pattern grid searches, regional waveform moment tensor inversion, and teleseismic P-waveform modeling. Their preferred fault parameters are strike $= 94°$, dip $= 62°$ and rake $= -90°$ with a Mw = 4.9 at 4.5 km depth.

This earthquake was recorded by 48 stations located in North America (Fig. 4.15 and Table 4.4). The good station coverage give the possibility to test the Stevens' model for paths through North America at different distances.

As I did before with the rest of events, I present the completed set of differences between the observations and the Stevens' model predictions (Fig. 4.17). To facilitate their analysis an expansion of Figure 4.17 for periods shorter than 20 seconds is displayed in Figure 4.18. To point out the common feature of the test I obtain the mean values of these differences (Fig. 4.19) and in Figure 4.20 the number of observations that contribute to the main value at each period are shown.

The results have similar characteristic to the other events, showing a good agreement between observations and predictions from 10 to 160 seconds at distances longer than 1500 km.
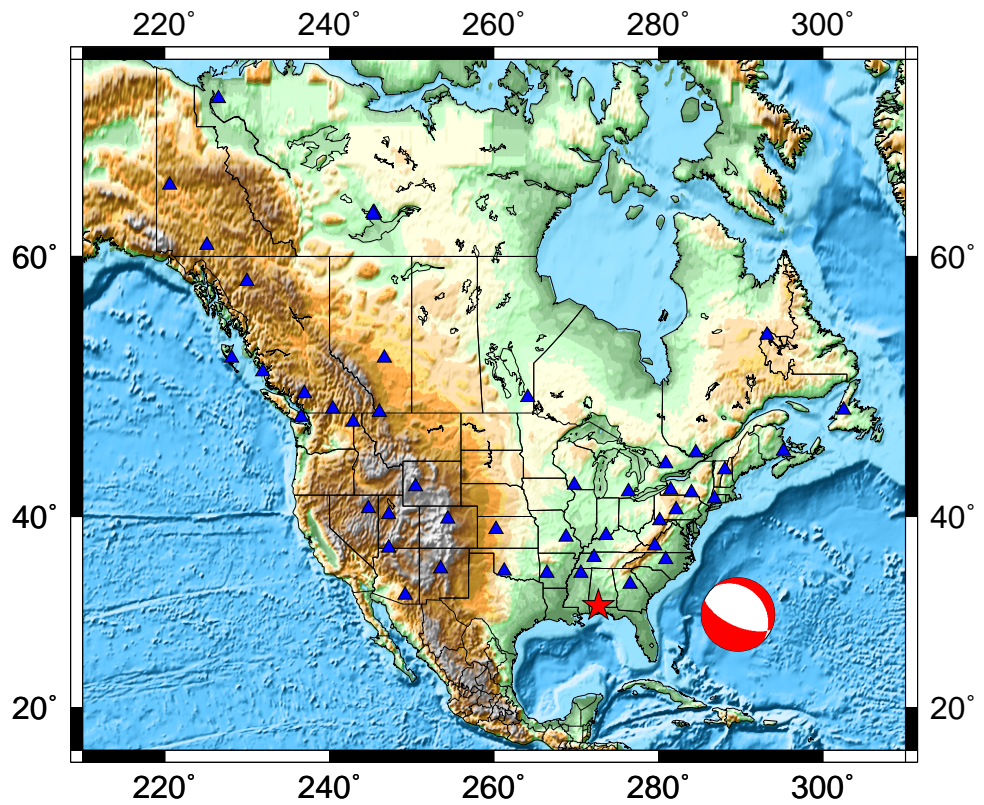
Figure 4.27: Map with the station (triangle) and the epicenter (start) locations for the Alabama earthquake. for the Alabama earthquake

Name	Lat	Lon	Name	Lat	Lon
BAAM	42.30	-83.66	MCWV	39.66	-79.85
ALQ	34.94	-106.46	MIAR	34.56	-93.57
BBB	52.18	-128.11	MOBC	53.20	-131.90
BINY	42.20	-75.99	NEW	48.26	-117.12
BLA	37.21	-80.42	OXF	34.51	-89.41
BW06	4.28	-109.56	PGC	48.65	-123.45
CBKS	38.81	-99.74	PMB	50.52	-123.08
CCM	38.06	-91.25	PNT	49.32	-119.62
CEH	35.89	-79.09	RES	74.69	-94.90
DAWY	64.06	-139.39	SADO	44.77	-79.14
DLBC	58.44	-130.03	SCHQ	54.83	-66.83
DRLN	49.26	-57.50	SSPA	40.64	-77.89
DUG	40.19	-112.81	TUC	32.31	-110.78
EDM	53.22	-113.35	ULM	50.25	-95.88
ELK	40.75	-115.25	WALA	49.06	-113.91
GAC	45.70	-75.48	WCI	38.21	-86.36
GOGA	33.41	-83.47	WHY	60.66	-134.88
INK	68.31	-133.52	WMOK	34.74	-98.78
ISCO	39.80	-105.61	WVT	36.13	-87.83
JFWS	42.91	-90.25	YKW1	62.49	-114.50
KNB	37.02	-112.82	YKW2	62.43	-114.61
LBNH	44.24	-71.93	YKW3	62.56	-114.62
LMN	45.85	-64.81	YKW4	62.49	-114.74
LSCT	41.68	-73.22	YSNY	42.48	-78.54

Table 4.4: Station locations for the Alabama earthquake
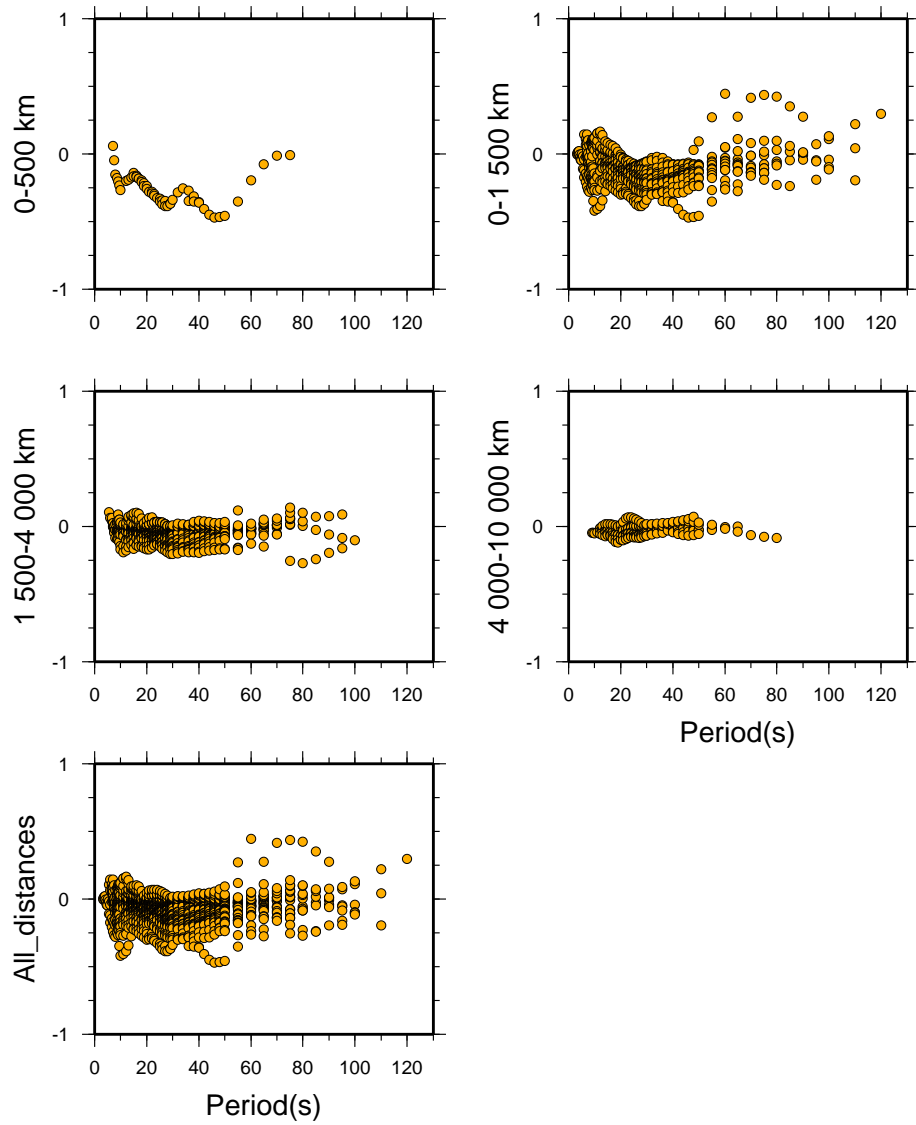
Figure 4.28: Differences between observation and Stevens' model predictions

ALABAMA (OBS - STV)
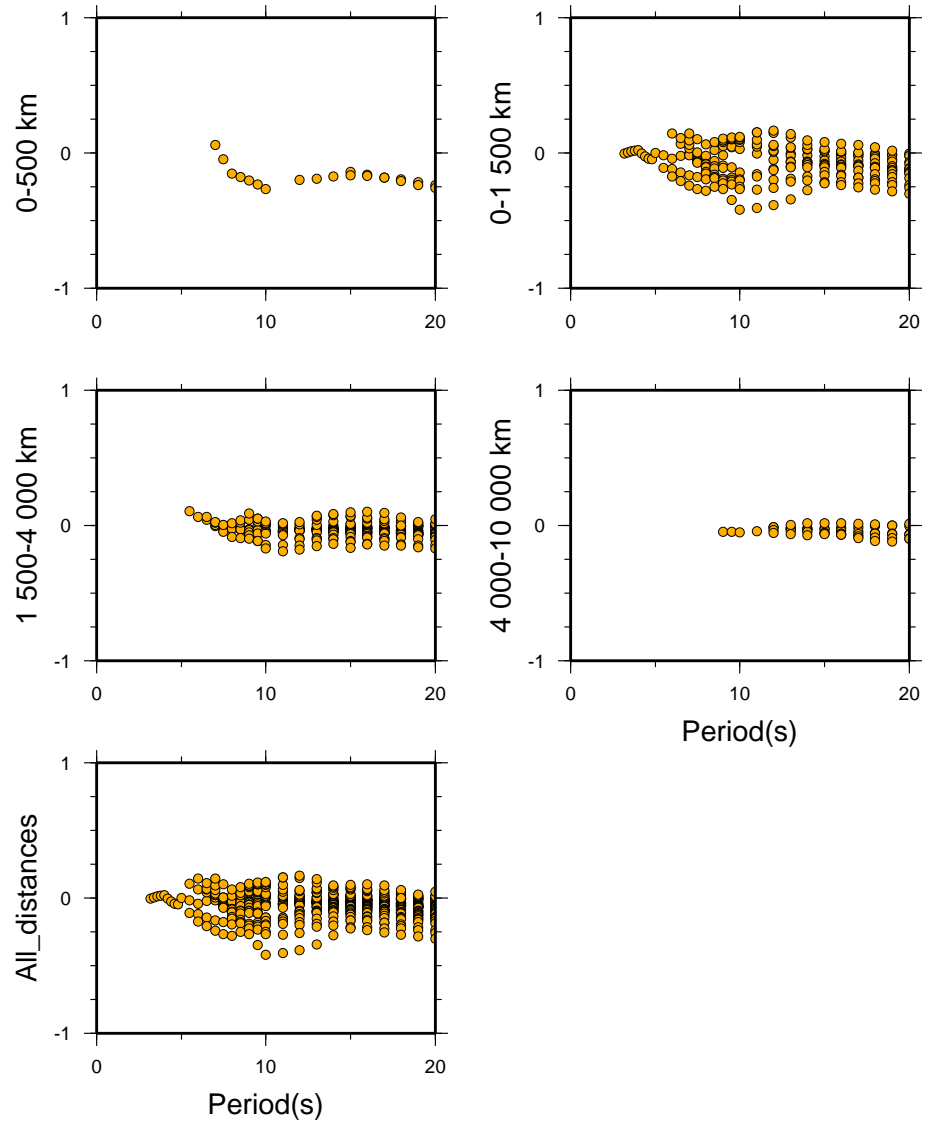
Figure 4.29: Expansion of Figure 4.17 for period < 20

ALABAMA Mean (obs-stv)
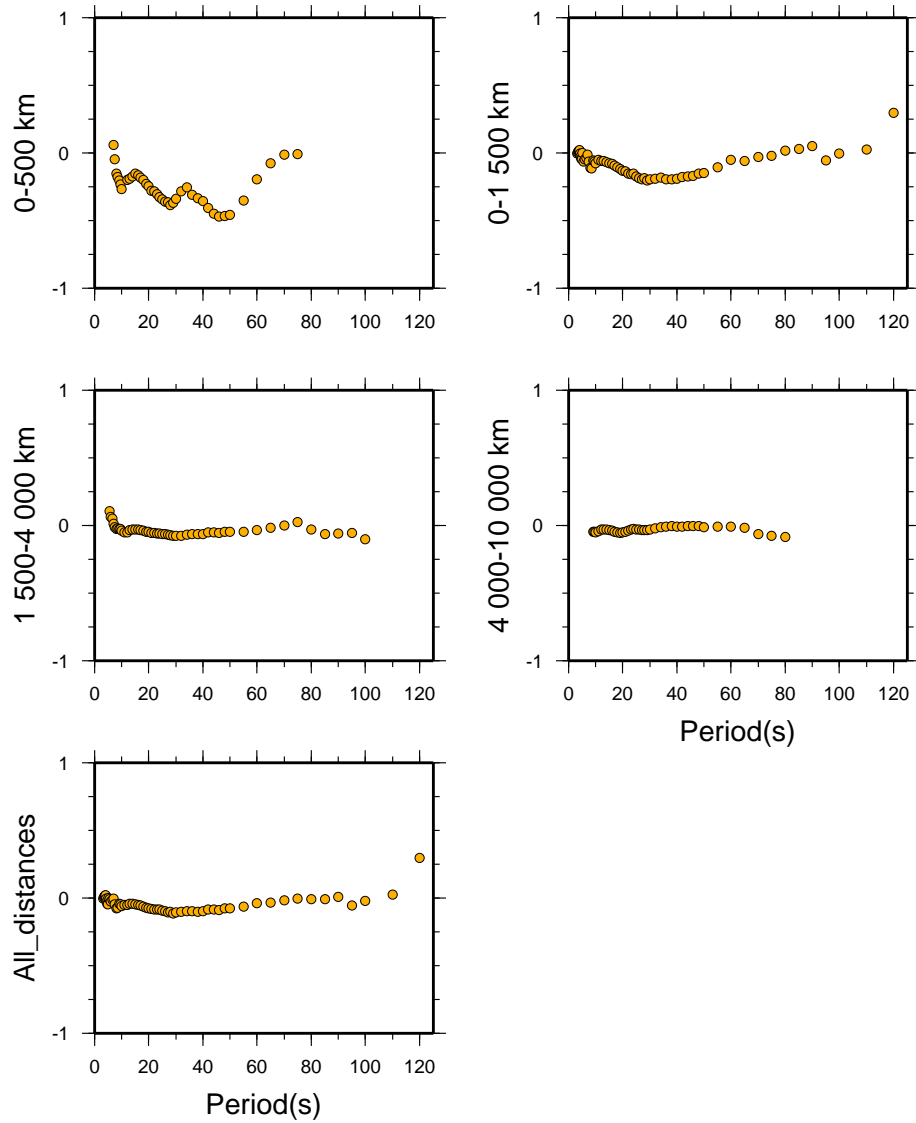
Figure 4.30: Mean between observation and Stevens' model
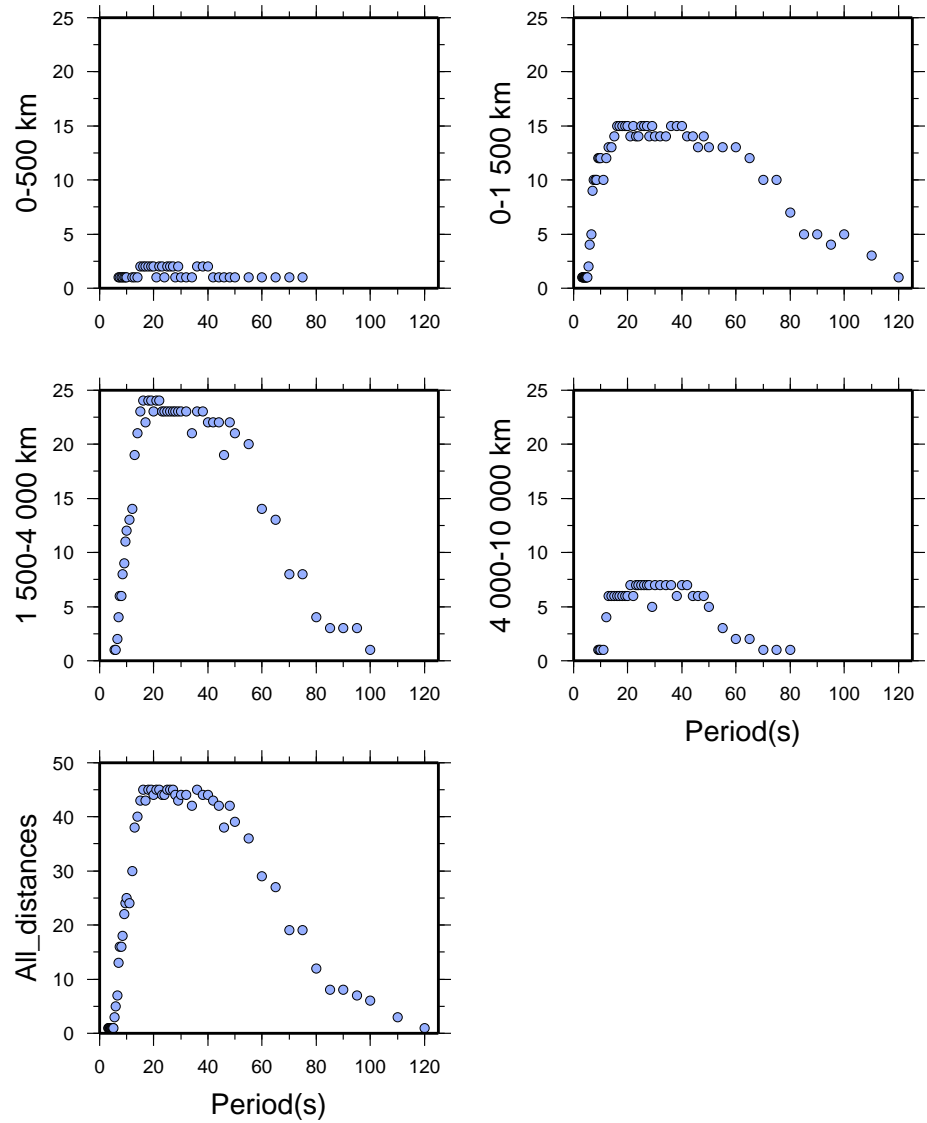
Figure 4.31: Number of observations that contribute to each period

5. THEORY OF THE PHASE VELOCITY MEASUREMENT

With the increase of the number of modern broadband stations in regional networks several methods have been developed in order to infer regional structure (e.g. Montagner, 1986; Friederich et al., 1994). The phase velocity of the surface waves has the advantage of being to first order a linear combination of the underlying 3-D model (Nataf el al., 1986). Friederich et al. (1994) discuss the limitations of the regional method for obtain regional structure.

After applying the phase matched filter, I obtained a signal containing a single mode, the fundamental mode. These simpler signals are the inputs for the $p-\omega$ technique that I use to calculate local phase velocity dispersion curve and which the theoretical bases are displayed in this chapter. The $p-\omega$ technique was first developed to be applied in linear array for refraction and reflection studies (McMechan and R. Ottolini, 1980). McMechan and Yedlin (1981) were the first to analyze of dispersive waves by this wave field transformation. Later Russell (1987) in his doctoral thesis developed this technique for discrete spatial sampling. I follow Russell (1987) for the phase velocity measurements.

In this chapter, I present the methodology used in the measurement of local phase velocity, the $p-\omega$ stacking. The results of the measurements are compared with the predictions of the regional HAMBURG model (Table 5.1) calculated from waveform modeling of an earthquake in Missouri (Herrmann and Ammon, 1997). The result are presented in the next chapter.

HAMBURG model					
Thickness (km)	P-velocity (km/s)	S-velocity (km/s)	Density (g/cm^3)	$Q_{\alpha^{-1}}$	$Q_{\beta^{-1}}$
1.00	4.93	2.85	2.48	0.0050	0.010
2.00	5.76	3.32	2.65	0.0005	0.001
2.00	6.25	3.60	2.77	0.0005	0.001
3.00	6.13	3.54	2.74	0.0005	0.001
3.00	6.23	3.60	2.77	0.0005	0.001
4.00	6.41	3.70	2.82	0.0005	0.001
4.00	6.36	3.67	2.80	0.0005	0.001
5.50	6.58	3.80	2.87	0.0005	0.001
5.50	6.53	3.77	2.85	0.0005	0.001
5.50	6.74	3.89	2.91	0.0005	0.001
5.50	6.63	3.83	2.88	0.0005	0.001
1.25	7.33	4.23	3.08	0.0005	0.001
1.25	7.36	4.25	3.09	0.0005	0.001
2.50	7.76	4.48	3.23	0.0005	0.001
2.50	7.84	4.52	3.25	0.0005	0.001
5.00	7.87	4.54	3.26	0.0005	0.001
2.50	8.06	4.65	3.33	0.0005	0.001
∞	8.56	4.94	3.51	0.0005	0.001

Table 5.1: Earth model for Central North America. HAMBURG earth model.

5.1 P-ω STACKING

McMechan and Yedlin, (1981), developed an alternate approach to sur-
face wave analysis that consists in the transformation of the entire data
wave field into the slowness-frequency $(p - \omega)$ domain where the disper-
sion curve can be directly picked. This method is based on the principle
that when two functions are in phase for a given frequency their sum will
reach the maximum and their difference will assume the minimum value.
The $p-\omega$ stacking involves searching for phase velocities that will produce
constructive interference of monochromatic waves at a given frequency.
A direct sum of many recording at a given frequency will not, in general,
constructively interfere, due to phase differences at different station. How-
ever if it is assumed that the seismic signal can be approximated by a sum
of wave planes, the difference in phase between any two stations, having
the same azimuth, will be equal to $k(\omega)\Delta r$, where Δr is the interstation
distance. I follow Russell (1987) for the determination of phase velocity
using the $p - \omega$ technique with discrete spatial sampling.

The expression for the wavenumber is

$$k(\omega) = \frac{\omega}{c(\omega)} = \omega p(\omega), \tag{5.1}$$

where $p = 1/c$ is the wave slowness. Therefore, either k, p, or c can be
treated as independent variables in the searching, and they can be varied
for the value (or values) where the phase adjusted sum of the recording
reaches a maximum.

After applying the phase matched filter, I get a signal containing a sin-
gle mode, the fundamental mode. I use this simpler signals to obtain local

phase velocity dispersion curves. We can express them by

$$f(t, r) = \int_{-\infty}^{\infty} A(r, \omega) \exp[i(\omega t + \phi(\omega, \theta) - k(\omega)r)]d\omega, \qquad (5.2)$$

where $\phi(\omega, \theta)$ is the source term, θ is the azimuth and r the distance from the source to the receiver.

The $p - \omega$ stacking process involves two linear transformations: a slant stack followed by a Fourier transform. A slant stack is a linear operation that transforms a wave field in the t-r domain into the wave field in the $p - \tau$ domain. Here p is the ray parameter (horizontal slowness), and τ is projection of t to zero offset along a line of slope p through the point (t,r) (McMechan and Ottolini, 1980).

Let N spatially separated stations lie along the same azimuth from the seismic source. I normalize the signal dividing the recorded seismograms by the signal belonging to the closed station to the source. With this normalization the source phase and the contribution of the Earth structure from the source to the closest station are removed. Then, the normalized signal has the expression

$$
\begin{aligned}
\bar{f}(t, r_i) &= \int_{-\infty}^{\infty} \frac{A(r,\omega)\exp[i(\phi(\omega,\theta)-k(\omega)r)]}{A(r_1,\omega)\exp[i(\phi(\omega,\theta)-k(\omega)r_1)]} \, exp[i\omega t]d\omega \\
&= \int_{-\infty}^{\infty} \frac{A(r,\omega)}{A(r_1,\omega)} \, \exp[i(\omega)t - k\Delta r_i]d\omega,
\end{aligned}
\qquad (5.3)
$$

where $\Delta r_i = r_i - r_1$ is the different between station i and the closest station.

After this normalization I perform the slant stack, transforming from $\bar{f}(r, t)$ wave field to $U(p', \tau)$, where

$$U(p', \tau) = \sum_{n=1}^{N} \bar{f}(r_n, \tau + p'\Delta r_n), \qquad (5.4)$$

N is the number of station. Substituting (5.3) into (5.4), we have

$$U(p', \tau) = \sum_{n} \int_{-\infty}^{\infty} \hat{A}_n(r_n, \omega) \exp[i(\omega\tau + \omega p'\Delta r_n - \omega p(\omega)\Delta r_n]d\omega, \qquad (5.5)$$

where

$$\hat{A}_n(r_n, \omega) = \frac{A(r, \omega)}{A(r_1, \omega)}. \tag{5.6}$$

The $p - \tau$ wave field contains the same information that the original data does, but it is now decomposed into elements of equal phase velocity c (1/p). The slant stack introduces a desired phase distortion of the data (Chapman, 1978), but no frequency shift. Thus, the amplitude spectrum of the trace at a given p is identical to that associated with the corresponding phase velocity in the original data.

The second step is to perform a Fourier transform, that is

$$U(p', \omega) = \sum_n \hat{A}_n(r_n, \omega). \exp[i(\omega(p' - p)\Delta r_n], \tag{5.7}$$

The quantity $U(p', \omega)$ will have a maximum when p'=p. Then I look for the values of p' that maximize the modulus of $U(p', \omega)$ at each frequency to find the phase velocity dispersion curve. If I correct the signal amplitude by geometrical spreading and attenuation, the maximum value of $U(p', \omega)$ must be equal to the number of stations. If this value is less than N, then I can attribute this to some deviations from the assumptions, that all the station lie along the same azimuth and our signal can be approximate by plane waves.

McMechan and R. Ottolini (1980) discuss the limitations of $p - \tau$ transform, concluding that the main limitations are:

1. The profiles are usually spatially aliased. In order to avoid spatial aliasing, the station must be placed at a distance from one another which is less than one-half of the wavelength of the highest frequency one wishes to resolve. For example if at 20 s the phase ve-

locity is around 3 km/s we need that the interstation distance to be less than 300 km.

2. Another limitation associated with the data is related to the coherency between sources when is used more than one source in the stacking process. This is no problem when the sources are shots but might be a problem if earthquake sources were used. Since slant stacking depends upon constructive interference to delineate the $p - \tau$ locus, it work well only when the apparent sources exhibit the same initial polarity. But I resolve this problem when I normalize by the closest station in that way the source dependence is removed.

6. PHASE VELOCITY MEASUREMENT

6.1 DATA

In this chapter I present the local phase velocity measurements obtain using $p - \omega$ stacking method. With the application of the PMF to the data set (section 3.2), I not only obtain an improvement of the group velocity dispersion curves but also isolate the fundamental mode. Using this simpler signal, in which the noise and the influence of higher modes is significantly reduced, I apply the $p - \omega$ stacking to the completed set of measurements for each earthquake. The methodology is applied only to earthquakes with three or more Rayleigh and/or Love surface waves observations (Table 4.2, columns 6 and 7). The data set is the same I used in the Chapter 4 (Fig. 4.2 and Table 4.2), but I do not get measurements for all of them.

As I did, in other sections of this thesis, the earthquakes are grouped depending of their epicentral locations (Fig. 4.2). All the observations are plotted with a reference model, HAMBURG obtained by Herrmann and Ammon (1997) for Central United States. The observations for the earthquakes, belonging to the same group, are presented in the same Figure. Each of the earthquakes has a different color and the symbols are circles in contrast with the symbol for the predictions values which are triangles. The color keys are displayed in the bottom of each figure. Following each plot I present a table with the azimuth.

Group B1

Figure 6.1: Rayleigh and Love local phase velocity curves for B1 group. The different colors correspond to different earthquakes. The key between colors and earthquakes are displayed in left bottom of the figure. The circles and the triangles indicate the observations and the HAMBURG model predictions, respectively. triangles

Azimuth (°)			
Station/event	990125	990331	990820a
BLO	346	354	356
CCM			
MPH	339	348	349
PLAL	341	351	
SIUC			350
SLM	341	349	350
UARL			344.6
UTMT			352

Table 6.1: Azimuths for the earthquakes in group B1.

Group B2

Figure 6.2: Rayleigh and Love phase velocity curves for B2 group. The different colors correspond to different earthquakes. The key between colors and earthquakes are displayed in left bottom of the figure. The circles and the triangles indicate the observations and the HAMBURG model predictions, respectively

Azimuth (°)				
Station/event	990615	990621	000809	010428
BLO	22	29	30	34
CCM	14	22		29
MPH	20	29	30	36
PLAL			34	39
SIUC	19	27	27	32
SLM	16	23	24	29
UARL			26	32
UTMT	21	29	30	35

Table 6.2: Azimuths for the earthquakes in group B2.

Group B3

Figure 6.3: Rayleigh and Love phase velocity curves for B3 group. The different colors correspond to different earthquakes. The key between colors and earthquakes are displayed in left bottom of the figure. The circles and the triangles indicate the observations and the HAMBURG model predictions, respectively

Azimuth (°)						
Station/event	990403b	990404	990606	990711	990930	010113
BLO	2	20	8	3	20	4
CCM					12	
MPH	355	18	2	356		358
PLAL	359	22			21	2
SIUC	357	17	3		16	359
SLM	355	14	1	356	13	358
UARL				350	12	352
UTMT			4		18	

Table 6.3: Azimuths for the earthquakes in group B3.

Group B4
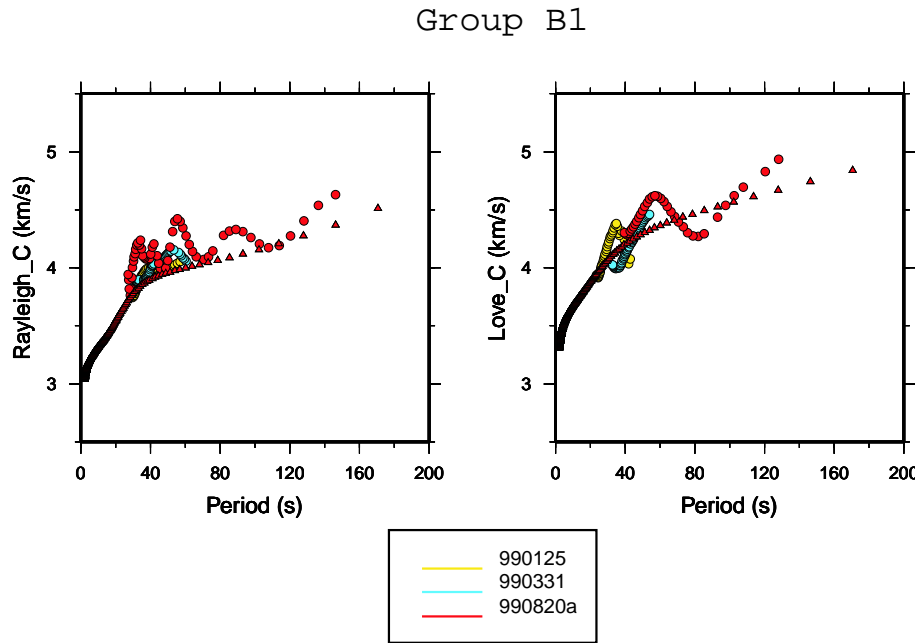

Figure 6.4: Rayleigh and Love phase velocity curves for B4 group. The different colors correspond to different earthquakes. The key between colors and earthquakes are displayed in left bottom of the figure. The circles and the triangles indicate the observations and the HAMBURG model predictions, respectively

Azimuth (°)					
Station/event	990515	990801	990818	991016	000903
BLO	76	76	76	70	
CCM					
MPH	87	88	86	81	87
PLAL				81	86
SIUC		81	80	74	81
SLM	78	78	78	71	79
UARL		90	88	82	89
UTMT	84	84	83	78	

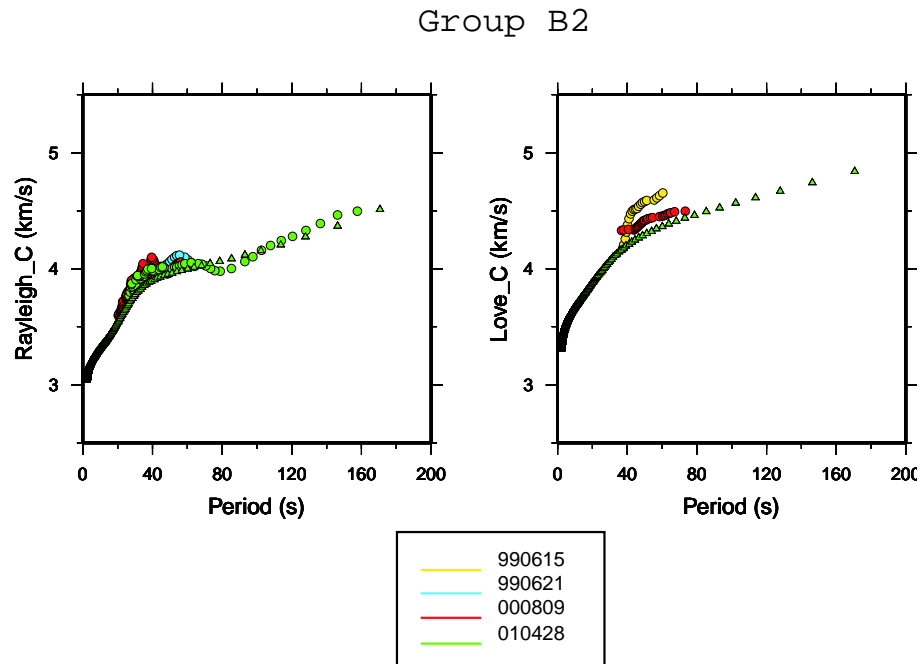Table 6.4: Azimuths for the earthquakes in group B4.

Group B5

Figure 6.5: Rayleigh and Love phase velocity curves for B5 group. The different colors correspond to different earthquakes. The key between colors and earthquakes are displayed in left bottom of the figure. The circles and the triangles indicate the observations and the HAMBURG model predictions, respectively

Azimuth (°)		
Station/event	990820b	010421
BLO	97	93
CCM		101
MPH	111	108
PLAL		106
SIUC		100
SLM	102	98
UARL	116	112
UTMT	107	

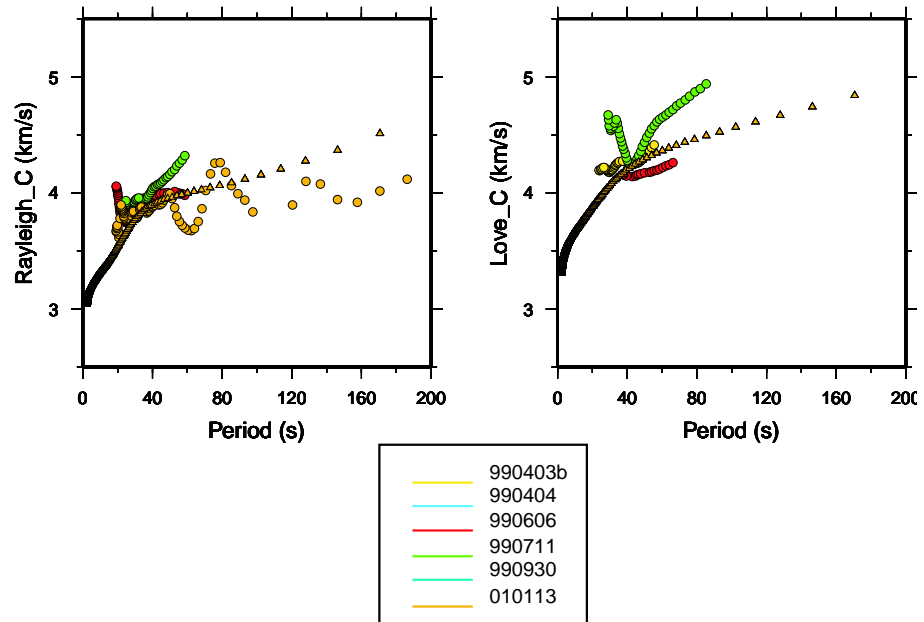Table 6.5: Azimuths for the earthquakes in group B5.

Group B6

Figure 6.6: Rayleigh and Love phase velocity curves for B6 group. The different colors correspond to different earthquakes. The key between colors and earthquakes are displayed in left bottom of the figure. The circles and the triangles indicate the observations and the HAMBURG model predictions, respectively

Azimuth (°)					
Station/event	990309	990703	000602	010111	010228
BLO	84	93	84	92	94
CCM		99			
MPH	93	103	93	102	104
PLAL	92		92		
SIUC	88	98	88		99
SLM	87	97	87	96	98
UARL		107	95	105	108
UTMT	91	100	90		

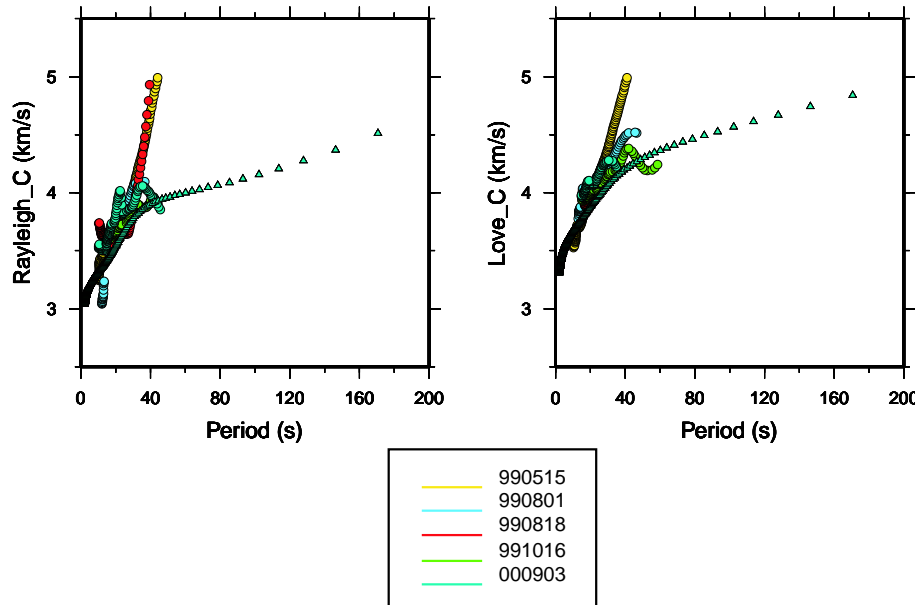Table 6.6: Azimuths for the earthquakes in group B6.

Group B

Figure 6.7: Rayleigh and Love phase velocity curves for B group. The different colors correspond to different earthquakes. The key between colors and earthquakes are displayed in left bottom of the figure. The circles and the triangles indicate the observations and the HAMBURG model predictions, respectively

Azimuth (°)		
Station/event	000101	000918
BLO	219	49
CCM		
MPH		55
PLAL	214	57
SIUC	224	49
SLM	230	46
UARL		53
UTMT		

Table 6.7: Azimuths for the earthquakes in group B.
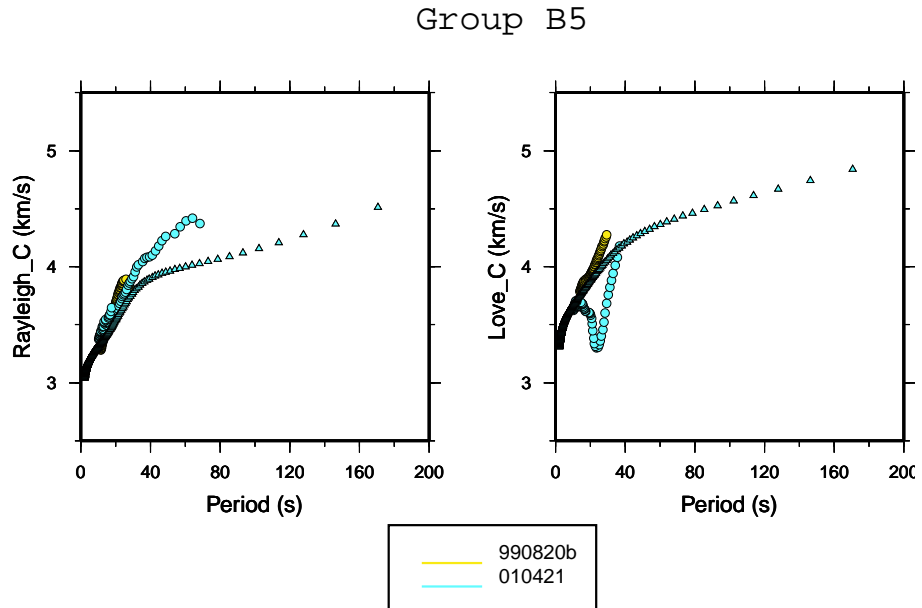
Group C1

Figure 6.8: Rayleigh and Love phase velocity curves for C1 group. The different colors correspond to different earthquakes. The key between colors and earthquakes are displayed in left bottom of the figure. The circles and the triangles indicate the observations and the HAMBURG model predictions, respectively

Azimuth (°)		
Station/event	990507	000711
BLO		83
CCM		
MPH		89
PLAL	88	88
SIUC	86	86
SLM	86	86
UARL		91
UTMT	87	87

Table 6.8: Azimuths for the earthquakes in group C1.
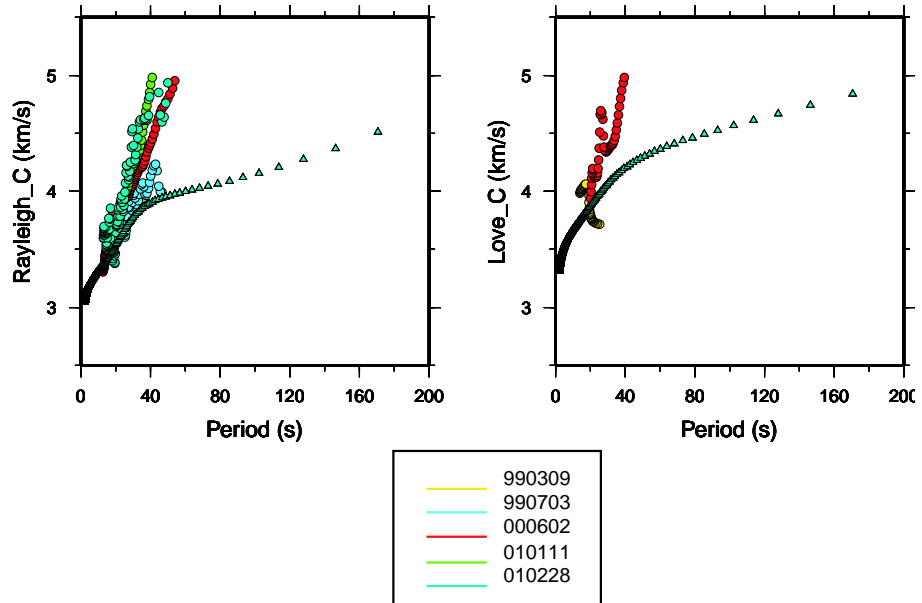
Group C2

Figure 6.9: Rayleigh and Love phase velocity curves for C2 group. The different colors correspond to different earthquakes. The key between colors and earthquakes are displayed in left bottom of the figure. The circles and the triangles indicate the observations and the HAMBURG model predictions, respectively

Azimuth (°)		
Station/event	990817	991112
BLO	315	316
CCM		318
MPH	315	
PLAL		314
SIUC		317
SLM	317	318
UARL	316	317
UTMT	315	316

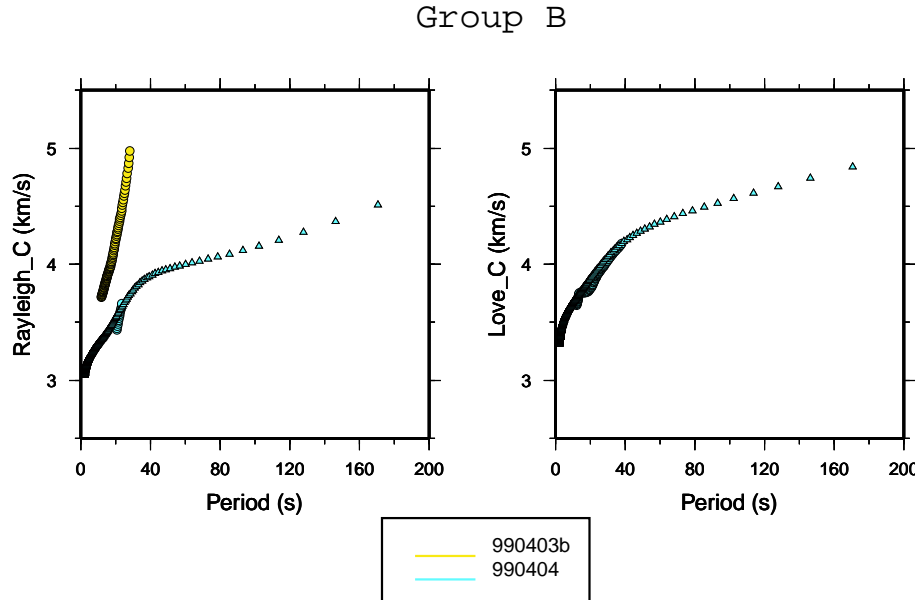Table 6.9: Azimuths for the earthquakes in group C2.
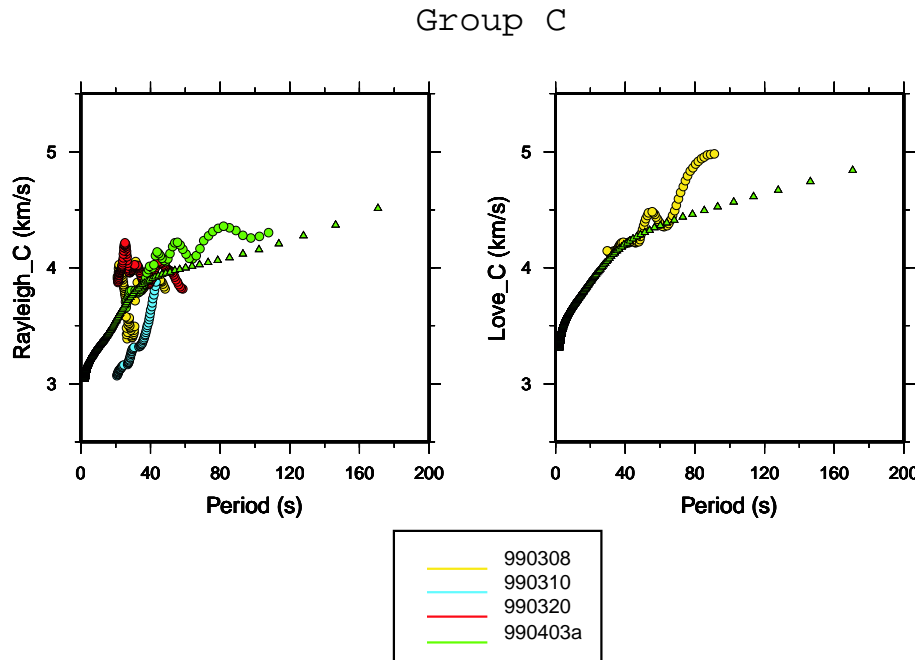
Group C

Figure 6.10: Rayleigh and Love phase velocity curves for C group. The different colors correspond to different earthquakes. The key between colors and earthquakes are displayed in left bottom of the figure. The circles and the triangles indicate the observations and the HAMBURG model predictions, respectively

Azimuth (°)				
Station/event	990308	990310	990320	990403a
BLO	48		63	347
CCM			66	
MPH	53		68	342
PLAL	52	269		344
SIUC	51	273		344
SLM	51	275	65	344
UARL				
UTMT		271		

Table 6.10: Azimuths for the earthquakes in group C.
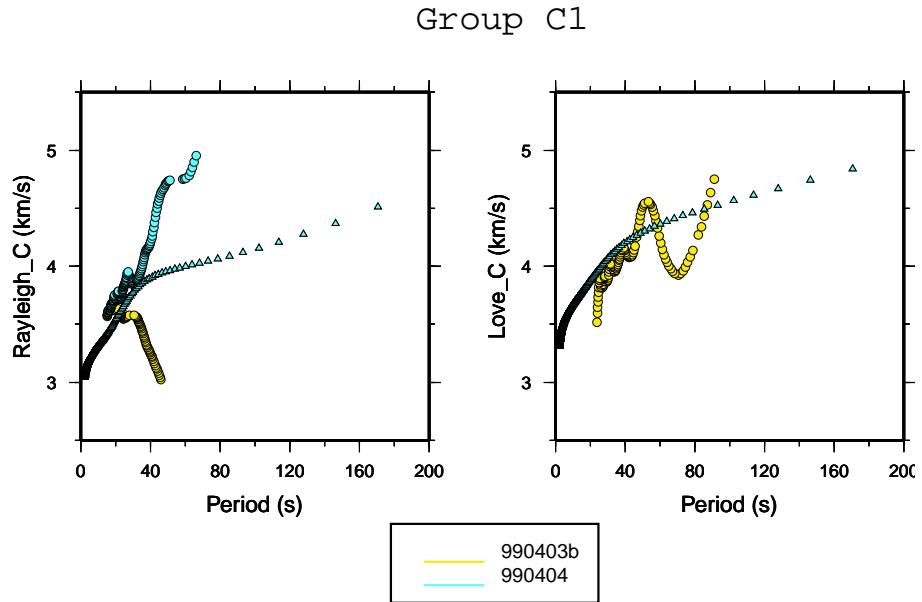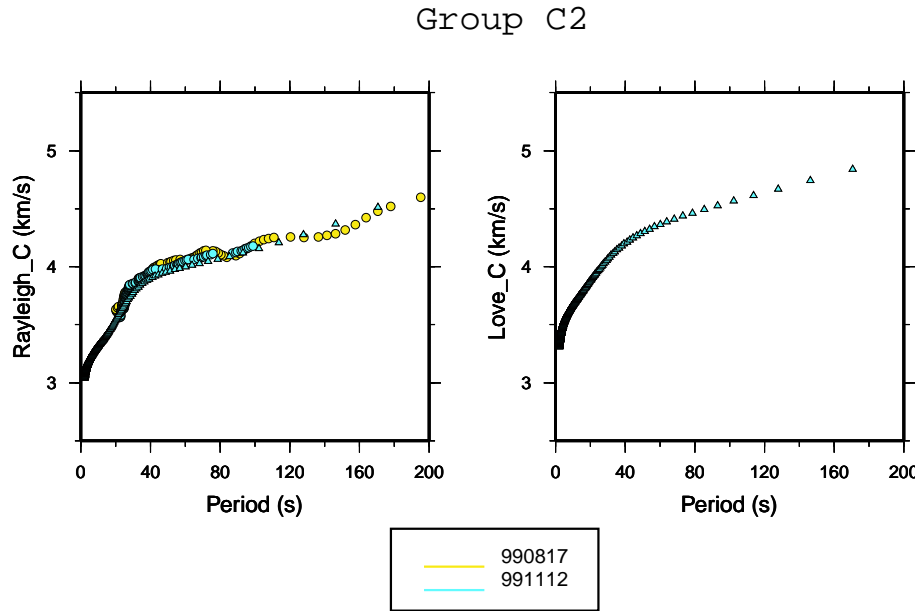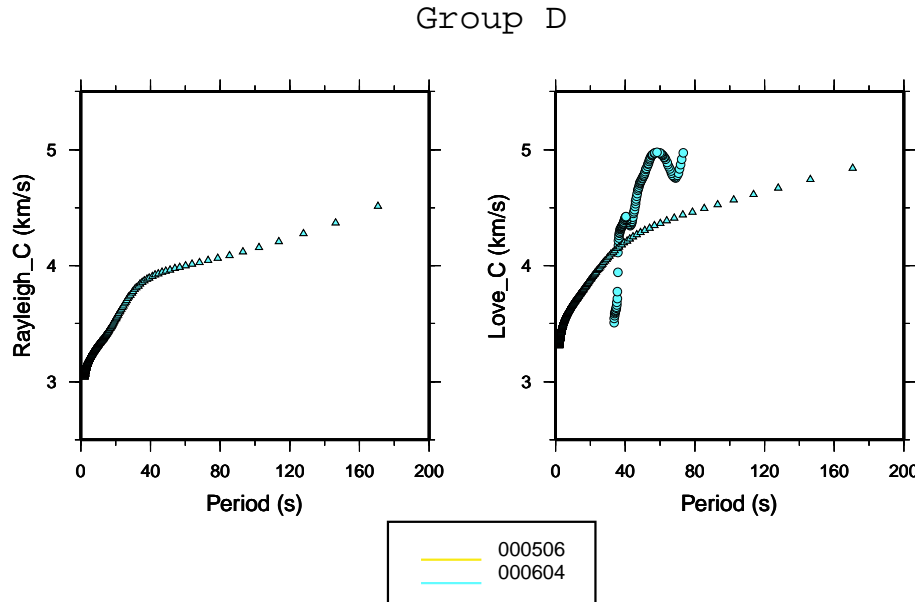
Group D

Figure 6.11: Rayleigh and Love phase velocity curves for D group. The different colors correspond to different earthquakes. The key between colors and earthquakes are displayed in left bottom of the figure. The circles and the triangles indicate the observations and the HAMBURG model predictions, respectively

Azimuth (°)		
Station/event	000506	000604
BLO	52	12
CCM		
MPH	57	19
PLAL	57	16
SIUC	54	16
SLM	53	17
UARL	57	22
UTMT	55	16

Table 6.11: Azimuths for the earthquakes in group D.

The results are only partially successful. The comparison of the obtained phase velocity dispersion curves with a model developed by Herrmann and Ammon (1997) for central U.S. gives only good results (they fit with the predictions within a 5%) for a reduced group of earthquakes (Figures 6.2, 6.7, and 6.9). These earthquakes were recorded in a large number of stations (6 or more). Also, their group velocity curves are the best in quality (absence of discontinuities and high signal-to-noise rate) in a wide range of periods, and so, allowed a good isolation of the fundamental mode. For the other earthquakes the methodology is unstable, giving place to unrealistic curves.

7. SUMMARY AND CONCLUSIONS

In this work I obtained the group velocity dispersion curves of the fundamental mode for Rayleigh and Love waves. The data set is composed of 50 events recorded by the Cooperative New Madrid Seismic Network and for the Alabama earthquake recorded by 48 stations located in North America. I have used the Multiple Filter Technique and the Phase Matched Filter methods to isolate the fundamental mode and retrieve its group velocity dispersion curve. These dispersion curves are important because they encode information about Earth's structure in depth.

The dispersion curves obtained for Rayleigh waves have been compared with the predictions of the Stevens' global earth model with the idea of testing its performance. In the period range from 13 to 160 seconds the Stevens' model reproduces the observations very accurately (within $\pm 3.3\%$ at 20 seconds). This is not a surprise because this is the period range in which most of the data used by Stevens in his inversion lie. For periods larger than 160 seconds the Stevens' model shows a linearly increasing tendency to overestimate the group velocity value. For example, for 160 seconds period the Stevens' model overestimate the group velocities by $12 \pm 2.5\%$. For these periods the Stevens' model is not based on the inversion of data, but on the PREM model for layers deeper than 200 km. At very long periods the problem may be inadequacy of the great-circle path assumption. For periods less than 13 seconds the model tends to underestimate the group velocity in comparison with the observation: At 5 seconds period I observe a difference between observations and prediction of $20 \pm 15\%$. These underestimations are more prominent for earthquakes

(or explosions) at regional distances and do not follow a clear pattern except for the explosion events. However, at these periods, my confidence in the resultant curves is limited because of the difficulty in removing contributions of higher modes. Similar results were obtained for the Alabama earthquake.

In the data set there are some local mining explosions located near Evansville, IN. The periods of these data range from 2 to 15 seconds. The comparison with the Stevens' model shows, as I already have commented, a tendency to underestimate. However, I can see a repeated pattern in all of them: a linear increase of the observed group velocity with respect to the predicted from 2 seconds up to a maximum value at 4 seconds, followed by a linear decrease from 4 to 6 seconds and an almost constant difference since for. The existence of this pattern could be an artifact of the model, since its spatial resolution is comparable to the source-receiver distances. From a physical perspective, it might be that the characteristics of the Paleozoic sedimentary basin in the central U.S. contribute to the differences between measured and predicted group velocity dispersion curves. This sedimentary basin is sampled by these very shortest periods for distances less than 500 km.

The second part of this work has been dedicated to calculating local phase velocities for Rayleigh and Love waves using the $p - \omega$ technique. This technique was developed to be applied in linear array used in reflection and refraction experiments. I have applied this technique in the Cooperative New Madrid Seismic Network, in spite of the fact that its geometry is not a linear array. In principle, this non-linearity would have to have only an small effect for far earthquakes. This technique was only applied

to clean signals, those where only the fundamental mode was present.

The results are only partially successful. The comparison of the obtained phase velocity dispersion curves with a model developed by Herrmann and Ammon (1997) for the central U.S. gives only good results for a small set of earthquakes, the fit between observations and predictions are within the 5%. These earthquakes share the feature that they were recorded by a large number of stations (6 or more). Also, their group velocity curves are the best in quality (absence of discontinuities and high signal-to-noise ratio)in a wide range of periods, and so, allowed a good isolation of the fundamental mode. For the other earthquakes, the methodology is unstable, giving place to unrealistic curves. This methodology will need of further analysis to check its viability and limitations, with emphasis on quantitatively defining the criteria for a good data set.

A crucial hypothesis in my calculation of local phase velocities is that the wave front is cylindrical. A direction left for the future is to use the dispersion curves in a model with no assumption whatsoever about the great circle path along the lines of Friederich et al. (1994, 2000).

Bibliography

Abramowitz, M. and I. A. Stegun, 1965, Handbook of mathematical functions, *Dover Publications, Inc.*, New York.

Aki, K., and P. G. Richards, 1980, Quantitative seismology: Theory and methods, *W. H. Freeman and Company*, San Francisco.

Ben-Menahem, A., and S. J. Singh, 1981, Seismic Waves and Sources, *Dover Publications, Inc.*, New York.

Bhattacharya, S. N., 1983, Higher order accuracy in multiple filter technique, *Bull. Seism. Soc. Am.*, 73, 1395-1406.

Chang, T., C. J. Ammon, and R. B. Herrmann, 1998, Faulting parameters of the October 24, 1997, Southern Alabama Earthquake, *Seism. Res. lett.*, 69, 175-175.

Curtis, A., J. Trampert, R. Sneider, and B. Dost, 1998. Eurasian fundamental mode surface wave phase velocities and their relationship with tectonic structures, *J. Geophys. Res.*, 103, 26919-26947.

Dziewonski, A. M., S. Bloch, and M. Landisman, 1969, A technique for the analysis of transient seismic signals, *Bull. Seism. Soc. Am.*, 59, 427-444.

Dziewonski, A. M. and A. L. Hales, 1972, Seismology: surface waves and Earth oscillations. Methods in computational physics, Vol 11. *Academic Press*, New York. Chap. 2, 70-72.

Ekstrom, G., A. M. Dsiewonski, G. P. Smith, and W. Su, 1996. Elastic and inelastic structure beneath Eurasia, in *Proceeding of the 18th Annual Seismic Research Symposium on Monitoring a Comprehensive Test Ban Treaty 4-6 September, 1996*, Phillips Laboratory Report PL-TR-96-2153, July, pp. 309-318, ADA313692.

Friederich, W., E. Wielandt and S. Stange, 1994 Non-plane geometries of seismic surface wavefields and their implications for regional surface-wave tomography, *Geophys. J. Int.*, 119, 931-948.

Herrin, E., and T. Goforth, 1977, Phase-matched filters: application to the study of Rayleigh waves, *Bull. Seism. Soc. Am.*, 67, 1259-1275.

Herrmann, R. B., 1973, Some aspects of band-pass filtering of surface wave, *Bull. Seism. Soc. Am.*, 63, 663-671.

Herrmann, R. B., 1979, Surface wave focal mechanisms for Eastern North American earthquakes, *J. Geophys. Res.*, 84, 3543-3552.

Herrmann R. B. and C. J. Ammon, 1997, Faulting parameters of earthquakes in the New Madrid, Missouri, region, *Engineering Geology*, 46, 299-311

Jenkins, G. M., and D. G. Watts, 1968, Spectral analysis and its applications, *Holden-day*, San Francisco.

Keilis-Borok, V. I. ed., 1986, Seismic surface waves in a laterally inhomogeneous Earth, *Klumer Academic Publishers*, Boston.

Laske G. and G. Masters, 1997, A global digital map of sediment thickness, *EOS Trans. AGU*, 78, F483.

Levshin, A. L., M. H. Ritzwoller, and S. S. Smith, 1996, Group velocity across Eurasia, in *Proceeding of the 18th Annual Seismic Research Symposium on Monitoring a Comprehensive Test Ban Treaty 4-6 September, 1996*, Phillips Laboratory Report PL-TR-96-2153, July, pp. 70-79, ADA313692.

McMechan, G. A. and R. Ottolini, 1980 Direct observation of a $p - \tau$ curve in a slant stacked wave field, *Bull. Seism. Soc. Am.*, 70, 775-789.

McMechan, G. A. and M. J. Yedlin, 1981, Analysis of dispersive waves by wave field transformation, *Geophysics*, 53, 869-874.

Mitchell, B. J., L. Cong, and J. Xie, 1996, Seismic attenuation studies in the Middle East and Souther Asia, St Louis University Scientific Report No. 1, PL-TR96-2154, ADA317387.

Montagner, J. P. and H. C. Nataf, 1986, A simple method for inverting the azimuthal anisotropy of surface wave, *J. Geophys. Res.*, 91, 511-520.

Mooney, W., G. Laske, and G. Masters, 1998, Crust 5.1: a global crustal model at 5x5 degrees, *J. Geophys. Res.*, 103, 727-747.

Percival, D. B., and A. T. Walden, 1993, Spectral analysis for physical applications: Multitaper and conventional univariate technique, *Cambridge University Press*, Cambridge.

Ritzwoller, M. H., A. L. Levshin, L. I. Ratnikova, and D. M. Tremblay, 1996, High resolution group velocity variations across Central Asia, in *Proceeding of the 18th Annual Seismic Research Symposium on Monitoring a Comprehensive Test Ban Treaty 4-6 September, 1996*, Phillips Laboratory Report PL-TR-96-2153, July, pp. 98-107, ADA313692.

Russell, D. R., 1987 Multi-Channel Processing of Dispersed Surface Waves, *Ph. D. Dissertation*, Saint Louis University, St. Louis, MO.

Russell, D. R., R. B. Herrmann and H. Hwang ,1988, Application of frequency variable filters to surface wave amplitude analysis, *Bull. Seism. Soc. Am.*, 78, 339-358.

Stevens, J. L., 1986, Estimation of scalar moments from explosion-generated surface wave, *Bull. Seism. Soc. Am.*, 76, 123-151.

Stevens, J. L., and McLaughlin, 1986, Regionalized maximum likehood surface wave analysis, Maxwell Technologies Technical report submitted to Air Force technical applications center, SSS-TR-89-9953, September, San Diego.

Stevens, J. L. and D. A. Adams, 1999, Improved methods for regionalized surface wave analysis, *Proceeding of the 21th Annual Seismic Research Symposium on Monitoring a Comprehensive Test Ban Treaty, September 1999*, 1, 274-282.

Tsai, Y. B. and K. Aki, 1969, Simultaneous determination of seismic moment and attenuation of surface waves, *Bull. Seism. Soc. Am.*, 59, 275-287.

Tsai, Y. B. and K. Aki, 1970, Precise focal depth determination from amplitude spectra of surface waves, *J. Geophys. Res*, 75, 5729-5743.

Vdovin, O. Y., J. A. Rial, Ritzwoller ,and M. H., A. L. Levshing, 1999, Group-velocity tomography of South America and the surrounding oceans, *Geophys. J. Int.*, 136, 324-330.

Vita Auctoris

Flor de Lis Mancilla was born in Cartagena, Spain on July 9, 1971. During her childhood she lived in different parts of the Iberian peninsula, but never north of Madrid. Becoming a physics student at the University of Granada stopped her from moving for a while. She graduated in Physics in 1997.

In Fall 1997, she was recruited as a pre-graduate student (a pre-position too much used and abused in Spain) by the "Instituto Andaluz de Geofísica y Prevención de Desastres Sísmicos". There she participated in several projects, including the installation of a broadband station at the Spanish base "Carlos I" in Antarctica.

In 1999, she began to move again. This time slightly north of New Madrid, but definitely south of the latitude of the old Madrid. At the "Department of Earth and Atmospheric Sciences" in Saint Louis University she has been pursuing a M.S. degree in geophysics.

It will continue in ...